Acquisition Methods for 7 Tesla MRI from Head to Toe

Sören Johst

Erwin L. Hahn Institute for Magnetic Resonance Imaging

Acquisition Methods
for 7 Tesla MRI from Head to Toe

Proefschrift

ter verkrijging van de graad van doctor
aan de Radboud Universiteit Nijmegen
op gezag van de rector magnificus prof. dr. Th.L.M. Engelen,
volgens besluit van het college van decanen
in het openbaar te verdedigen op dinsdag 16 december 2014
om 16.00 uur precies

door
Sören Malte Lennart Johst
geboren op 17 april 1984
te Heidelberg, Duitsland

Promotoren:	Prof. dr. David G. Norris Prof. dr. Mark E. Ladd, Deutsches Krebsforschungszentrum, Duitsland
Manuscriptcommissie:	Prof. dr. Arend Heerschap Prof. dr. Andrew G. Webb, Universiteit Leiden Dr. Gregory J. Metzger, University of Minnesota, Verenigde Staten

The studies in this thesis were performed at the Erwin L. Hahn Institute for Magnetic Resonance Imaging in Essen, Germany.

ISBN: 978-3-00-047676-1

Printed by: Universitätsdruckzentrum Duisburg-Essen, Duisburg, Germany

*“Of all the preposterous assumptions of humanity over humanity,
nothing exceeds most of the criticisms made on the habits of the poor
by the well-housed, well- warmed, and well-fed.”*

Herman Melville

For my life partner Isolde Aigner

Contents

List of original publications

Portions of this thesis are published in the following international peer-reviewed journal articles with the author of this thesis as first author:

Johst S, Wrede KH, Ladd ME, Maderwald S.
“Time-of-Flight Magnetic Resonance Angiography at 7 T Using Venous Saturation Pulses With Reduced Flip Angles”
Investigative Radiology, 2012; 47(8): 445-50.

Johst S, Orzada S, Fischer A, Umutlu L, Ladd ME, Maderwald S.
“Comparison of Fat Saturation Techniques for Single-Shot Fast Spin Echo Sequences for 7-T Body Imaging”
Investigative Radiology, 2014; 49(2): 101-8.

Johst S, Orzada S, Fischer A, Schäfer LC, Nassenstein K, Umutlu L, Lauenstein TC, Ladd ME, Maderwald S.
“Sequence Comparison for Non-enhanced MRA of the Lower Extremity Arteries at 7 Tesla”
PLOS ONE, 2014; 9(1): e86274.

Johst S, Maderwald S, Fischer A, Quick HH, Ladd ME, Orzada S.
“Investigation of the Saturation Pulse Artifact in Non-Enhanced MR Angiography of the Lower Extremity Arteries at 7 Tesla”
PLOS ONE (in press)

Chapter 1 Introduction

1.1 A brief look at the history of magnetic resonance imaging

In 1924, Wolfgang Pauli introduced the term “spin” to explain the hyperfine structure in nuclei. Following the preliminary work of Isidor I. Rabi, Felix Bloch and Edward M. Purcell described in 1946 the magnetic spin resonance in liquids and solids and performed the first experiments using nuclear magnetic resonance (NMR).[1,2] Afterwards, this method was mainly used in molecular physics and chemistry to examine structures via spectroscopy.

In 1950, Erwin L. Hahn discovered the spin echo and used it to study molecular diffusion in liquids.[3] The first one to relate NRM with medical imaging was Raymond Damadian, who measured T_1 and T_2 relaxation times in rat tumors and observed that the tumor tissue had longer relaxation times than normal tissue. He predicted that this technique in future might be useful for the detection of malignant tumors.[4]

However, the first real MR image was not realized until 1973 when Paul C. Lauterbur used a projection technique similar to computer tomography (CT) to obtain the first images.[5] Richard Ernst introduced in 1975 the reconstruction method via Fourier transformation which is used today,[6] followed 1977 by the first MR images of a human being generated by Peter Mansfield.[7]

In the beginning of the 1980s, the first clinical MR systems were installed. In the following years an increase of the static magnetic field strength was pursued as the signal-to-noise ratio (SNR) increases approximately linearly with the field strength.[8] Nowadays magnetic field strengths of 1.5 T and 3 T are the current clinical standards.[9] In MRI, the term magnetic field strength is normally used despite the fact that magnetic flux density would be the correct term as defined by the theory of electromagnetism.

In 1999, the first 7 T system was installed at the University of Minnesota. While today more than 35 7 T magnets are set up worldwide; in contrast to 3 T, they have not yet arrived in the clinical environment and are only used as research systems. The main reason is the inhomogeneous transmission field caused by the shorter radio frequency wavelength at 7 T.[10] In the final MR images this appears e.g. as black bands or contrast changes. Hence, ameliorating the effects of the inhomogeneities is a main focus of research at ultra-high field (7 T and above).

Since the beginning of MRI with only proton-density-weighted spin-echo sequences, a vast variety of different imaging sequences have been developed providing a wide range of contrasts for medical diagnosis non-invasively and without ionizing radiation. Using the same MR hardware a mere change of image acquisition parameters is able to provide a wide range of different information: Not only the basic tissue-property-weighted contrasts are possible, but also e.g. brain function, diffusion, flowing blood or the heart cycle in real time can be depicted.

1.2 Principles of magnetic resonance imaging

In the following, a short introduction into the physical principles of MRI is given. More detailed theoretical background can be found in standard textbooks.[11,12]

Spins and magnetization

Atomic nuclei possess an intrinsic angular momentum called spin. It is a mere quantum-mechanical phenomenon. The atomic nucleus consists of nucleons (neutrons and protons, each with spin ½) and its spin is the sum of the spins of the nucleons. If the number of nucleons is even, the spin of the nucleus is zero as two individual nucleons always form pairs with antiparallel spin directions. Only nuclei with odd number of nucleons have non-zero spin with absolute value

$$|\vec{I}| = \hbar\sqrt{I(I+1)} \tag{1.1}$$

where $\hbar = 1.0551^{-34}\ Ws^2$ is the reduced Planck's constant and I the spin quantum number which can only take the discrete values $I = 0, 1/2, 1, 3/2, 2, \ldots$. For the description of the quantized angular momentum the magnetic quantum number $m = -I, -I+1, \ldots, I-1, I$ is necessary. Hydrogen H^1 which is the most abundant nuclei in the human body and therefore preferably used for MRI, has only one proton which means that it possesses a nuclear spin of $I = 1/2$ with magnetic quantum number $m = \pm 1/2$. Both in units of $\hbar$.

The angular momentum $\vec{I}$ of the positively charged proton is associated with a magnetic moment $\vec{\mu}$:

$$\vec{\mu} = \gamma\vec{I} \tag{1.2}$$

where γ is the gyromagnetic ratio which depends on the nucleus. Hydrogren has a value of $\gamma/2\pi$ = 42.577 MHz/T. Without external magnetic field, the sum of magnetic moments within a sample is zero as the directions of the individual magnetic moments are randomly distributed. However, if an external magnetic field B_0 is present, the magnetic moment $\vec{\mu}$ interacts with the external field thus the discrete energy levels described by

$$E_m = -\gamma\hbar m B_0 \tag*{[1.3]}$$

split up according to the Zeeman effect. Nuclei with spin 1/2 have two different eigenstates where the z component of $\vec{\mu}$ is either aligned parallel or antiparallel to the axis of the external magnetic field. The energy difference for nuclei with spin 1/2,

$$\Delta E = -\gamma\hbar B_0 \tag*{[1.4]}$$

corresponds to the resonant radio frequency (RF) waves that can be emitted or absorbed by the spin system. As the energy of a photon is $E = \hbar\omega_0$ the following equation is valid

$$E = \hbar\omega_0 = \gamma\hbar B_0 \tag*{[1.5]}$$

which tells us the resonance frequency (called Larmor frequency) of the system:

$$\omega_0 = \gamma B_0 \tag*{[1.6]}$$

For an external magnetic field of $B_0 = 7\,T$, the frequency $\nu_0 = \omega_0/2\pi$ amounts to approximately 300 MHz.

The macroscopic magnetization M_0 of a sample is the absolute value of the vector sum of the magnetic moments $\vec{\mu}_i$ of the individual spins. In thermal equilibrium, the probability p_m in which state (parallel / antiparallel to the external field) the individual spins can be found, is given by the Boltzmann distribution:

$$p_m = \frac{e^{-\frac{E_m}{kT}}}{Z};\ Z = \sum_{m=-I}^{I} e^{-\frac{E_m}{kT}} \tag*{[1.7]}$$

with E_m from equation [1.3], the partition function Z and kT being the Boltzmann energy (Boltzmann constant $k = 1.38 \cdot 10^{-23} WsK^{-1}$ and temperature T in Kelvin). Using the high-temperature approximation ($kT >> \gamma\hbar B_0$, valid for room temperature of *300K* and B_0 = 7 T) M_0 can be calculated (with N being the total number of nuclei):

$$M_0 = \frac{N\gamma^2\hbar^2 I(I+1)}{3kT} B_0 \qquad [1.8]$$

Comparing the number of nuclei in state $E_{1/2}$ and $E_{-1/2}$, a slightly higher number of nuclei (≈ 10^{-6}) can be found in the lower energy state $E_{1/2}$, which means spins aligned parallel to the external field $\vec{B}_0$. Only the high number of spins ($N \approx 10^{19}$ per mm^3 body tissue) allows the realization of MRI despite the small amount of net magnetization - the higher M_0 the higher the MR signal. The direct proportionality of M_0 and B_0 which can be seen in equation [1.8] explains the drive for higher field strength as the possibility of cooling down living tissue is not given.

Excitation and relaxation

The quantum mechanical description of the equation of motion of the magnetization $\vec{M}$, can be converted into classical Euler's equation of motion:

$$\frac{d}{dt}\vec{M}(t) = \vec{M}(t) \times \gamma\vec{B}(t) \qquad [1.9]$$

Analog to classical movement of a spinning top in a gravity field, $\vec{M}$ precesses around the axis $\vec{B}(t)$ with the Larmor frequency (eq. [1.6]). The measured signal in MRI is proportional to the transversal component of $\vec{M}$ which induces - through its precession - a signal in a coil with axis orthogonal to the static magnetic field $\vec{B}_0$. Because $\vec{M}$ is aligned parallel to $\vec{B}_0$ in thermal equilibrium, it needs to be tipped away from the z-axis in order to generate signal. This is achieved by an external radio frequency field, called $\vec{B}_1$, which is emitted orthogonal to $\vec{B}_0$. The tip or flip angle α between $\vec{M}$ and the z-axis is proportional to the strength of $\vec{B}_1$and the duration of its emission. The shape of the envelope of the emitted $\vec{B}_1$ field is called RF excitation pulse. The movement of $\vec{M}$ under influence of $\vec{B}_0$, $\vec{B}_1$ and the restoration of the thermal equilibrium state can be described via the Bloch equations:

$$\frac{d}{dt}M_x = \gamma(\vec{M} \times \vec{B})_x - \frac{M_x}{T_2} \qquad [1.10]$$

$$\frac{d}{dt}M_y = \gamma(\vec{M} \times \vec{B})_y - \frac{M_y}{T_2} \qquad [1.11]$$

$$\frac{d}{dt}M_z = \gamma(\vec{M} \times \vec{B})_z + \frac{M_0 - M_z}{T_1} \qquad [1.12]$$

T_1 is the longitudinal relaxation time describing the recovery of M_z to its equilibrium state while T_2, the transversal relaxation time, describes the loss of the phase coherence between the individual spins. Both relaxation times depend on the tissue in which the spins are located. In reality, local field inhomogeneities and susceptibility effects lead to a much faster dephasing of the spins (T_2* decay).

Image formation

If additionally a magnetic gradient field is applied, the Larmor frequency gets dependent on the spatial position:

$$\vec{G} = \frac{\delta B_z}{\delta x}\vec{e}_x + \frac{\delta B_z}{\delta y}\vec{e}_y + \frac{\delta B_z}{\delta z}\vec{e}_z \qquad [1.13]$$

$$\omega(\vec{x},t) = \gamma B_z(\vec{x},t) = \gamma(B_0 + \vec{x}\vec{G}(t)) \qquad [1.14]$$

This effect is used in MR imaging in two different ways: While the B_1 field is switched on to flip the magnetization, a concomitant slice selection gradient is applied in z-direction. Thereby, the Larmor frequency changes linearly in that direction and dependent on the strength of the applied gradient and the bandwidth of the excitation RF pulse only a single slice of an object within the magnetic field is excited. The chosen carrier frequency of the excitation pulse defines the position on the z-axis where the slice is excited. This relation is illustrated in Figure 1.1.

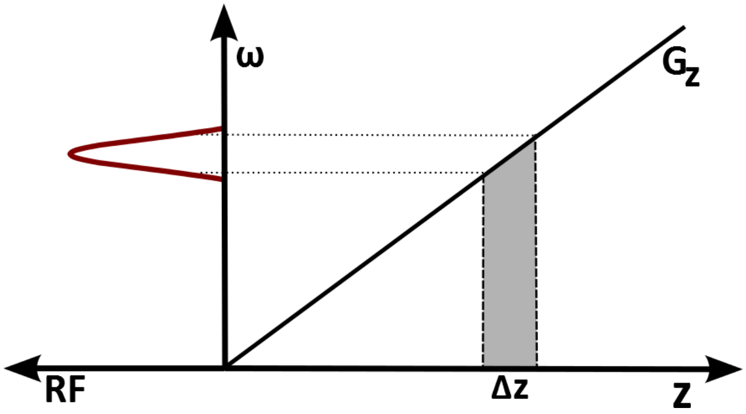

Figure 1.1: *Schematic depiction of slice selection. The thickness of the excited slice is dependent on the gradient strength and the bandwidth of the RF pulse.*

The second way the spatial frequency dependence described in equation [1.14] is used is the so-called frequency encoding. During acquisition of the MR signal, a gradient in x-direction (also called readout direction) is applied. Thereby, via a Fourier transformation (FT) every frequency within the acquired signal can be assigned to a position on the x-axis. The strength of the gradient amplitude determines the resolution of this dimension.

The second dimension within the excited slice is also obtained via a Fourier relation. For this purpose, the phase of the signal is manipulated via a gradient on the y-axis of the MR system. This gradient is switched on for a short time between excitation and acquisition of the signal. Depending on the amplitude and duration of this gradient the spins acquire an additional phase. The phase encoding needs to be repeated for a certain amount of different gradient amplitudes to acquire enough data to perform a FT in this direction. The resolution in the phase encoding direction is determined by the number of performed phase encoding steps. Frequency encoding is also performed in every step. In that way, a two-dimensional complex data space is filled, called k-space (Figure 1.2) which can be Fourier transformed into a location-dependent magnetization $M_{\perp}(x,y)$:

$$S(k_x,k_y,t) \sim \int_x \int_y M_{\perp}(x,y,t_0) e^{-i(k_x x + k_y y)} dxdy \qquad [1.15]$$

$$k_{x/y} = \int G_{x/y}(t)\, dt \qquad [1.16]$$

Three-dimensional data sets can be obtained if an additional phase encoding gradient is applied on the z-axis.

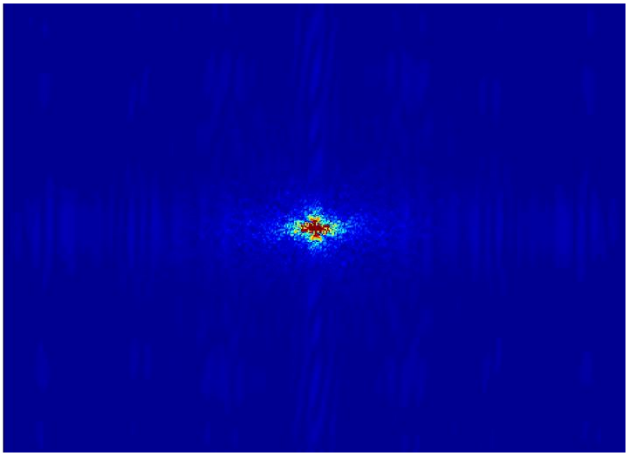

Figure 1.2: *Example of k-space representation of a MR image. Here, the magnitude part of the complex k-space is shown. Values beyond 1 were cut off for better visibility. Via Fourier transform the magnitude and phase of the final MR image can be obtained.*

Spin Echo

The timing and order of excitation, gradient switching and acquisition is called a sequence. There are two basic classes of sequences that differ in the way the signal, the so-called echo, is generated.

In the spin-echo sequence, a 90° excitation RF pulse flips the magnetization in the transversal plane. The spins dephase according to the T_2* decay. Through application of a 180° RF pulse, the effect of the T_2* relaxation can be revoked. The spins are rephased and a signal is formed. This kind of signal formation is called spin echo, the time between excitation and acquisition of the echo is called echo time *TE*. The timing of a basic spin echo sequence is shown in Figure 1.3.

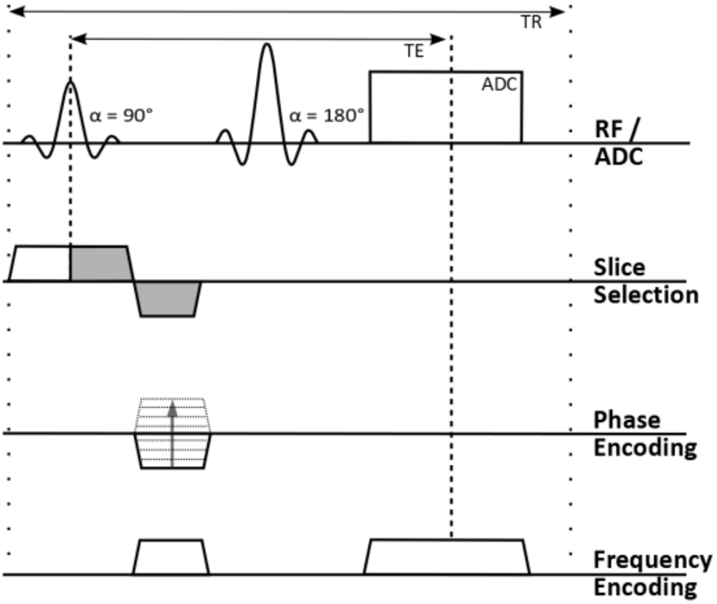

Figure 1.3: *Basic principle of the spin-echo sequence. 90° excitation pulse and slice selection gradient are applied simultaneously followed by a refocusing gradient that rephrases the spins within the slice. Concurrently one step of the phase encoding gradient is carried out. At half of the echo time TE, a 180° refocusing pulse is applied. During acquisition (ADC), a frequency encoding gradient is applied.*

As the effect of T_2* is annulled, amongst e.g. T_1 and proton density (PD) weighting, an image contrast mainly determined by the T_2 relaxation times within the object can be achieved. Due to the 180° refocusing pulse, spin-echo sequences are more robust against e.g. susceptibility artifacts than gradient echo sequences.

Gradient Echo

In a gradient-echo sequence, the 180° RF pulse is removed and an additional gradient is applied to dephase the spins even faster. The echo is formed by inverting the direction of the gradient leading to the rephasing of the spins. This principle is illustrated in Figure 1.4.

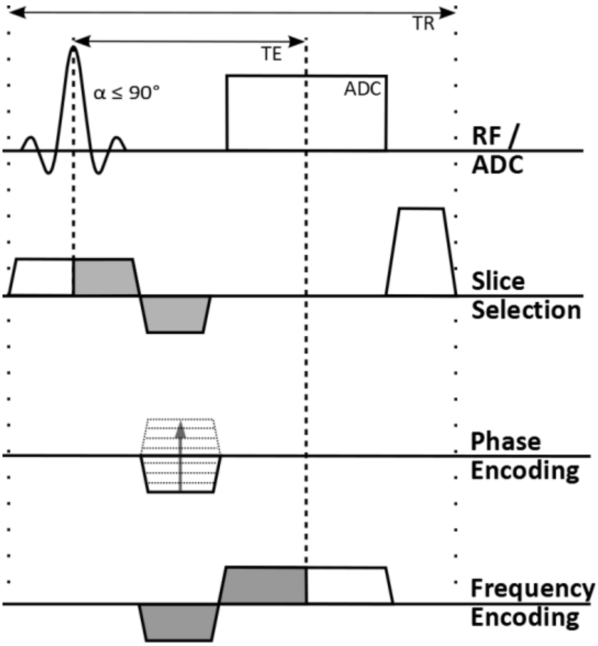

Figure 1.4: *Basic principle of the gradient-echo sequence. An excitation pulse of less than 90° and slice selection gradient are applied simultaneously. The echo time TE is defined by a dephasing gradient that is followed by the frequency encoding gradient with opposite sign. The repetition time ends with a spoiling gradient that dephases the remaining transverse magnetization.*

As the effect of the T_2* relaxation cannot be rephased that way, the maximum signal amplitude of the echo is decreased by the T_2* dephasing. Signal strength is also influenced by the chosen flip angle and repetition time *TR* which is the time between two consecutive excitations. One advantage of using gradient-echo sequences are shorter echo times. By choosing *TR* and *TE* accordingly, e.g. T_1, PD or mere T_2* weighting of the MR images can be achieved.

Drawbacks of 7 T

Besides the gain in SNR (equation [1.8]), increasing the field strength B_0 to 7 T also leads to disadvantages. Amongst others, B_0 inhomogeneities are increased generated by susceptibility effects at the transition of different tissues. This can result e.g. in geometric distortions or intra-voxel dephasing.[13]

Besides tipping the magnetization, the excitation RF pulses simultaneously heat the tissue. This is measured via the specific absorption rate (SAR) defined via the electrical field strength $\vec{E}$ which is generated by the time-varying magnetic field - as described via the Maxwell equations.

$$SAR = \frac{1}{2}\frac{\sigma}{\rho}E^2 \qquad [1.17]$$

σ is the conductivity and ρ the density of the tissue. In general one can derive a relation with the main magnetic field, the flip angle and the bandwidth $\Delta\omega$ of the RF pulse:[12]

$$SAR \sim B_0^2 \alpha^2 \Delta\omega \qquad [1.18]$$

As SAR is in general increasing with the main magnetic field many clinical sequence protocols used at 1.5 T or 3 T cannot be transferred to 7 T without modifications for compliance with the SAR limitations defined by the International Electrotechnical Commission (IEC) guidelines.[14]

With the increase of the static magnetic field, the Larmor frequency also increases and hence the wavelength of the emitted RF waves decreases accordingly. At 7 T, the wavelength is approximately *15 cm* which is smaller than most human body dimensions including the head. Hence, constructive and destructive interferences of the B_1 fields generate an inhomogeneous excitation throughout the field of view (FOV), which leads e.g. to variations in SNR and contrast of the final image.[10,15-17]

RF shimming

One way to counter the B_1 inhomogeneities is a technique called RF shimming.[18,19] Here, multiple elements transmit the same excitation B_1 waveform but with individual amplitudes and phases. The resulting field B_1^{total} is the complex sum of all fields $B_{1,n}$ transmitted by the N individual elements with their respective weighting factors b_n:

$$B_1^{total}(\vec{\mathrm{r}}) = \sum_{n=1}^{N} b_n \cdot B_{1,n}(\vec{\mathrm{r}}) \qquad [1.19]$$

This equation can be formulated as a system of complex equations and thereby solved for a given B_1^{total} target. Typically this system of equations is overdetermined. The most commonly used targets are a region of interest with a B_1^{total} distribution as homogeneous as possible or with the magnitude of B_1^{total} as large as possible. In general, the increase in homogeneity in a certain region of interest leads to a decrease in other regions of the FOV. With mere RF shimming, a completely homogeneous excitation over the FOV is thus not achievable.

Transmit Sense

Compared to RF shimming, Transmit SENSE[20-22] expands the flexibility in such a way that every transmit channel not only has its individual amplitude and phase settings, but is able to apply an individual B_1 RF pulse completely independent from the other channels. Additionally, not only one gradient for slice selection but all three gradient directions are used to provide additional spatial encoding within the excited imaging slice. Hence, this technique is able to provide any desired target pattern within the FOV.

This is clearly depicted by the image domain method developed by Grissom et al.[23] For small tip angles,[24] the transverse magnetization M_{xy} of a single transmit coil can be approximated by the Fourier integral of the applied excitation k-space trajectory $\vec{k}(t)$ weighted by a complex RF pulse *b(t)* and the complex spatial transmit sensitivity $s(\vec{\mathrm{r}})$ of the coil:

$$M_{xy}(\vec{\mathrm{r}}) = i\gamma M_0 s(\vec{\mathrm{r}}) \int_0^T b(t) e^{i\vec{\mathrm{r}}\cdot\vec{\mathrm{k}}(t)} e^{i\gamma \Delta B_0(\vec{\mathrm{r}})(t-T)} \mathrm{d}t \qquad [1.20]$$

M₀ is the equilibrium magnetization, *T* the RF pulse duration and $e^{i\gamma \Delta B_0(\vec{\mathrm{r}})(t-T)}$ describes additional phase accumulations due to spatially varying inhomogeneities $\Delta B_0(\vec{\mathrm{r}})$. Excitation k-space $\vec{k}(t)$ is defined as the time-reversed integration of the gradients:[24]

$$\vec{\mathrm{k}}(t) = -\gamma \int_t^T \vec{\mathrm{G}}(\mathrm{r}) \mathrm{d}r \qquad [1.21]$$

The expression [1.20] can be expanded to multiple transmit coils exploiting linearity in the small-tip angle regime. Here, the desired transverse magnetization target M_{xy} can be described as the spatial superposition of the excitation patterns of the individual transmit elements:

$$M_{xy}(\vec{\mathrm{r}}) = i\gamma M_0 \sum_{n=1}^{N} s_n(\vec{\mathrm{r}}) \int_0^T b_n(t) e^{i\vec{\mathrm{r}}\cdot\vec{\mathrm{k}}(t)} e^{i\gamma \Delta B_0(\vec{\mathrm{r}})(t-T)} \mathrm{d}t \qquad [1.22]$$

Analog to [1.20], s_n are the transmit sensitivities and b_n the RF waveforms of the *N* individual coils. To calculate the individual waveforms b_n for a chosen magnetization target, gradient trajectory and measured coil sensitivities and field inhomogeneities, equation [1.22] is normally reformulated as a minimization problem.[23]

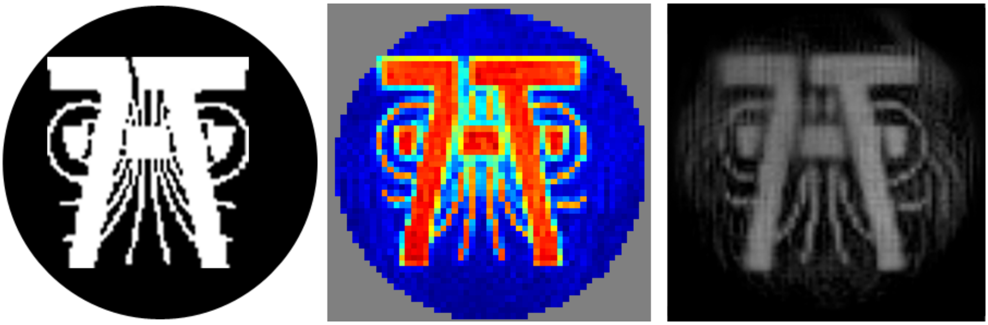

Figure 1.5: *Example of a Transmit SENSE excitation. Here, the target magnetization was the logo of the Erwin L. Hahn Institute for MRI (left). In the middle, the simulation of the calculated RF pulse via the Bloch equations is shown and on the right the actual excitation in a homogeneous spherical oil phantom using an 8-channel transmit/receive head array.*

1.3 Objective of this thesis

The aim of this thesis is to develop and investigate new imaging sequence techniques for 7 T MRI of the whole human body. The focus is on applications including regions outside the human head aiming towards clinically-oriented, feasible 7-T imaging. As representative areas of the human body, in addition to the head, the abdomen and the lower extremities were chosen. For all studies, new sequence variants considering the challenging conditions of 7 T were developed, implemented and tested in phantom measurements and in-vivo.

In chapter 2, a time-of-flight (TOF) sequence for non-enhanced MR angiography (MRA) of the intracranial arteries is developed. Especially TOF MRA techniques profit from the increased magnetic field strength of 7 T.[25,26] However, in order to suppress the venous signal, additional saturation RF pulses need to be applied. To stay within the regulatory SAR limits, TR needs to be prolonged preventing acquisition of high-resolution data sets within clinically acceptable total acquisition times. Besides using the variable-rate selective excitation (VERSE) algorithm for both excitation and saturation to ameliorate the SAR constraints, saturation RF pulses were additionally reduced in their duration and flip angle. The minimal necessary flip angle for sufficient suppression of the veins is determined in the parameter range commonly used in clinical imaging protocols. Theoretical background, evaluations of the RF pulse profiles as well as first in-vivo images in a patient are presented.

In chapter 3, fat saturation techniques for single-shot fast spin echo (SSFSE) sequences at 7 T are presented. For the standardly used saturation technique, at 7 T black bands in the bright fat signal instead of complete suppression are observed. As delineation between fat and bright liquids in SSFSE images is essential for diagnosis, the goal of this study is to provide a feasible, homogeneous fat saturation technique for the challenging case of SSFSE 7 T body imaging. Here, four different fat saturation techniques for SSFSE are implemented and compared in a healthy volunteer study, whereby the recently proposed time-interleaved acquisition of modes (TIAMO)[27,28] is used for the imaging portion of the sequence to reduce B_1 artifacts. The different fat saturation variants, in-vivo images as well as the corresponding evaluations are shown in this chapter.

Non-enhanced MRA imaging in the diagnosis of diseases of the lower extremity vasculature is becoming more and more important as the administration of Gadolinium-based contrast agents has been associated with nephrogenic systemic fibrosis in patients with severe renal dysfunction.[29] The potential of 7 T non-enhanced TOF MRA imaging of the lower extremity vasculature is examined in chapter 4 in a comparison of three sequences. An ultrafast spoiled gradient echo (UGRE) sequence is modified: To keep the total acquisition time short, RF pulses for the suppression of venous signals are implemented in a sparse fashion. Again, TIAMO is implemented to counter the B_1 inhomogeneities at 7 T. Here, cardiac triggering via a phonocardiogram[30] is necessary to prevent signal variation in the arteries. The modified UGRE is compared to a gradient echo sequence without cardiac triggering and a Quiescent-Interval Single-Shot (QISS) sequence. Sequence diagrams, technical details of the acquisition, quantitative evaluations, imaging artifacts as well as in-vivo images of healthy volunteers are presented.

In chapter 5, the work on the UGRE sequence, which performed best in the sequence comparison of chapter 4, is continued to provide deeper insight into an artifact that appears like aliasing that was observed in the previous work. In simulations of different sequence variants, the nature of the artifact is determined, verified in static and flow phantoms and also in a healthy volunteer. Simulations and measurement results are shown and discussed.

The work shown in chapters 2 to 5 has already been published and these chapters are formatted accordingly. The implemented TOF MRA sequence variant of chapter 2 was used in a clinical study with neurosurgical patients comparing non-enhanced MR Imaging of cerebral aneurysms at 7 T to 1.5 T regarding delineation of unruptured intracranial aneurysms.[31] A similar evaluation of cerebral arteriovenous malformations is currently under review.[32] Another study evaluating the clinical applicability of this sequence protocol (amongst others by a neuroradiological assessment of the delineation of arterial vessels) was recently published.[33] The sequences for non-enhanced MRA of the legs described in chapter 3 were also evaluated in a radiological qualitative image analysis looking at different artery segments with regard to e.g. artery delineation and presence of artifacts.[34] The UGRE sequence variant that performed best was used in an ensuing clinical study evaluating 7-T non-contrast-enhanced MRA in patients with peripheral arterial occlusive disease in comparison to contrast-enhanced MRA at 1.5 T.[35]

The last chapter, chapter 6, provides a brief summary and discussion.

References

1. Bloch F. Nuclear Induction. Phys Rev 1946;70:460-474.
2. Purcell EM, Torrey HC, Pound RV. Resonance Absorption by Nuclear Magnetic Moments in a Solid. Phys Rev 1946;69:37-38.
3. Hahn EL. Spin Echoes. Phys Rev 1950;80:580-594.
4. Damadian R. Tumor Detection by Nuclear Magnetic Resonance. Science 1971;171:1151-1153.
5. Lauterbur PC. Image Formation by Induced Local Interactions - Examples Employing Nuclear Magnetic-Resonance. Nature 1973;242:190-191.
6. Kumar A, Welti D, Ernst RR. Nmr Fourier Zeugmatography. Journal of Magnetic Resonance 1975;18:69-83.
7. Mansfield P, Maudsley AA. Medical Imaging by Nmr. Brit J Radiol 1977;50:188-194.
8. Hoult DI, Phil D. Sensitivity and power deposition in a high-field imaging experiment. J Magn Reson Imaging 2000;12:46-67.
9. Ai T, Morelli JN, Hu XM, Hao DP, Goerner FL, Ager B, Runge VM. A Historical Overview of Magnetic Resonance Imaging, Focusing on Technological Innovations. Investigative radiology 2012;47:725-741.
10. Van de Moortele PF, Akgun C, Adriany G, Moeller S, Ritter J, Collins CM, Smith MB, Vaughan JT, Ugurbil K. B(1) destructive interferences and spatial phase patterns at 7 T with a head transceiver array coil. Magn Reson Med 2005;54:1503-1518.
11. Levitt M. Spin dynamics, basics of nuclear magnetic resonance: John Wiley & Sons, Ltd.: 2001.

12. Bernstein M, King K, Zhou X. Handbook of MRI Pulse Sequences: Elsevier Academic Press: 2004.

13. Truong TK, Chakeres DW, Beversdorf DQ, Scharre DW, Schmalbrock P. Effects of static and radiofrequency magnetic field inhomogeneity in ultra-high field magnetic resonance imaging. Magn Reson Imaging 2006;24:103-112.

14. Moser E, Stahlberg F, Ladd ME, Trattnig S. 7-T MR-from research to clinical applications? Nmr Biomed 2012;25:695-716.

15. Snyder CJ, Delabarre L, Metzger GJ, van de Moortele PF, Akgun C, Ugurbil K, Vaughan JT. Initial results of cardiac imaging at 7 tesla. Magn Reson Med 2008.

16. Vaughan JT, Snyder CJ, DelaBarre LJ, Bolan PJ, Tian J, Bolinger L, Adriany G, Andersen P, Strupp J, Ugurbil K. Whole-body imaging at 7T: preliminary results. Magn Reson Med 2009;61:244-248.

17. Umutlu L, Orzada S, Kinner S, Maderwald S, Brote I, Bitz AK, Kraff O, Ladd SC, Antoch G, Ladd ME, Quick HH, Lauenstein TC. Renal imaging at 7 Tesla: preliminary results. European radiology;21:841-849.

18. Collins CM, Liu W, Swift BJ, Smith MB. Combination of optimized transmit arrays and some receive array reconstruction methods can yield homogeneous images at very high frequencies. Magn Reson Med 2005;54:1327-1332.

19. Mao W, Smith MB, Collins CM. Exploring the limits of RF shimming for high-field MRI of the human head. Magn Reson Med 2006;56:918-922.

20. Katscher U, Bornert P, Leussler C, van den Brink JS. Transmit SENSE. Magn Reson Med 2003;49:144-150.

21. Katscher U, Bornert P, van den Brink JS. Theoretical and numerical aspects of transmit SENSE. IEEE transactions on medical imaging 2004;23:520-525.

22. Katscher U, Rohrs J, Bornert P. Basic considerations on the impact of the coil array on the performance of Transmit SENSE. Magma (New York, NY 2005;18:81-88.

23. Grissom W, Yip CY, Zhang Z, Stenger VA, Fessler JA, Noll DC. Spatial domain method for the design of RF pulses in multicoil parallel excitation. Magn Reson Med 2006;56:620-629.

24. Pauly J, Nishimura D, Macovski A. A k-space analysis of small-tip-angle excitation. J Magn Reson 1989;81:43-56.

25. Maderwald S, Ladd SC, Gizewski ER, Kraff O, Theysohn JM, Wicklow K, Moenninghoff C, Wanke I, Ladd ME, Quick HH. To TOF or not to TOF: strategies for non-contrast-enhanced intracranial MRA at 7 T. Magma 2008;21:159-167.

26. Nowinski WL, Puspitasaari F, Volkau I, Marchenko Y, Knopp MV. Comparison of Magnetic Resonance Angiography Scans on 1.5, 3, and 7 Tesla Units: A Quantitative Study of 3-Dimensional Cerebrovasculature. J Neuroimaging 2013;23:86-95.

27. Orzada S, Maderwald S, Poser BA, Bitz AK, Quick HH, Ladd ME. RF excitation using time interleaved acquisition of modes (TIAMO) to address B1 inhomogeneity in high-field MRI. Magn Reson Med 2010;64:327-333.

28. Orzada S, Maderwald S, Poser BA, Johst S, Kannengiesser S, Ladd ME, Bitz AK. Time-interleaved acquisition of modes: an analysis of SAR and image contrast implications. Magn Reson Med 2012;67:1033-1041.

29. Thomsen HS. Nephrogenic systemic fibrosis: A serious late adverse reaction to gadodiamide. Eur Radiol 2006;16:2619-2621.

30. Nassenstein K, Orzada S, Haering L, Czylwik A, Zenge M, Eberle H, Schlosser T, Bruder O, Muller E, Ladd ME, Maderwald S. Cardiac MRI: evaluation of phonocardiogram-gated cine imaging for the assessment of

global und regional left ventricular function in clinical routine. Eur Radiol 2012;22:559-568.

31. Wrede KH, Dammann P, Monninghoff C, Johst S, Maderwald S, Sandalcioglu IE, Muller O, Ozkan N, Ladd ME, Forsting M, Schlamann MU, Sure U, Umutlu L. Non-enhanced MR imaging of cerebral aneurysms: 7 Tesla versus 1.5 Tesla. PLoS One 2014;9:e84562.

32. Wrede HK, Dammann P, Johst S, Mönninghoff C, Schlamann M, Maderwald S, Sandalcioglu IE, Ladd ME, Forsting M, Sure U, Umutlu L. Non-enhanced MR imaging of cerebral arteriovenous malformations: 7 Tesla versus 1.5 Tesla. (under review) 2014.

33. Wrede HK, Johst S, Dammann P, Özkan N, Mönninghoff C, Kreaemer M, Maderwald S, Ladd ME, Sure U, Umutlu L, Schlamann M. Improved cerebral time-of-flight magnetic resonance angiography at 7 Tesla – feasibility study and preliminary results using optimized venous saturation pulses. PLoS One 2014;9:e106697.

34. Fischer A, Johst S, Orzada S, Ladd ME, Nassenstein K, Lauenstein TC, Maderwald S. Non-enhanced T1w imaging of the lower extremity arteries at 7 Tesla. In: Proceedings of the 21st Annual Meeting of ISMRM, Salt Lake City, USA, 2013. (abstract 4474).

35. Fischer A, Maderwald S, Johst S, Orzada S, Ladd ME, Umutlu L, Lauenstein TC, Kniemeyer HW, Nassenstein K. Initial evaluation of non-contrast-enhanced magnetic resonance angiography in patients with peripheral arterial occlusive disease at 7 T. Investigative radiology 2014;49:331-338.

Chapter 2 Time-of-Flight Magnetic Resonance Angiography at 7 T Using Venous Saturation Pulses With Reduced Flip Angles*

Abstract

The visibility of the vasculature in time-of-flight (TOF) magnetic resonance angiography (MRA) highly profits from increased magnetic field strengths. However, the application of additional saturation pulses for suppression of the venous system is often not possible at 7 T; to remain within the regulatory specific absorption rate (SAR) limits, the repetition time (TR) needs to be prolonged, preventing the acquisition of high-resolution MRA data sets within clinically acceptable acquisition times. In this work, saturation pulses were modified regarding flip angle and duration to meet SAR constraints and minimize total measurement time.

To ameliorate SAR restrictions, the variable-rate selective excitation (VERSE) algorithm was used for both excitation and saturation radio frequency pulses. In this way, saturation pulses (executed every TR) become applicable in high-resolution TOF MRA protocols but still lengthen total measurement time notably. In this work, saturation pulses were further modified in terms of flip angle and duration to meet SAR constraints and minimize total measurement time.

In the considered parameter range for excitation flip angle α of 15° to 35° and TR of 20 ms to 35 ms, sufficient saturation flip angles (α_{SAT}) were 30° to 50°.

This work shows that by lowering the flip angle α_{SAT}, saturation pulses can be applied in high-resolution clinical TOF protocols using a TR as short as 20 ms. An α_{SAT} of $\alpha + 15°$ is sufficient for suppression of the venous system in TOF MRA protocols in the parameter range normally used at 7 T. Instead of the standard 90° saturation pulse, only half the flip angle (or even less) is necessary, substantially

ameliorating SAR constraints and enabling acquisition of high resolution in acceptable imaging time.

****Johst S**, Wrede KH, Ladd ME, Maderwald S.
“Time-of-Flight Magnetic Resonance Angiography at 7 T Using Venous Saturation Pulses With Reduced Flip Angles”
Investigative Radiology, 2012; 47(8): 445-50.*

2.1 Introduction

It has been shown that time-of-flight (TOF) magnetic resonance angiography (MRA) highly profits from increased field strengths.[1-4] In TOF MRA sequences, repetition time (TR) intervals are chosen preferably as short as possible to take advantage of the prolonged T_1 values at 7 T.[5] As the high-resolution 3D data sets are acquired over many excitation cycles, low steady-state signals can easily be achieved for static background tissue when using short TR. In comparison, the signal from inflowing, completely relaxed blood is high, providing the desired image contrast of TOF MRA.

The application of saturation pulses for suppression of the venous system using a standard flip angle of 90° is often not possible without substantial prolongation of TR.[1,6] Using the variable-rate selective excitation (VERSE) algorithm[7] for excitation/saturation radio frequency (RF) pulses,[8] the use of 90° saturation pulses is possible, but TR still has to be prolonged because of SAR constraints. If saturation pulses are applied every TR, a flip angle of 90° is generally more than would be necessary to suppress venous signal (in particular when looking at maximum intensity projections [MIPs]). In this work, we propose to take advantage of the inherent saturation effects of the relative short TR in this type of sequence not only for background suppression but also for the saturation of the venous system.

To achieve this, 3 different changes were introduced beyond the utilization of VERSE. (1) Shorter saturation pulses (which allow shorter TR) are applied to suppress an area above the imaging slab that is as thick as possible and that covers the superior sagittal sinus. As a slice-selection gradient controls the thickness of the saturation area, changes in duration (and thus changes in the frequency bandwidth of the pulse) are balanced by the amplitude of this gradient. (2) To remain in conformance with SAR limits, the shorter saturation RF pulses are applied with smaller flip angle. (3) Not only the duration of the RF pulse itself prolongs the minimum TR, but also the spoiler gradients that follow the saturation pulse. Therefore, we also implemented spoiler gradients with shorter duration.

The fact that the blood flow inside the veins is slower than inside the arteries (mean maximum velocity, 0.35 m/s in cerebral veins[9] compared with, eg, 0.32-0.82 m/s in the basilar artery[10]) and that the course of the superior sagittal sinus is nearly parallel to the cranium also simplifies the task of saturating the venous system.

Other authors have chosen to apply 90° saturation pulses sparsely, for example, once every 230 ms with a TR of 23 ms.[11-13] This alternative concept is beyond the scope of this manuscript. In this work, we examined the influence of different saturation pulse durations on the excitation profile of a 3D TOF MRA sequence with the constraint of minimizing total measurement time and systematically varied the flip angle of the saturation pulses (α_{SAT}) with the aim of achieving sufficient suppression of venous signals inside the imaging slab, with α_{SAT} as small as possible to ameliorate SAR limitations.

2.2 Theoretical Background

As higher values of the RF amplitude contribute disproportionately to the SAR of the RF pulse, the main principle of the VERSE algorithm is to crop and prolong these portions of the RF pulse; in parallel, the slice-selection gradient has to be modified to balance the changes in instantaneous bandwidth of the RF pulse. Here, an implementation similar to Schmitter et al[8] was used.

The steady-state signal in spoiled gradient echo sequences is described by the formula[14]:

$$\mathrm{S}=M_0 \sin(\alpha)\mathrm{e}^{-\mathrm{TE}/\mathrm{T2}^*}\frac{1\text{-}\mathrm{e}^{-\mathrm{TR}/\mathrm{T1}}}{1\text{-}\cos(\alpha)\mathrm{e}^{-\mathrm{TR}/\mathrm{T1}}} \qquad [2.1]$$

The following relaxation time values were used in subsequent calculations: T_1 was 1220/2132/2587/4300 ms for white matter (WM)/ grey matter (GM)/blood[5]/cerebrospinal fluid (CSF),[15] respectively, and T_2* was 26.8/33.2/7.4/120 ms for WM/GM[16]/blood[17]/CSF (taken from Figure 3 in Peters et al[16]), respectively.

With the assumption that the signal of the spins reaches a steady state during passage through the superior sagittal sinus, the criterion for sufficient suppression of the veins inside the imaging slab is given by $S_{Tissue} \geq S_{Sinus}$. Here, the considered background tissue consisted of WM, GM, and CSF. Subcutaneous fat was not taken into account, as fat signal can be masked in MIP processing. Because the increase in the steady-state signal of GM/WM/CSF with higher TR values is almost identical to the increase in the steady-state signal of blood, sufficient saturation is expected over the entire range of TR values (Fig. 2.1A). Within the considered parameter range, α_{SAT} does not need to be 90° to reach a steady-state signal S_{Sinus} lower than that of the surrounding tissue S_{Tissue}. This is illustrated in Figure 2.1A for an excitation flip angle of 20°. For α_{SAT} of 35°, TR of 20 ms, and echo time (TE) of 4.34 ms, S_{Sinus} remains below S_{Tissue} for excitation flip angles α up to 65°. However, the number of repetitions needed to reach the steady state varies strongly with α_{SAT}.

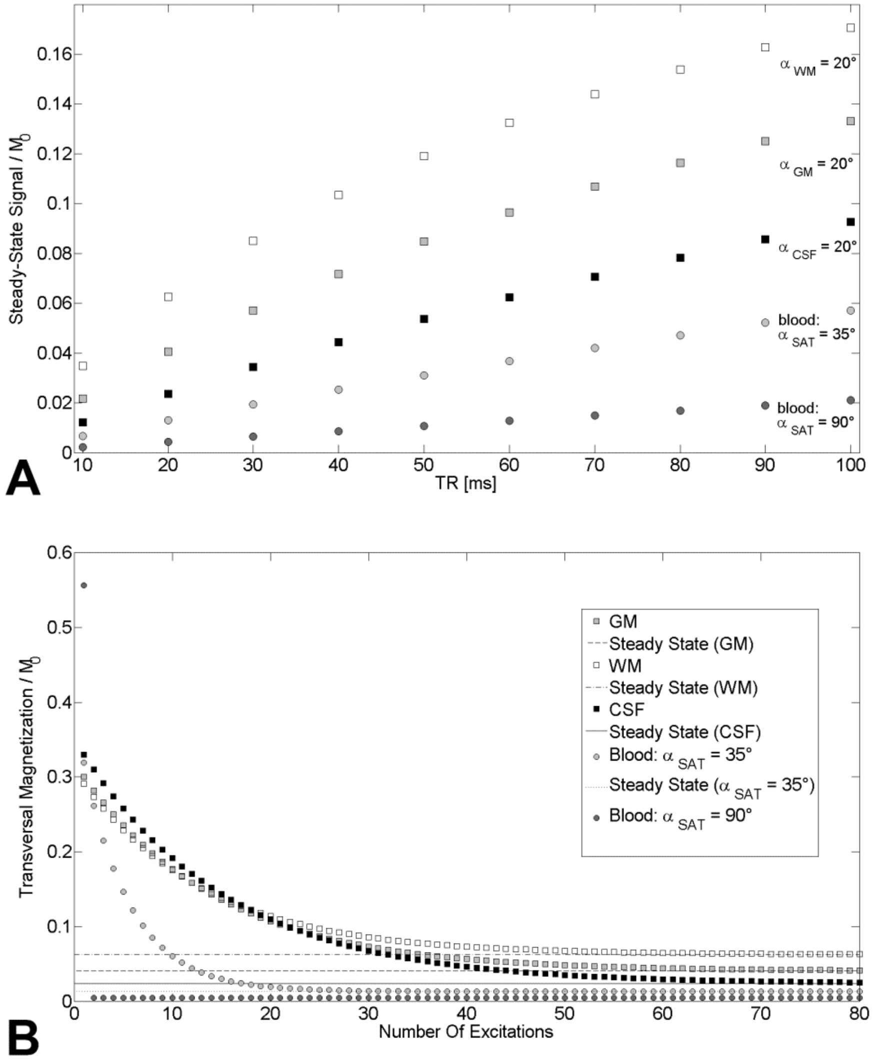

Figure 2.1. *A, Theoretical steady-state signals for WM/GM/blood/CSF using different TR values. B, Transition to steady state for WM/GM/blood/CSF using a TR of 20 ms, α of 20°, and* α_{SAT} *of 35°. Blood signal needs 13 excitations to fall below the steady-state signal of WM/GM. For calculation of the steady-state signals, the following relaxation times were used:* T_1*, 1220/2132/2587/4300 ms (WM/GM/blood*[5]*/CSF*[15]*, respectively); and* T_2**, 26.8/33.2/7.4/120 ms (WM/GM*[16]*/blood*[17]*/CSF*[16]*, respectively).*

The transition to steady state with increasing number i (= 1,2,3,…) of RF excitation pulses is described by the formula[14]:

$$M_0 \sin(\alpha) e^{\text{-TE/T2*}} \left(f + (1 - f)\left(\cos(\alpha)\mathrm{e}^{\text{-TR/T1}}\right)^{i-1}\right) \qquad [2.2]$$

$$\mathrm{f} = (1 - e^{-TR/T1})/(1 - \cos(\alpha)\mathrm{e}^{\text{-TR/T1}})$$

For α_{SAT} of 35°/TR of 20 ms, about 31 saturation pulses are needed in the sinus (vs about 56/69/74 excitations in WM/GM/CSF for an α_{SAT} of 20°, TR of 20 ms, and TE of 4.34 ms) to reach 95% of the steady-state signal, whereas only 2 saturation pulses of 90° are needed (Fig. 2.1B).

With a TR of 20 ms (50 repetitions per second) and assuming a 0.1-m length of the superior sagittal sinus, the venous blood experiences about 31 excitations when flowing with a velocity of 0.16 m/s. Sufficient saturation for longer TR/faster flow may still succeed due to presaturation, which the blood spins experience during their course through the imaging slab before they enter the saturation slab. In addition, fewer repetitions are needed to reach signals below the steady-state signal of the brain tissue (eg, for GM, 13 for a TR of 20 ms [Fig. 2.1B], 7 for a TR of 100 ms; not shown in Fig. 2.1B). Saturation pulses with flip angles below 90° need a certain number of excitations (which increases with diminishing flip angle) to lead to an acceptable signal attenuation. The exact number of experienced excitations is patient-individual, depending, for example, on blood flow velocity and head shapes and sizes.

One can define a vessel-to-background ratio (VBR = S_{Sinus} / S_{Tissue}) to measure the degree of saturation of the sagittal sinus. The criterion for adequate venous saturation is a VBR equals 1, which means that the signal in the sagittal sinus is isointense with the surrounding tissue. Isointensity is at least necessary to get true arterial TOF MRA images. Therefore, VBR equals 1 defines the minimum saturation flip angle (and thereby SAR) that is necessary for venous suppression. The saturation flip angle α_{SAT} leading to this optimal VBR depends mainly on the chosen TR and excitation flip angle α. As the degree of saturation also depends on patient-individual factors, saturation flip angles should, in general, be chosen that produce calculated VBR less than 1.

2.3 Materials and Methods

Imaging was performed on a 7-T whole-body system (Magnetom 7T, Siemens Healthcare, Erlangen, Germany) equipped with a 32-channel Tx/Rx head coil (Nova Medical, Wilmington, MA). A high-resolution clinical TOF MRA protocol was first optimized in volunteer scans before saturation pulses were added.[18] The 3D fast low-angle shot TOF high-resolution protocol acquired a single slab using flow compensation, tilt-optimized nonsaturated excitation (TONE) across the slab of 50% (flip angle at inferior edge divided by superior edge), an excitation pulse flip angle α of 20°, a TR of 20 ms, a TE of 4.34 ms, an acquisition time of 6 minutes 22 seconds per slab, 112 slices (oversampling 14.3%), a generalised autocalibrating partially parallel acquisitions acceleration factor R equals 4 (48 reference lines), partial Fourier 6/8 (read/slice), matrix of 896 x 756, a voxel size of 0.22 x 0.22 x 0.41 mm^3, and VERSE cutoff thresholds (percentage of maximum amplitude of the original pulse at which the pulse is cropped by the VERSE algorithm[8]) of 50%/30% (excitation/saturation pulses). The saturation slab covered the entire area above the imaging slab (at least 4 cm), leaving a gap to the imaging slab of about 2 cm. The saturation pulse was applied every TR interval.

The application of standard 90° saturation pulses does not only increase SAR but also prolongs the minimal TR because of the duration of the RF pulse itself (here, vendor-provided duration is 3840 microseconds) and the spoiler gradients that follow the saturation pulse. To incorporate the saturation pulses into the high-resolution protocol, saturation pulse duration was made variable between 1025 and 6000 microseconds, using about 500-microsecond gradient ramping time and a short spoiler gradient of 4000-microsecond duration. Thus, at most, 10,500 microseconds is necessary for the saturation block (VERSE applied and an appropriate α_{SAT} chosen), which facilitates the integration of the saturation block into a TR of 20 ms.

The shortened spoiler gradient (75,000 µs mT/m gradient moment) was tested in phantom measurements and validated in vivo (sequence parameters as above, vendor-provided polydimethylsiloxane oil phantom, T_1, ~1400 ms) by shifting the saturation area inside the imaging slab, using an α_{SAT} of 90°/50°/10° (the latter being close to the Ernst angle of blood and background tissue), and switching off the normal excitation pulse (transmitter voltage, 0 V). With sufficient spoiling gradient moment, only noise and no residual signal from transverse magnetization excited by the saturation pulse should be observable. For comparison, all measurements were repeated with 0 µs mT/m spoiling moment.

Excitation slice profiles of the modified saturation pulses were measured (same phantom) and evaluated in comparison with ideal slice profiles (Bloch simulation, Matlab r2008a; The MathWorks, Natick, MA). For this purpose, a modified version of the TOF MRA protocol was used. The excitation RF pulse was replaced by the saturation pulse with excitation thickness only 35% of the nominal excitation thickness but still 100% readout thickness to capture the slopes and side lobes of the excitation profile. Sequence parameters were as follows: excitation flip angle α, 10°; TR, 50 ms; TE, 7.29 ms; acquisition time, 11 minutes 6 seconds per slab; 512 slices per slab; no generalised autocalibrating partially parallel acquisitions; partial Fourier 6/8 (phase); matrix, 256 x 31 (phase resolution 12% to shorten measurement time); and slice thickness, 0.34 mm (effective excitation slab thickness about 6 cm). The duration of the saturation pulse was varied between 1025 and 6000 microseconds in steps of 1000 microseconds. The measured slice profiles were normalized by the sensitivity profile of the 32-channel head coil before analysis. B_1 transmit profile was ignored because the transmit field of the 32-channel head coil is homogeneous with a deviation of 10.0% in the relevant area. The following parameters were examined: thickness (width of profile at half maximum), center shift of the saturation profiles (middle position between lobes at half maximum), and overlap with imaging slab (amplitude of side lobes at position corresponding to position of first slice in imaging slab). The ripple in the plateau of the saturation profile was not evaluated because this was not considered relevant for the saturation effectiveness of the pulse.

A duration of 2000 microseconds was chosen for the saturation pulse α_{SAT} to fit within a TR of 20 ms. The flip angle α_{SAT} was varied in steps of 5° beginning with 10° until the saturation criterion was fulfilled. The criterion for acceptable venous saturation was set to a VBR less than 0.6 (instead of VBR $\leq$ 1) to account for differences in, for example, head shapes and sizes or flow velocity. Vessel-to-background ratio was measured in the slice of the imaging slab, which lies adjacent to the saturation area. Due to the TONE excitation profile of the imaging slab, the signal of the tissue in this slice is lowest and increases toward the inferior portion of the slab.

A slab covering the Circle of Willis - considered to be the most clinically relevant - was chosen for the saturation flip angle variation scans. The finally chosen α_{SAT} was verified in 7 healthy volunteers. Because the normally used parameter range in 7-T TOF MRA[11-13,19] covers a TR of 20 ms to 35 ms and an α of 15° to 35°, the excitation flip angle α was varied in steps of 5°, and TR, in steps of 5 ms. As the theoretical values for VBR vary less than 10% for different TRs (comparing TR of 20/35 ms, Fig. 2.1A), α_{SAT} was varied for α of 15° to 35° and TR of 20 ms. The thereby determined α_{SAT} was then validated for a TR up to 35 ms. To meet the SAR constraints despite higher excitation flip angles, a longer duration for the saturation RF pulse, lower image resolution, and lower VERSE thresholds were used. As the steady-state signal of the tissue is normally reached with about 60 excitations and the blood experiences the same number of excitations (same slice thickness), the relation between α and α_{SAT} should, in general, not depend on image resolution.

In additional volunteer measurements, the slope of the TONE RF pulse and the slab thickness (shifting the imaging slab to keep center position of saturation area and gap) were varied to examine the influence of these parameters. For a TR of 20 ms and an α of 20°/ 35° (and corresponding sufficient α_{SAT}), slab thickness was changed to 50% and 30% of the original thickness and TONE excitation pulses were changed to 100% (flat excitation profile) and 20% (maximum available slope of excitation profile in this protocol).

Before the acquisition of all TOF MRA sequences, B_0 shimming was performed using a vendor-provided gradient echo sequence and algorithm based on the work of Schar et al.[20] For B_1 field mapping and local flip angle optimization, a vendor-provided spin echo type sequence was used. After a slice-selective excitation, 2 refocusing pulses generate a spin echo and a stimulated echo, respectively. The algorithm is mainly based on the work of Hoult.[21]

2.4 Results

In the phantom/in vivo measurements with the shorter spoiling gradient for α of 90°/50°/10°, only noise was observed. No difference was visible compared with images acquired without any RF. Measurements without dephasing of the transverse magnetization showed severe signal artifacts over the entire FOV.

The evaluation of the saturation slice profiles (Table 2.1, Fig. 2.2) showed that the shift of the center of the slice profiles is always away from the imaging slab for both VERSE and unmodified saturation pulses. Maximal values were 2.0 ± 0.5/1.6 ± 0.3 mm, mean values were 1.1 ± 0.1/0.7 ± 0.1 mm for VERSE/unmodified saturation pulses. For the broadening of the slice profiles, a maximum increase of 12.9% ± 0.8% was observed (relative to the thickness of the slice profiles acquired with the unmodified saturation pulse). Mean values were 6.2% ± 0.1%. The broadening of the slice profiles of the unmodified saturation pulse was always below 5% (relative to the theoretical slice profile thickness). The maximum amplitude of the side lobes at the overlap with the first slice of the imaging slab was 5.0% ± 0.5%/2.0% ± 0.5% (relative to the maximum amplitude of the saturation profile). Mean values were 2.5% ± 0.1%/1.3% ± 0.1% for VERSE/unmodified saturation pulses.

Duration, µs	Shift, mm	Thickness, %	Side Lobes, %
1025	0.8/0.2	100.0	1/1
2000	0.0/0.2	100.2	2/2
3000	1.5/0.6	108.2	1/1
4000	0.9/0.8	107.5	2.5/1
5000	1.2/1.0	108.4	3.5/1
6000	2.0/1.6	112.9	5/2

Table 2.1. *Evaluation of measured saturation slice profiles of VERSE/unmodified saturation RF pulses with different durations: Shift of slice center (error ± 0.5 mm), thickness of slice profile (error ± 0.8%; 100% corresponds to thickness of slice profile of unmodified RF pulse), and amplitude of side lobes (error ± 0.5%) at the position corresponding to the first image of the imaging slab.*

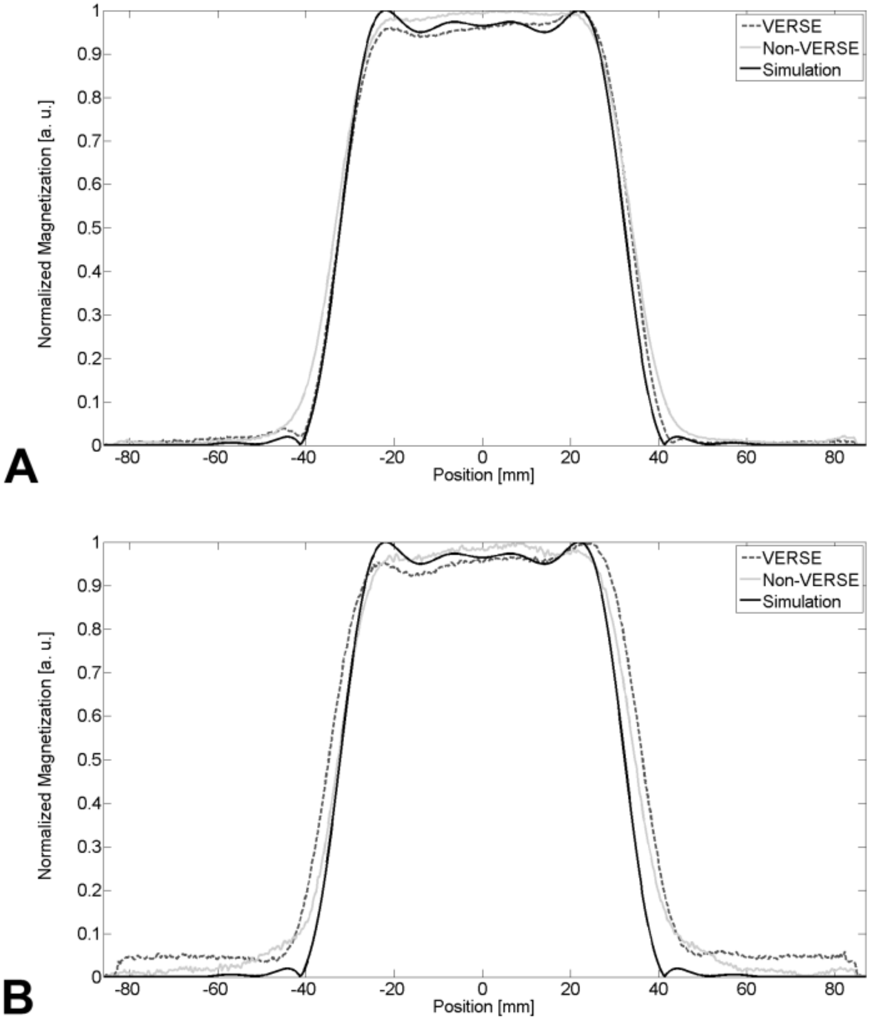

Figure 2.2. *Slice profiles (61-mm thickness) of a 1025-microsecond (A) and a 6000-microsecond (B) saturation pulse with and without VERSE technique applied in comparison with a simulated profile (without VERSE).*

In Figure 2.3, the results of the variation of α_{SAT} are shown for an α of 20° and TR of 20 ms. A pulse duration of about 2000 microseconds and, thus, a total duration of the saturation block of about 6500 microseconds were achieved. In all slices of the imaging slab, the VBR was equal to or less than the VBR in the first image of the imaging slab adjacent to the saturation area. The measured signal decreases with higher $\alpha_{SAT,}$ but the slope of the curve diminishes: The gain in signal suppression decreases with higher α_{SAT} (Fig. 2.3). For an α_{SAT} of 25° or greater, the signal in the sagittal sinus was smaller than the signal of the surrounding tissue. Variation of α_{SAT} for saturation pulses without VERSE (TR, 22 ms; duration of saturation pulse, 3000 microseconds) yielded similar results: For an of α_{SAT} of 25° or greater, the signal in the sagittal sinus was lower than that of the surrounding tissue. Ultimately, an α_{SAT} of 35° was chosen for an α of 20° to meet the more stringent criterion of VBR less than 0.6 (Fig. 2.4). Accordingly, for the considered excitation flip angles α of 15°/20°/25°/30°/35°, the choice of the most desirable saturation flip angle was determined to be an α_{SAT} of 30°/35°/40°/45°/50° (= α + 15°) (Fig. 2.5A). The course of the determined VBR versus saturation flip angle looked very similar for different excitation flip angles except for a shift toward higher flip angles (exemplarily shown for α of 20°/35° in Fig. 2.5B). In all volunteer scans, the respective α_{SAT} led to sufficient venous saturation over the entire considered TR range (20-35 ms; Fig. 2.3).

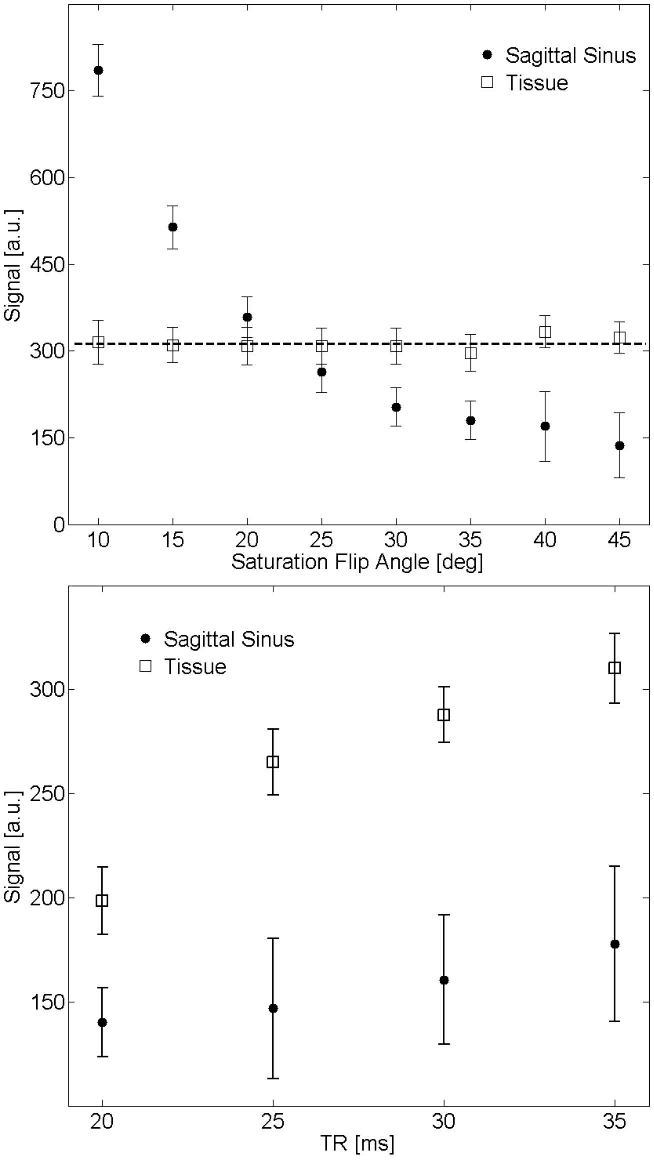

Figure 2.3. *Signal in the sagittal sinus (black circles) compared with signal in the surrounding tissue (white boxes) for an* α *of 20°, TR of 20 ms, and variation of saturation flip angle* α_{SAT} *(top). Signals versus TR for an* α *of 20° and* α_{SAT} *of 35° are shown (bottom). Error bars represent the standard deviation inside the region of interest.*

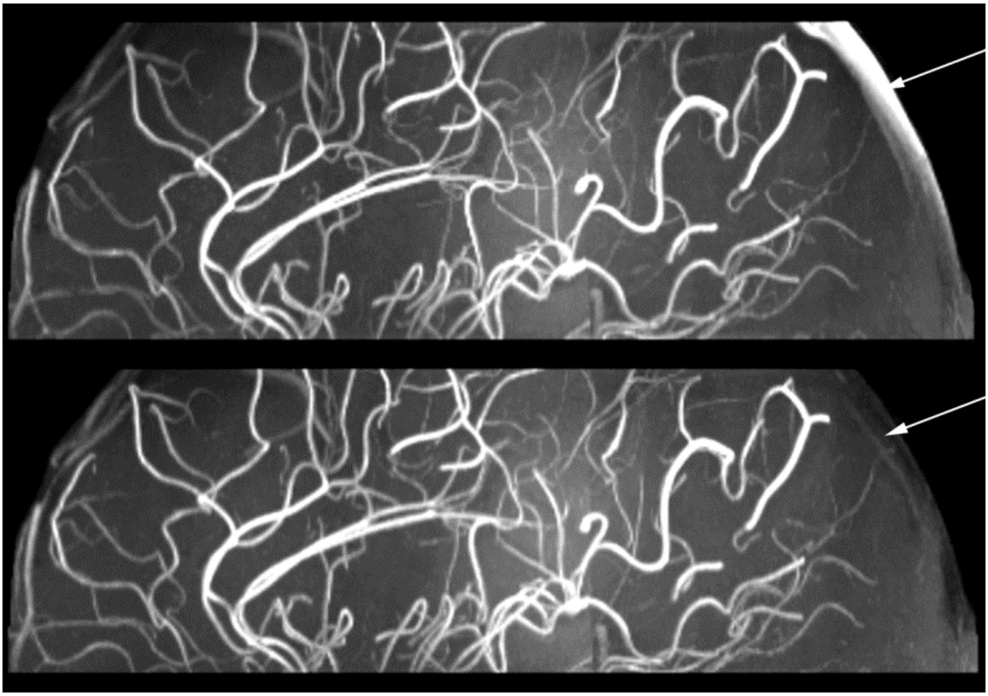

Figure 2.4. *Sagittal MIP (skull removed) showing TOF without (top) and with saturation RF pulse (bottom): An* α_{SAT} *of 35° led to complete saturation of sagittal sinus (*$\alpha = 20°$*;* $TR = 20$ *ms). White arrows indicate sagittal sinus.*

The signal in the sagittal sinus did not change significantly when acquiring different slab sizes (same center position of the saturation slab). A VBR of 0.42 ± 0.07 (0.59 ± 0.3)/0.38 ± 0.09 (0.63 ± 0.1)/0.36 ± 0.11 (0.84 ± 0.2) was determined for 100%/50%/30% slice thickness and an α of 15°/α_{SAT} of 30° ($\alpha = 35°/\alpha_{SAT} = 50°$). Different slopes of the TONE ramp changed the VBR for an α of 15°/α_{SAT} of 30° ($\alpha = 35°/\alpha_{SAT} = 50°$) from 0.43 ± 0.08 (0.89 ± 0.16) for 50% TONE pulses to 0.34 ± 0.07 (0.65 ± 0.13) for 100% TONE pulses and to 0.51 ± 0.1 (1.36 ± 0.18) for 20% TONE pulses. Only in the case of the highest slope and α of 35° was the chosen α_{SAT} of 50° not sufficient to compensate for the high flip angles at the superior edge of the slab.

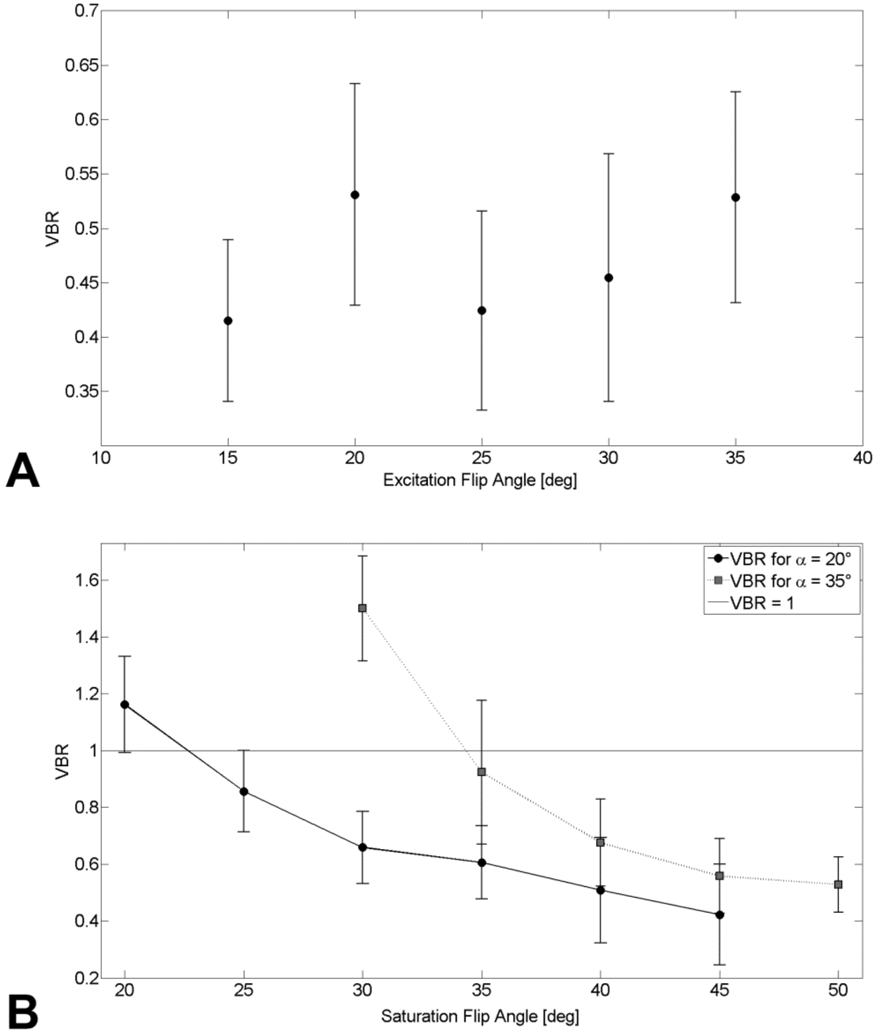

Figure 2.5. *A, Measured VBR for different excitation flip angles and the corresponding saturation flip angle according to an* α_{SAT} *of α + 15°. B, Comparison of the course of VBR as a function of the saturation flip angle for an α of 20° and 35°. The similarity and the shift toward higher flip angles can be clearly seen.*

2.5 Discussion

The shortened spoiler gradient with a spoiling moment of 75,000 µs mT/m fulfilled the desired requirements: No residual magnetization belonging to spins excited inside the saturation area and that moved into the imaging slab disturbed the image. Because the modified spoiler gradient is able to sufficiently spoil the transverse magnetization of saturation pulses with an α_{SAT} of 10°/50°/90° for a TR of 20 ms, it is assured that sufficient spoiling will be achieved for higher TR values and any α_{SAT} inside the considered range. Because the spoiler gradient and excitation slice-selection gradient are applied with the same sign, the excitation gradient works as an additional spoiler for the magnetization inside the saturation area. In this work, the spoiler gradient moment was reduced to achieve a shorter duration of the saturation sequence time block to fit into a minimum TR of 20 ms. The determination of an optimized duration/moment for the spoiler gradient could be examined in future work.

Longer saturation pulse duration in general leads to higher sensitivity to B_0 inhomogeneity, which leads to inaccurate slab profiles. For the saturation slabs, an exact slice profile is not important as long as the saturation area does not overlap with the imaging slab. This is the reason for choosing a lower VERSE cutoff threshold for the saturation pulses than for the excitation pulses in the high-resolution TOF MRA protocol.[8] No overlap with the imaging slab was perceivable in any of the measurements of saturation slice profiles, as the side lobe amplitude was always below (or equal to) 5%. In addition, broadening of the excited saturation profile is not a problem for the chosen sequence parameters because a broadening of the saturation profile above 165% (for a saturation slab thickness of 6 cm) would be necessary to fill the gap of 2 cm used here. The shift of the profiles is very small and away from the imaging slab, so the imaging slab remains undisturbed.

The variation of α_{SAT} for the high-resolution protocol ($\alpha = 20°$; TR = 20 ms) led to the choice of an α_{SAT} of 35° to ensure that saturation would work for different head sizes and shapes. To show feasibility, the protocol was applied in a patient with basilar tip and media aneurysms (Fig. 2.6), leading to a VBR of 0.67 ± 0.15 (compared with 4.12 ± 1.39 without saturation). The measurement was conducted in accordance with all guidelines set forth by the approving institutional review board. Informed consent was obtained before the examination. Provision for a margin to ensure consistent saturation leads to a general rule for the sufficient saturation flip angle α_{SAT} of $\alpha + 15°$. The respective saturation flip angles were validated within the parameter range of TR of 20 to 35 ms and of α of 15° to 35°. Consistent with theory (Fig. 2.1), the VBR did not significantly change when prolonging TR from 20 ms up to 35 ms. Thus, for the considered parameter range, sufficient saturation flip angles are only about half (or less) of the conventionally used flip angle of 90°.

The decreasing slope of the signal in the sagittal sinus (Fig. 2.3) with increasing α_{SAT} is expected by theory (cf. Eq. 2.1) and indicates that for a further increase in α_{SAT}, the increase in SAR outweighs the gain in VBR. The measured VBR in all slices was equal to or smaller than the VBR in the first image of the imaging slab adjacent to the saturation slab. This is due to the TONE ramp (highest flip angle at superior edge of slab leading to lowest steady-state background signal), as the signal in the sagittal sinus stays approximately the same throughout the entire slab. Different slopes of the TONE ramp changed the VBR: in the case of α of $35°/\alpha_{SAT}$ of 50°, VBR was greater than 1 for a TONE ramp of 20%. This implies that only smaller ramps fulfill the requirements for the reduced saturation flip angles.

Presaturation of the blood flowing through the imaging slab does not seem to significantly influence the signal in the sagittal sinus, as no significant signal changes were observed when different imaging slab sizes were used (while keeping the saturation slab constant). Because the imaging slab thickness does not influence the saturation of the venous signal significantly, the chosen saturation flip angles are also sufficient when using multiple overlapping thin slab angiography (MOTSA).[22] A measurement comparing the VBR of our single-slab clinical high-resolution protocol with a 3-slab MOTSA technique (using the same parameters but one-third slab thickness: TR = 20 ms; $\alpha = 20°$; $\alpha_{SAT} = 35°$) showed

Figure 2.6. *Axial (top) and coronal (bottom; skull removed) MIP of patient with basilar tip and media aneurysms (grey/black arrows) using a high-resolution protocol (α_{SAT} = 35°; α = 20°; TR = 20 ms). The white arrow indicates sagittal sinus.*

that VBR for all 3 slabs varied maximally 10% compared with the single-slab technique.

The flip angle reduction as performed here simplifies the use of venous saturation pulses in high-resolution TOF MRA at 7 T, as the resultant flip angles are less than half of the standard 90° saturation pulses. In addition, the modified saturation pulses are more flexible: The duration can be adjusted for a given TR or can be prolonged to meet SAR restrictions or other sequence requirements. For the optimized clinical protocol, a shorter saturation pulse duration (2000 microseconds) than the one provided by the vendor (3840 microseconds) was achieved, which led to a shorter TR and, thereby, to shorter total measurement time.

The implementation of saturation pulses that are variable in time and reduced in flip angle is an easy-to-implement method to ameliorate the SAR constraints in TOF protocols with venous saturation, even for the case where the much more complicated VERSE technique is not yet implemented. For the same overall SAR (51%), the presented clinical high-resolution protocol is acquirable with non-VERSE pulses within a total acquisition time of 7 minutes 38 seconds (TR was changed from 20 to 24 ms and the duration of the saturation pulse was changed from 2000 to 5500 microseconds) versus 6 minutes 22 seconds in conjunction with the VERSE technique. However, to minimize the total measurement time, the VERSE technique is essential. Using the original saturation method (saturation pulse duration, 3840 microseconds; 90°; VERSE only for excitation pulses), a minimum TR of 23 ms was necessary to accommodate the pulse durations and SAR limitations were exceeded, leading to 219% SAR. Applying VERSE to the 90° saturation pulse led to 104% SAR. By additionally reducing the saturation flip angle to 35°, 51% of allowed SAR was reached.

In summary, this work shows that by reducing the flip angle α_{SAT}, saturation pulses can be applied every TR in high-resolution clinical TOF protocols using a TR as short as 20 ms. In addition, by making the duration of the saturation pulses a parameter that can be changed online, more flexibility in protocol creation can be gained. An α_{SAT} of $\alpha + 15°$ is sufficient for suppression of the venous system in TOF

MRA protocols in the parameter range for α of 15° to 35° and TR of 20 ms to 35 ms, which are the ranges normally used at 7 T. Instead of the standard 90° saturation pulse, only half the flip angle (or even less) is necessary, substantially ameliorating SAR constraints and enabling acquisition of high resolution in acceptable imaging time.

Acknowledgment

The authors thank Lena C. Schäfer (RT) for performing all in vivo examinations.

References

1. Maderwald S, Ladd SC, Gizewski ER, Kraff O, Theysohn JM, Wicklow K, Moenninghoff C, Wanke I, Ladd ME, Quick HH. To TOF or not to TOF: strategies for non-contrast-enhanced intracranial MRA at 7 T. Magma 2008;21:159-167.

2. Nowinski WL, Puspitasaari F, Volkau I, Marchenko Y, Knopp MV. Comparison of Magnetic Resonance Angiography Scans on 1.5, 3, and 7 Tesla Units: A Quantitative Study of 3-Dimensional Cerebrovasculature. J Neuroimaging 2013;23:86-95.

3. Cho ZH, Kang CK, Han JY, Kim SH, Kim KN, Hong SM, Park CW, Kim YB. Observation of the lenticulostriate arteries in the human brain in vivo using 7.0T MR angiography. Stroke 2008;39:1604-1606.

4. Heverhagen JT, Bourekas E, Sammet S, Knopp MV, Schmalbrock P. Time-of-flight magnetic resonance angiography at 7 Tesla. Invest Radiol 2008;43:568-573.

5. Rooney WD, Johnson G, Li X, Cohen ER, Kim SG, Ugurbil K, Springer CS, Jr. Magnetic field and tissue dependencies of human brain longitudinal 1H2O relaxation in vivo. Magn Reson Med 2007;57:308-318.

6. von Morze C, Xu D, Purcell DD, Hess CP, Mukherjee P, Saloner D, Kelley DA, Vigneron DB. Intracranial time-of-flight MR angiography at 7T with comparison to 3T. J Magn Reson Imaging 2007;26:900-904.

7. Conolly S, Nishimura D, Macovski A, Glover G. Variable-rate selective excitation. J Magn Reson Imaging 1988;78:440-458.

8. Schmitter S, Bock M, Johst S, Auerbach EJ, Ugurbil K, Van de Moortele PF. Contrast enhancement in TOF cerebral angiography at 7 T using saturation and MT pulses under SAR constraints: Impact of VERSE and sparse pulses. Magn Reson Med 2012;68:188-97.

9. Kubale R, Stiegler H. Farbkodierte Duplexsonographie: interdisziplinaerer vaskulaerer Ultraschall: Thieme: 2002.

10. Ludwig M. Angiologie in Klinik und Praxis: Georg Thieme Verlag: 1998.

11. Conijn MM, Hendrikse J, Zwanenburg JJ, Takahara T, Geerlings MI, Mali WP, Luijten PR. Perforating arteries originating from the posterior communicating artery: a 7.0-Tesla MRI study. Eur Radiol 2009;19:2986-2992.

12. Hendrikse J, Zwanenburg JJ, Visser F, Takahara T, Luijten P. Noninvasive depiction of the lenticulostriate arteries with time-of-flight MR angiography at 7.0 T. Cerebrovasc Dis 2008;26:624-629.

13. Zwanenburg JJ, Hendrikse J, Takahara T, Visser F, Luijten PR. MR angiography of the cerebral perforating arteries with magnetization prepared anatomical reference at 7 T: comparison with time-of-flight. J Magn Reson Imaging 2008;28:1519-1526.

14. Bernstein MA, King KF, Zhou ZJ. Handbook of MRI pulse sequences. Amsterdam ; Boston: Academic Press: 2004.

15. Madelin G, Oesingmann N, Inglese M. Double Inversion Recovery MRI with fat suppression at 7 tesla: initial experience. J Neuroimaging 2010;20:87-92.

16. Peters AM, Brookes MJ, Hoogenraad FG, Gowland PA, Francis ST, Morris PG, Bowtell R. T2* measurements in human brain at 1.5, 3 and 7 T. Magn Reson Imaging 2007;25:748-753.

17. Koopmans PJ, Manniesing R, Niessen WJ, Viergever MA, Barth M. MR venography of the human brain using susceptibility weighted imaging at very high field strength. Magma 2008;21:149-158.

18. Johst S, Wrede KH, Schmitter S, Dammann P, Schlamann MU, Sandalcioglu IE, Sure U, Ladd SC, Ladd ME, Maderwald S. High-resolution clinical 7T

protocol for the depiction of cerebral vascular structures. Montréal, Canada, 2011. (abstract 4243).

19. von Morze C, Purcell DD, Banerjee S, Xu D, Mukherjee P, Kelley DA, Majumdar S, Vigneron DB. High-resolution intracranial MRA at 7T using autocalibrating parallel imaging: initial experience in vascular disease patients. Magn Reson Imaging 2008;26:1329-1333.

20. Schar M, Kozerke S, Fischer SE, Boesiger P. Cardiac SSFP imaging at 3 Tesla. Magn Reson Med 2004;51:799-806.

21. Hoult DI. The principle of reciprocity in signal strength calculations—A mathematical guide. Concepts in Magnetic Resonance 2000;12:173-187.

22. Parker DL, Yuan C, Blatter DD. MR angiography by multiple thin slab 3D acquisition. Magn Reson Med 1991;17:434-451.

Chapter 3 Comparison of Fat Saturation Techniques for Single-Shot Fast Spin Echo Sequences for 7-T Body Imaging*

Abstract

For T2-weighted abdominal images, homogenous fat suppression (FS) is crucial for diagnosis, but inherent B_0/B_1 inhomogeneities at 7 T lead to inhomogeneous FS and to tissue signal loss for most techniques. Here, 4 different FS techniques for single-shot fast spin echo were compared, whereby the recently proposed time-interleaved acquisition of modes (TIAMO) was used for the imaging portion of the sequence to reduce B_1 artifacts.

Fat suppression techniques included a novel method using TIAMO (TIAMO FS: multiple fat-selective 90-degree radiofrequency pulses applied with alternating transmit radiofrequency modes), slice-selective gradient reversal (SSGR), slice-selective smaller bandwidth refocusing pulses (SSB), and the combination of SSGR and SSB with TIAMO FS. Ten volunteers were examined in 6 different ways in the following order: without any FS, with TIAMO FS, with SSGR, SSGR with preceding TIAMO FS, SSB, and SSB with preceding TIAMO FS. For evaluation of the techniques, regions of interests were placed identically for all 6 protocols per volunteer in subcutaneous fat, intraabdominal fat, organs, and muscle. Overall image quality, artifacts, quality of subcutaneous/ intra-abdominal/retroperitoneal FS, and homogeneity of FS were rated over the entire field of view by 2 experienced radiologists using a 5-point scale.

Comparing the different FS techniques, only SSGR and SSGR combined with TIAMO FS led to a nearly homogeneous FS over the entire field of view and all slices. All other techniques showed severe FS inhomogeneities. Results of a radiologic evaluation confirmed the observations made by the quantitative analysis.

Of the compared techniques, the most favorable was SSGR because, here, a homogeneous FS with moderate tissue signal loss of approximately 20% was achieved with no additional preparation pulses being necessary. Using this FS technique combined with TIAMO image acquisition, delineation between fat and bright liquids in single-shot fast spin echo images, which is essential for diagnosis, is possible at 7 T.

*__Johst S__, Orzada S, Fischer A, Umutlu L, Ladd ME, Maderwald S.
“Comparison of Fat Saturation Techniques for Single-Shot Fast Spin Echo Sequences for 7-T Body Imaging”
Investigative Radiology, 2014; 49(2): 101-8.

3.1 Introduction

Homogenous fat suppression (FS) is crucial for diagnosis in T2-weighted abdominal images. Because fat is displayed with high signal intensities in single-shot fast spin echo (SSFSE) sequences, diseases also producing high signal intensities may be obscured by the bright fat signal.[1-5] Because of inherent B_0 and B_1 inhomogeneities,[6,7] abdominal imaging at 7 T is challenging[8-11] and complete FS is not easily achieved.

Various FS techniques for magnetic resonance imaging have been introduced over the years. Among others, these include spectrally selective 90-degree saturation pulses (SPS), spectral attenuated inversion recovery (SPAIR), slice-selective gradient reversal (SSGR), slice-selective smaller bandwidth refocusing pulses (SSB), and FS pulse trains, each of which is briefly described in the following paragraphs:

1) In the case of SPS 90-degree radiofrequency (RF) pulses followed by a spoiling gradient,[12,13] the RF pulses are transmitted on the fat frequency with a bandwidth small enough to not influence the water spins. This technique relies on a homogeneous B_0/B_1 distribution, which cannot be guaranteed in 7-T body imaging, leading to inhomogeneous FS over large fields of view (FOVs) (Fig. 3.1).[14] In addition, the water signal is reduced because of magnetization transfer effects,[15] especially in multislice acquisitions.

2) Another technique called SPAIR (also called spectral adiabatic inversion recovery) is based on spectrally selective adiabatic 180-degree preparation pulses followed by an inversion time aiming for the zero crossing of the fat magnetization.[5,16] Through the use of an adiabatic RF pulse, this technique is relatively robust against B_1 inhomogeneity if a certain B_1 threshold can be surpassed over the entire FOV (which can be difficult for abdominal imaging at 7 T). Once again, the water signal is reduced because of magnetization transfer effects. B_0 inhomogeneity can

also lead to imperfect FS and tissue signal suppression because of induced local shifts of fat/water frequencies.

3) For spin-echo-based imaging sequences, a technique named SSGR is applicable.[17-19] Here, the slice selection gradients of the 90-degree excitation pulse and the 180-degree refocusing pulses are applied with opposite polarity leading to opposite directions of the chemical shift, which means that no spin echo is formed from fat. This technique profits from higher field strength because the chemical shift between fat and water (3.5 ppm) gets larger. Fat suppression can be accomplished without additional scan time or specific absorption rate (SAR) contribution. Another advantage of this technique is that it can be combined with other FS techniques that rely on preparation pulses such as 1) or 2).

4) For high-field spin-echo imaging, a recently presented technique takes advantage of the increased chemical shift to omit the fat signal. The duration of the refocusing pulses is prolonged compared with the excitation pulse, whereas the time-bandwidth product (TBWP) is kept constant. In this way, the SSB diminish the amplitude of the slice-selection gradient. The lower gradient amplitude shifts the refocusing bandwidth away from the excited fat signal.[20] It has been claimed that this technique is superior to SSGR because inhomogeneity in B_0 causes the slices to bend in opposite directions during excitation and refocusing when using SSGR, leading to loss in signal-to-noise ratio.

5) More recently, a technique using a train of 3 RF pulses to suppress the fat signal in the presence of B_1 inhomogeneity was presented.[21] Similar to this approach, in the current study, we implemented a technique based on multiple spectrally selective RF preparation pulses alternating between individual transmission modes. We designate this technique time-interleaved acquisition of modes (TIAMO) FS because it is similar to the technique that we generally use for the imaging portion of sequences in abdominal imaging protocols. The principle of TIAMO[22,23] is to excite at least 2 different B_1 transmission modes using static RF shimming in an

interleaved acquisition. Overall signal homogeneity can be improved by exploiting the complementary RF patterns of the different transmission modes.

In this study, TIAMO FS, SSGR, SSB, and the combination of SSGR/SSB with TIAMO FS are compared for 7-T abdominal SSFSE imaging. Because of their previously observed inadequacy and inhomogeneity of FS in abdominal SSFSE imaging (Fig. 3.1), SPS and SPAIR were not considered in this study.

The rationale of TIAMO FS is that FS pulses played out, for example, in the same modes as used for TIAMO imaging may lead to a more homogenous FS because the TIAMO acquisition itself improves the overall image homogeneity. Because of the B_1 inhomogeneity, flip angles in the order of 90 degrees are reached only in certain areas, so playing out FS pulses multiple times with subsequent spoiling should saturate fat signals. A drawback could be tissue signal loss due to B_0 inhomogeneity. Because SSGR and SSB are FS methods that are not based on preparation pulses, both can easily be combined with TIAMO FS, which should improve the FS of the individual techniques.

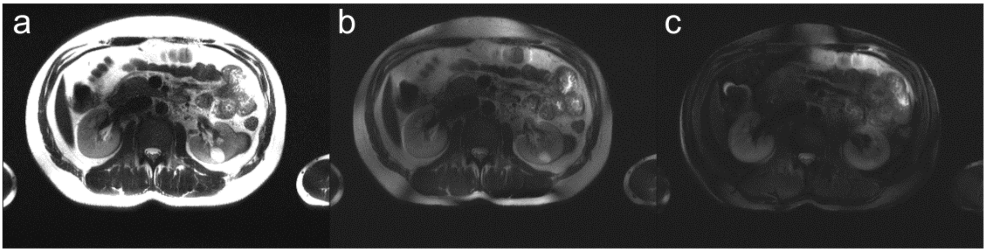

Figure 3.1. *Standard FS techniques show severe inhomogeneities in 7-T abdominal imaging: Central slice without FS (a), SPS (b), and SPAIR (c). In general, FS in the outermost slices performed worse (not shown). All images were windowed identically.*

3.2 Materials and Methods

Imaging was performed on a 7-T whole-body system (MAGNETOM 7T; Siemens Healthcare, Erlangen, Germany) equipped with a SC72 gradient coil capable of 70 mT/m of maximal amplitude, 200 mT/m per second of slew rate, and second-order B_0 shims. All volunteer examinations (N = 10) were made with a custom-built 8-channel transmit/receive body coil[24] and a custom 8-channel RF shimming and SAR supervision system capable of fast switching between different RF shim sets (amplitudes and phases).[25] A total of 3 volunteers were scanned with an additional dorsal receive array.[26]

For compliance with the International Electrotechnical Commission guidelines, SAR calculations were performed in human adult male and female body models of the Virtual Family (CST Microwave Studio, Darmstadt, Germany).[27,28] Full-wave simulations were applied with exact dimensions and characteristics of the 8-channel RF coil, and maximum permitted input power levels were calculated from the simulations of the corresponding body models. On the basis of these simulations, a standardized SAR file was integrated into the SAR monitoring system.[25] Measurements were conducted in accordance with all guidelines set forth by the approving institutional review board. Written informed consent was obtained before the examination.

Fat Suppression Techniques

Time-interleaved acquisition of modes FS uses multiple fat-selective 90-degree (nominal) RF pulses (each 3 milliseconds), each applied with different RF shims (modes) followed by spoiler gradients on each axis. Here, 6 such preparation pulses alternating between the first- and second-order circularly polarized modes (CP^+ and CP^{2+}) were chosen. A sequence diagram of TIAMO FS with TIAMO imaging is shown in Figure 3.2.

Slice-selective smaller bandwidth refocusing pulses used an excitation RF pulse duration of 2 milliseconds (the same duration and TBWP of 1.85 as used for the other techniques), and for refocusing, a duration of 4.1 milliseconds was chosen.

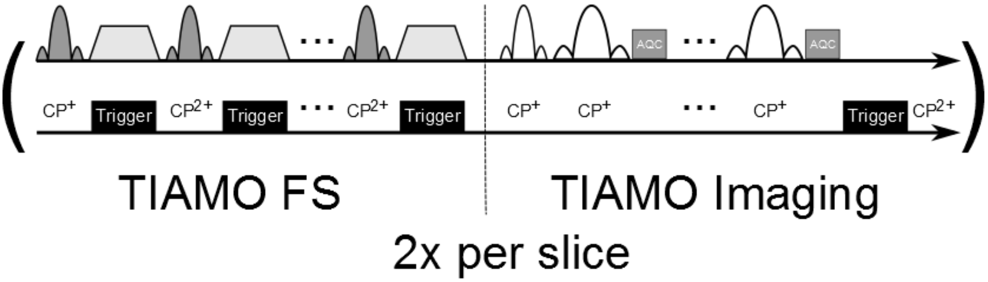

Figure 3.2. *Sequence timing for TIAMO FS. The modes of the fat-selective RF pulses are changed by triggering during the spoiler gradients. The shown part of the sequence has to be repeated twice because TIAMO imaging needs the acquisition of at least 2 modes. Triggers are placed such that the imaging part is acquired in the* CP^+ *mode in the first run and in the* CP^{2+} *mode in the second run. Slice-selective gradient reversal and SSB use the same TIAMO imaging scheme, except for changes in gradient polarity or pulse duration.*

Imaging Parameters

The image acquisition was performed with a 2-dimensional SSFSE using an FOV of 384 mm x 288 mm and a matrix of 384 x 288, resulting in a noninterpolated in-plane resolution of 1 mm x 1 mm, with a slice thickness of 5 mm. Eleven transversal slices with 150% distance factor (corresponding to a 13-cm coverage in the z-direction) were acquired. A repetition time of 1500 milliseconds, an echo time (TE) of 91 milliseconds (97 milliseconds for the SSB technique), a phase partial Fourier of 5/8, a generalised autocalibrating partially parallel acquisitions acceleration factor of R = 3, a bandwidth of 766 hertz per pixel, and a total acquisition time of 33 seconds were used. For the imaging portions of all sequences, TIAMO[22,23] with the CP^+ and CP^{2+} modes was used to address B_1 nonuniformity. No SAR reduction for the 180-degree refocusing pulses was applied. The imaging was performed in 10 volunteers (mean [SD] age, 30.4 [6.1] years; mean [SD] weight, 78.3 [11.8]; height, 1.83 [0.11]) in 6 different ways in the following order: without any FS, with TIAMO FS, with SSGR, SSGR with preceding TIAMO FS, SSB, and SSB with preceding TIAMO FS.

For evaluation of the techniques regarding FS and tissue signal preservation, 12 regions of interest (ROIs) in total were placed identically for all 6 protocols per volunteer in the central slice in subcutaneous fat (6 ROIs distributed around the body contour), intra-abdominal fat (3 ROIs in the posterior retroperitoneal space: 1 next to each kidney, 1 ROI in mesenteric fat), organs (2 ROIs, 1 in each kidney), and muscle (1 ROI in the psoas major muscle). The outermost slices were evaluated in the same way, in part, without considering the kidneys because they were not visible in all slices. The measured signals were normalized to the first scan without FS to quantify the differences between the FS techniques in an intra-individual comparison. The imaging with the 6 protocols was performed in succession so that the same B_0 shim and amplifier adjustments could be used, keeping all acquisition imaging parameters the same, which should, in general, lead to the same noise power.

Overall image quality, artifacts, quality of subcutaneous/ intra-abdominal/retroperitoneal FS, and homogeneity of FS were rated over the entire FOV by 2 experienced radiologists using a 5-point scale. The ratings of image quality are as follows: 1, excellent; 2, good; 3, moderate; 4, poor; 5, nondiagnostic. The ratings of artifacts are as follows: 1, no impairment; 2, slight; 3, moderate; 4, strong; 5, nondiagnostic. The ratings of quality of FS are as follows: 1, optimal; 2, sufficient; 3, moderate; 4, insufficient; 5, no FS. The ratings of homogeneity of FS are as follows: 1, homogeneous; 2, nearly homogeneous; 3, moderately homogeneous; 4, insufficiently homogeneous; 5, very inhomogeneous. These ratings were averaged over all volunteers and both radiologists.

To check for statistically significant differences between the different FS techniques, a t test was performed.[21]

After these evaluations, to show feasibility, the most favorable FS technique was applied in a different body region (female pelvis, 27 years/85 kg/1.78 m). Fat suppression (intra-abdominal and subcutaneous fat) and tissue signal (back muscle, bladder) was quantitatively evaluated and compared with a protocol without FS.

3.3 Results

Comparing the different FS techniques, only SSGR and SSGR combined with TIAMO FS led to a nearly homogeneous FS over the entire FOV and all slices. All other techniques showed severe FS inhomogeneities: areas with very high FS next to areas with nearly no effect on the fat signal. Figure 3.3 shows the center slices of the sequence variants using the different FS techniques for a male volunteer (same volunteer as that in Fig. 3.1) and a female volunteer. The same results could be observed in all other volunteers.

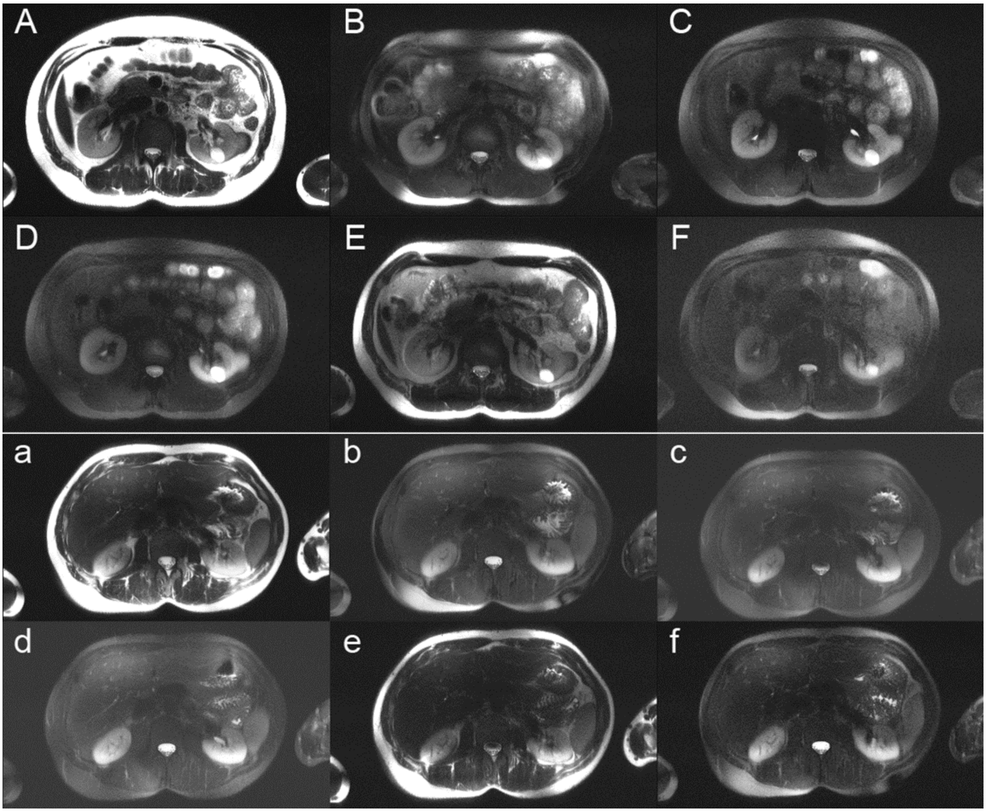

Figure 3.3. *Center slice of a male volunteer (same as in Fig. 3.1) showing known cysts in the left kidney (A-F) and of a female volunteer (a-f). Protocol without any FS (A/a), with TIAMO FS (B/b), SSGR (C/c), SSGR and TIAMO FS combined (D/d), SSB (E/e), SSB and TIAMO FS combined (F/f).*

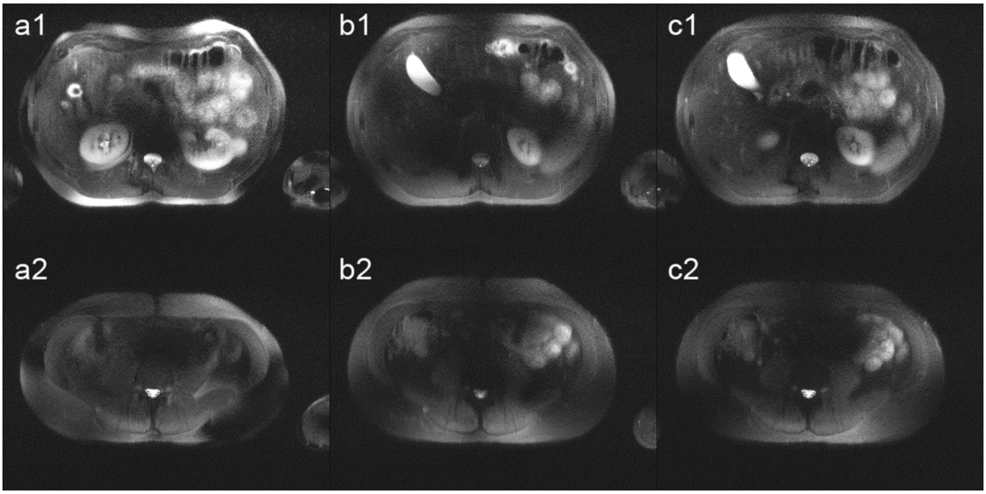

Figure 3.4. *Loss of tissue signal can be observed in the outermost slices. TIAMO FS (a1/a2), SSGR (b1/b2), and combination of SSGR and TIAMO FS (c1/c2). The same male volunteer as shown in Figures 3.1 and 3.2. Image a1 shows a slightly different anatomical position compared with images b1 and c1, presumably because of movement of the volunteer during the examination*

Generally, the outermost slices tended to show more inhomogeneities (Fig. 3.4), which was also reflected in the ratings of the effectiveness of the FS techniques.

Figure 3.5 shows signal intensities of fat and tissue measured in the central imaging slice (in 2 volunteers: Figs. 3.5A, B) relative to the sequence acquired without any FS and averaged over all measured ROIs. In all volunteers, for TIAMO FS, SSGR, and SSGR combined with TIAMO FS, the signal of the psoas major muscle was greater than or only slightly less than 80% (on average, 83.2%, 79.4%, and 77.6% with a standard deviation of approximately 7%), whereas the signal of the kidneys was greater than or only slightly less than 90% (on average, 98.2%, 89.8%, and 92.6% with a standard deviation of approximately 17%). In SSB and SSB combined with TIAMO FS, both tissue signals were relevantly less than 80% in almost all cases (for muscle/kidney, on average, 54.8%/68.3% and 49.7%/61.5% in the combined variant with a standard deviation of approximately 9%). The

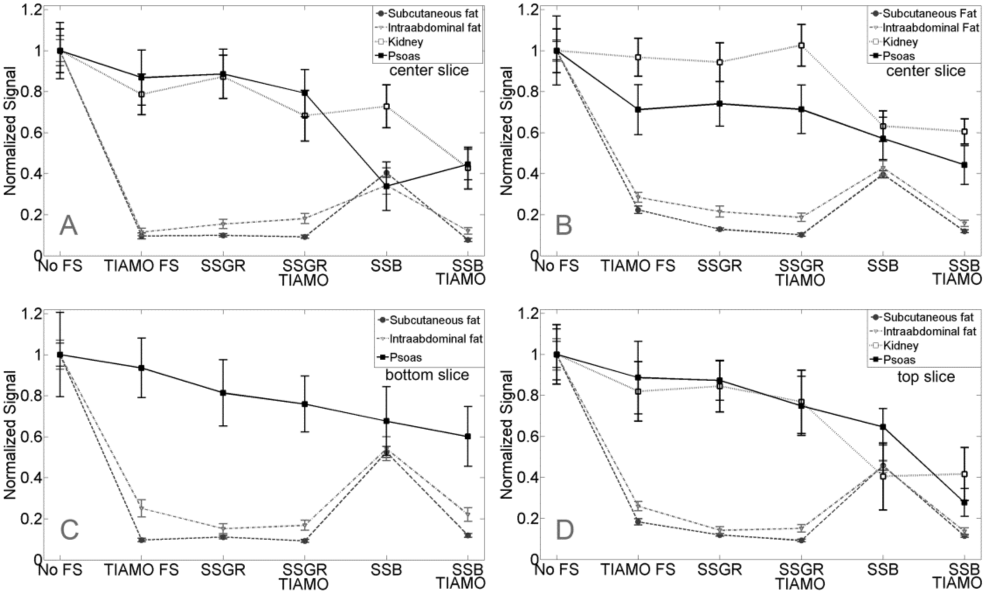

Figure 3.5. *Top row shows signal intensities of the subcutaneous/intra-abdominal fat, kidney, and psoas major muscle relative to imaging without FS and averaged over all ROIs for the central slice of a male volunteer (A) and a female (B) volunteer. Bottom row shows relative signal intensities from inferior (C)/superior slice (D) of the male volunteer. Data are from the same male and female volunteers shown in Fig. 3.3.*

combination with TIAMO FS led to a mean additional signal loss of 6%. Subcutaneous fat was suppressed best (always less than 20%) with SSGR combined with TIAMO FS and SSGR alone (10.3%/12.8%, on average), whereby the combination reached slightly lower signal values but also tended to cause slightly more tissue signal loss (approximately 2% additional suppression/ loss averaged over all volunteers). Time-interleaved acquisition of modes FS led to suppression of subcutaneous/intra-abdominal fat of approximately 20%/29% (for all volunteers except 1 where 10%/12% was reached; cf Fig. 3.5A). The worst suppression for both subcutaneous and intra-abdominal fat was reached with SSB: a reduction to only approximately 40% was possible. For SSB combined with TIAMO FS, FS was, on average, relevantly better than for SSB alone (10.9%/18.5%) and, hence, better than TIAMO FS alone. However, also, tissue signals were significantly smaller compared with all other sequence variants. For all techniques and volunteers, subcutaneous fat could be suppressed slightly better than intra-abdominal fat. Slice-selective gradient reversal and both SSGR/SSB combined with TIAMO FS could reduce intra-abdominal fat to approximately 20% (17.1%, 15.7%/18.5%, on average). Although TIAMO FS alone reached similar (Fig. 3.5A) or slightly higher (Fig. 3.5B) fat signal values, FS was not homogenous over the whole FOV (Figs. 3.3, 3.4). Applying TIAMO FS with more than 6 prepulses did not lead to better results (not shown).

Looking at the outermost slices, the results are quite similar, except that the FS techniques are slightly less effective. Slice-selective gradient reversal performed best regarding FS and tissue signal preservation. For intra-abdominal fat, relative signal values of approximately or less than 20% were reached by SSGR (except for 1 case where only 24% [2%] was reached in the most superior slice). Subcutaneous fat could be reduced by SSGR in every case to less than 17%, averaged over all volunteers to approximately 13%. In all considered slices, tissue signal was greater than or approximately 80% for SSGR, except for 1 volunteer where only 70.0% (6.7%) was reached in the most superior slice.

Considering the overall SAR, the differences between the FS techniques were negligible for 2-dimensional SSFSE because of the high number of 180-degree refocusing RF pulses in the imaging part of the sequence. Except for the techniques working with SSB, as mentioned here, the prolonged refocusing RF pulses are less demanding of SAR.

The evaluation results by the 2 radiologists showed that the overall image quality was rated between 2 and 3 (good to moderate) for all techniques. The sequence that was run without FS was rated 2.3 (0.33) averaged over all volunteers (Fig. 3.6A). Although SSGR and SSB combined with TIAMO FS were rated the highest, no relevant difference, compared with the sequence that was run without FS, was detected for any of the techniques.

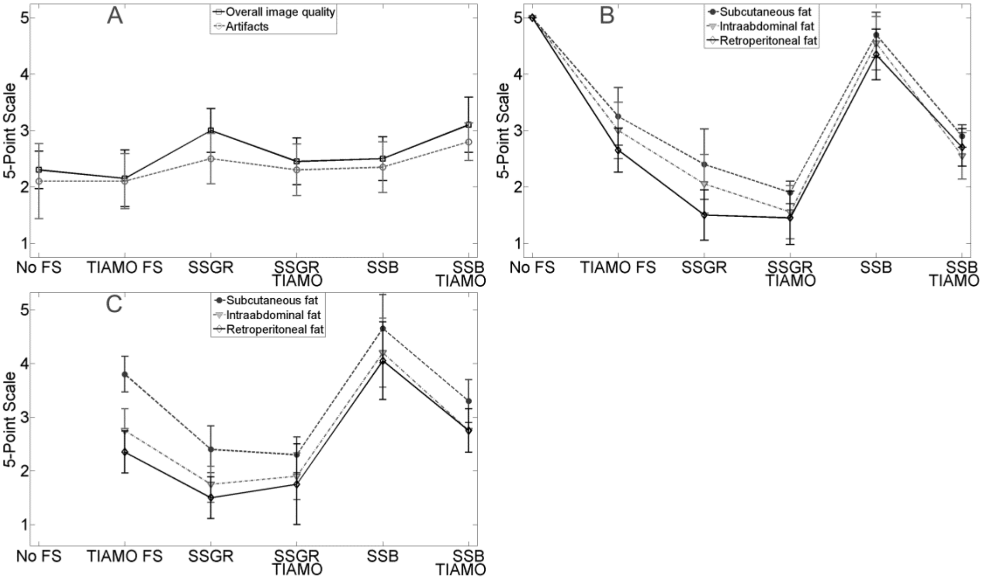

Figure 3.6. *Results of the radiologic evaluation using a 5-point scale showing the overall image quality and the overall artifacts (A), quality of FS (B), and homogeneity of FS (C). Homogeneity of FS in non-fat-suppressed image was not rated. Lower values of the 5-point scales represent more favorable ratings.*

Artifact level was relatively constant, rated only greater than 2 (slight impairment), with no relevant deviation from the value of the sequence that was run without any FS (Fig. 3.6A).

Quality of FS was rated best for SSGR and SSGR combined with TIAMO FS, with no relevant difference between the 2 techniques (Fig. 3.6B). Slice-selective smaller bandwidth refocusing pulses received values greater than 4 (insufficient), and SSB combined with TIAMO FS received approximately the same values as that for TIAMO FS alone.

Regarding homogeneity of the FS, SSGR and SSGR combined with TIAMO FS reached the lowest values, whereas SSB was rated relevantly higher for all fat types (Fig. 3.6C). Homogeneity of FS was not rated for the images without any FS. For subcutaneous fat, both TIAMO FS and SSB combined with TIAMO FS reached relevantly higher values than the other techniques did. For all techniques, subcutaneous fat had the highest values of all fat types and retroperitoneal had the lowest.

Adding up the evaluated categories for an overall rating of the FS techniques, SSGR and SSGR combined with TIAMO FS reached the lowest values (mean [SD],17.1 [1.4]/15.6 [2]), whereas TIAMO FS and SSB combined with TIAMO FS performed very similar (mean [SD], 22.1 [1.8]/22.85 [1.4]) and SSB alone reached the highest value of all FS techniques (mean [SD], 31.4 [3.1]).

To test for statistically significant differences between the FS techniques, a t test was performed. The resulting P values provided an estimation for the significance of differences, and P values less than 0.05 can be considered as statistically significant. For tissue signals, the results of the t test showed that there is no statistically significant difference between tissue signal acquired without FS and with TIAMO FS ($P > 0.23$). Comparing SSGR with SSGR combined with TIAMO FS/TIAMO FS alone, no significant difference could be found ($P > 0.99$/$P > 0.98$). Slice-selective gradient reversal combined with TIAMO FS and TIAMO FS alone are not significantly different but only marginal with $P > 0.05$. Slice-selective smaller bandwidth refocusing pulses compared with SSB combined with TIAMO FS showed no significant difference ($P > 0.48$). Every comparison not mentioned here showed a significant difference or a highly significant difference ($P < 0.01$) in most cases.

Regarding fat, the results of the t test revealed that SSGR and SSGR combined with TIAMO FS compared with SSB combined with TIAMO FS showed no significant differences ($P > 0.99$ for both). The remaining differences were (highly) significant.

For the t test results of the qualitative evaluation, mean values averaged over both radiologists and all categories were analyzed. No significant differences comparing SSB combined with TIAMO FS and TIAMO FS alone ($P > 0.99$) were found. The same results also apply for SSGR and SSGR combined with TIAMO FS

(P > 0.28). The differences between the other sequence variants were statistically highly significant.

To show feasibility, the protocol was additionally applied for pelvic imaging in a female volunteer (Fig. 3.7). Here, the conclusions made from the FS comparison could be confirmed. For SSGR, the fat signal was substantially suppressed (subcutaneous fat, 11.7% [0.6%]; intra-abdominal fat, 10.9% [0.2%]) and tissue signal was largely preserved (back muscle, 75.0% [12.9%]; bladder, 129% [37%]). Because of the sufficient FS, a small amount of fluid in the recto-uterine pouch can be better visualized compared with the image without FS.

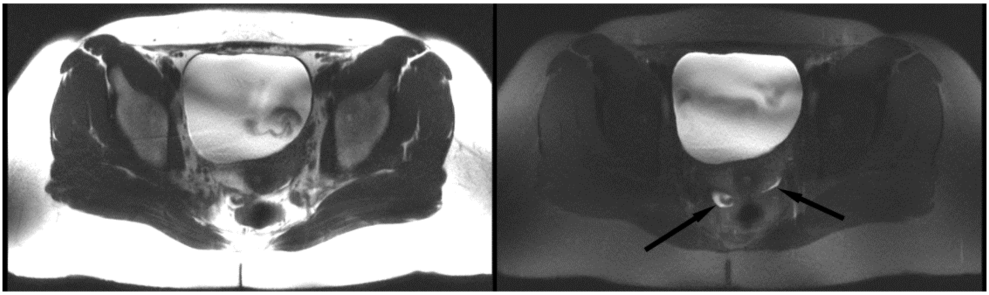

Figure 3.7. *Single-shot fast spin echo imaging of the pelvis without FS (left) and with SSGR (right). Black arrows show a small amount of fluid in the recto-uterine pouch, which is better visualized after FS.*

3.4 Discussion

The inherent B_0 inhomogeneities of 7-T abdominal imaging lead to a general loss of tissue signal when using different FS techniques. Techniques that use preparation pulses, such as TIAMO FS, tend to weaken the tissue signal because of B_0 inhomogeneity and magnetization transfer effects.[15] In the version proposed here (using the same 2 modes that are also used for the imaging portion), the technique was not suited to balance the inherent inhomogeneous flip angle distribution (Fig. 3.3). Fat suppression could be improved compared with SPS but only in certain areas, simultaneously generating loss of tissue signal (Figs. 3.4, 3.5). Here, calculating individual FS modes based on absolute B_1 maps might lead to better results with this technique. However, because the acquisition of reliable absolute abdominal B_1 maps is currently not easily achieved (because of, among other factors, limited RF power), this variant could not be evaluated yet. Recently, at the 21st Annual Meeting of the International Society of Magnetic Resonance in Medicine 2013, a concept using absolute B_1^+ mapping in the abdomen at 7 T was presented.[29] After implementation of such technique, individual FS modes based on absolute B_1 maps could be examined in future studies. In general, one can see that, because of the limited RF power, in the central region of the FOV, only relatively low signal intensities are reached despite the use of TIAMO imaging (Fig. 3.3).

Of the techniques that led to satisfying FS with acceptable tissue signal decrease, SSGR was the most favorable technique because it showed the most homogeneous and satisfying FS with no additional preparation pulses being necessary. Here, only the gradient of the 90-degree excitation pulse is switched, together with the spoiling gradient. The following 180-degree pulses are played in the same way as in the other sequence variants. Hence, intensified eddy currents could, at most, influence the first echo. Therefore, the influence of additional eddy currents is not considered relevant. The moderate tissue signal loss may be induced by B_0 inhomogeneities combined with the gradient reversal: the B_0 inhomogeneities leading to the excitation of bent slices and the gradient reversal leading to the refocusing of slices that are bent in the opposite direction, such that the signal of spins that are not in the refocused slice does not contribute to the imaged signal. Here, the implementation of slice-dependent B_0 shimming[30-32] or the installation of higher B_0 shim orders[33] could lead to a better tissue signal preservation without losing FS abilities; however, ultimately, one has to deal with varying magnetic fields arising from eddy currents.

Slice-selective smaller bandwidth refocusing pulse showed the largest signal decrease for nonfat tissue of all compared techniques. On the one hand, this is mostly caused by the longer TE that has to be chosen to apply the prolonged refocusing pulses. On the other hand, this may be also caused by the improper slice refocusing induced by the different gradient amplitudes that are used for excitation and refocusing pulses that possess different bandwidth. By using slice-dependent B_0 shimming, the latter effect might be reduced. Slice-selective smaller bandwidth refocusing pulses was also the technique with the worst FS. The reason for this may be that the displacement between fat and water induced by the different gradient amplitudes during the prolonged refocusing pulses is not high enough because of the severe B_0 inhomogeneities at 7 T that strongly distort the slice profiles. Apart from using higher B_0 shim orders/ slice-dependent B_0 shimming to ameliorate the B_0 inhomogeneities, the displacement could be improved either by the use of RF pulses with lower TBWPs, which would mean worse slice profiles, or by further prolongation of the refocusing pulses, which would lead to even longer TE and, thus, to overall signal loss in both cases. It has been claimed, at least for head imaging, that this technique would be superior to SSGR.[20] As mentioned here, the refocusing pulses could not be further optimized, and this advantage versus SSGR could not be confirmed. For the chosen imaging protocol, with SSGR, the distance between excited fat signal and refocusing fat bandwidth is intrinsically high because of the change of gradient polarity, without the need to change the RF pulses and/or prolonging TE.

The combination of the FS techniques with TIAMO FS led to a slight improvement in FS in almost all cases (6 of 10) but also to a slight additional loss of tissue signal. Regarding fat signals, SSGR and both SSGR/SSB combined with TIAMO FS led to a sufficient overall FS (Fig. 3.5); however, in the case of SSB with

TIAMO FS, the suppression was not homogeneously distributed over the entire FOV because TIAMO FS itself did not lead to a homogeneous FS (Figs. 3.3, 3.6C). Also, SSB and the combination with TIAMO FS caused the largest tissue signal loss of all compared FS variants.

Generally, the outermost slices are more prone to inhomogeneous FS and signal decrease (Fig. 3.4) because they are farther away from the center and thus suffer more from improper slice refocusing and B_1/B_0 inhomogeneities. Nevertheless, the conclusions made from the central slice could be confirmed. Even for these outlying slice positions, SSGR would be the most favorable technique because it is only slightly less effective than in the central slices.

The results of the radiologic evaluation (Fig. 3.6) confirmed the observations made by the quantitative analysis (Fig. 3.5) that SSGR and SSGR combined with TIAMO FS did best regarding FS and homogeneity of FS, with both variants reaching values less than or approximately equal to 2 (sufficient/nearly homogeneous), which should be enough to distinguish between fatty tissue and bright lesions. Looking at the overall image quality and artifact impairment, all techniques were rated approximately the same, but no technique was able to reach values less than 2 (good/slight impairment), not even imaging without FS. To further improve image quality, higher amplifier power would be beneficial. Also, choosing a broader slice profile for the refocusing pulses could lead to higher signals.

Only TIAMO FS led to tissue signals that did not differ significantly from imaging without FS. Combining SSGR/SSB with TIAMO FS did not lead to significant additional signal losses. Hence, the effects leading to tissue signal loss did not add up relevantly if FS techniques are combined. Comparing SSGR with TIAMO FS, no statistically significant tissue difference was found, but because the P value was very close to 0.05, it is probable that the difference would get significant if a higher number of volunteers would be examined. Taking also the t test results of the qualitative evaluation into account, where the overall performance of SSGR and SSGR combined with TIAMO FS was significantly better than that of TIAMO FS, the conclusion can be drawn that SSGR is the most favorable FS technique; especially because there was no significant gain by combining SSGR with TIAMO FS.

The additional scan in the pelvis of a female volunteer showed the feasibility of the SSGR FS technique. An evaluation in patients could be examined in future studies.

In summary, this study shows that most FS techniques lead to inhomogeneous FS and to tissue signal loss at 7 T. Of the compared techniques, the most favorable was SSGR because, here, a homogeneous FS with only moderate tissue signal loss is possible. This technique has the additional advantage that it does not depend on additional preparation pulses, thus allowing, in general, for more SAR- and time-efficient protocols, especially if implemented in non-single-shot spin echo sequences where FS pulses are normally applied to a greater extent. Using this FS technique combined with TIAMO image acquisition, delineation between fat and bright liquids in SSFSE images, which is essential for diagnosis, is possible at 7 T.

Acknowledgment

The authors thank Michael Schwarz and Jan Snagowski of the Department of General Psychology: Cognition, University of Duisburg-Essen, Duisburg, Germany, for their support on the statistical analysis.

References

1. Delfaut EM, Beltran J, Johnson G, Rousseau J, Marchandise X, Cotten A. Fat suppression in MR imaging: techniques and pitfalls. Radiographics 1999;19:373-382.

2. Lu DS, Saini S, Hahn PF, Goldberg M, Lee MJ, Weissleder R, Gerard B, Halpern E, Cats A. T2-weighted MR imaging of the upper part of the abdomen: should fat suppression be used routinely? AJR Am J Roentgenol 1994;162:1095-1100.

3. Kanematsu M, Hoshi H, Itoh K, Murakami T, Hori M, Kondo H, Yokoyama R, Nakamura H. Focal hepatic lesion detection: comparison of four fat-suppressed T2-weighted MR imaging pulse sequences. Radiology 1999;211:363-371.

4. Low RN, Ma J, Panchal N. Fast spin-echo triple-echo Dixon: initial clinical experience with a novel pulse sequence for fat-suppressed T2-weighted abdominal MR imaging. J Magn Reson Imaging 2009;30:569-577.

5. Lauenstein TC, Sharma P, Hughes T, Heberlein K, Tudorascu D, Martin DR. Evaluation of optimized inversion-recovery fat-suppression techniques for T2-weighted abdominal MR imaging. J Magn Reson Imaging 2008;27:1448-1454.

6. Hoult DI, Phil D. Sensitivity and power deposition in a high-field imaging experiment. J Magn Reson Imaging 2000;12:46-67.

7. Van De Moortele PF, Akgun C, Adriany G, Moeller S, Ritter J, Collins CM, Smith MB, Vaughan JT, Ugurbil K. B-1 destructive interferences and spatial phase patterns at 7 T with a head transceiver array coil. Magn Reson Med 2005;54:1503-1518.

8. Vaughan TT, Snyder CJ, DelaBarre LJ, Bolan PJ, Tian J, Bolinger L, Adriany G, Andersen P, Strupp J, Ugurbil K. Whole-Body Imaging at 7T: Preliminary Results. Magn Reson Med 2009;61:244-248.

9. Umutlu L, Bitz AK, Maderwald S, Orzada S, Kinner S, Kraff O, Brote I, Ladd SC, Schroeder T, Forsting M, Antoch G, Ladd ME, Quick HH, Lauenstein TC. Contrast-enhanced ultra-high-field liver MRI: A feasibility trial. Eur J Radiol;2013:760-767.

10. Umutlu L, Maderwald S, Kinner S, Kraff O, Bitz AK, Orzada S, Johst S, Wrede K, Forsting M, Ladd ME, Lauenstein TC, Quick HH. First-pass contrast-enhanced renal MRA at 7 Tesla: initial results. Eur Radiol 2013;23:1059-1066.

11. Moser E, Stahlberg F, Ladd ME, Trattnig S. 7-T MR-from research to clinical applications? Nmr Biomed 2012;25:695-716.

12. Rosen BR, Wedeen VJ, Brady TJ. Selective saturation NMR imaging. J Comput Assist Tomogr 1984;8:813-818.

13. Haase A, Frahm J, Hanicke W, Matthaei D. 1H NMR chemical shift selective (CHESS) imaging. Phys Med Biol 1985;30:341-344.

14. Bley TA, Wieben O, Francois CJ, Brittain JH, Reeder SB. Fat and water magnetic resonance imaging. J Magn Reson Imaging 2010;31:4-18.

15. Shin W, Gu H, Yang Y. Incidental magnetization transfer contrast by fat saturation preparation pulses in multislice Look-Locker echo planar imaging. Magn Reson Med 2009;62:520-526.

16. Kaldoudi E, Williams SC, Barker GJ, Tofts PS. A chemical shift selective inversion recovery sequence for fat-suppressed MRI: theory and experimental validation. Magn Reson Imaging 1993;11:341-355.

17. Park HW, Kim DJ, Cho ZH. Gradient reversal technique and its applications to chemical-shift-related NMR imaging. Magn Reson Med 1987;4:526-536.

18. Volk A, Tiffon B, Mispelter J, Lhoste JM. Chemical shift-specific slice selection. A new method for chemical shift imaging at high magnetic field. J Magn Reson 1987;71:168–174.

19. Gomori JM, Holland GA, Grossman RI, Gefter WB, Lenkinski RE. Fat suppression by section-select gradient reversal on spin-echo MR imaging. Work in progress. Radiology 1988;168:493-495.

20. Ivanov D, Schafer A, Streicher MN, Heidemann RM, Trampel R, Turner R. A simple low-SAR technique for chemical-shift selection with high-field spin-echo imaging. Magn Reson Med 2010;64:319-326.

21. Rasch D, Guiard V. The robustness of parametric statistical methods. Psychology Science 2004;46:175-208.

22. Orzada S, Maderwald S, Poser BA, Bitz AK, Quick HH, Ladd ME. RF excitation using time interleaved acquisition of modes (TIAMO) to address B1 inhomogeneity in high-field MRI. Magn Reson Med 2010;64:327-333.

23. Orzada S, Maderwald S, Poser BA, Johst S, Kannengiesser S, Ladd ME, Bitz AK. Time-interleaved acquisition of modes: an analysis of SAR and image contrast implications. Magn Reson Med 2012;67:1033-1041.

24. Orzada S, Quick HH, Ladd ME, Bahr A, Bolz T, Yazdanbakhsh P, Solbach K, Bitz A. A flexible 8-channel transmit/receive body coil for 7 T human imaging. Paper presented at: ISMRM 17th Annual Meeting Honolulu, Hawai, USA, 2009. (abstract 2999).

25. Bitz AK, Brote I, Orzada S, Kraff O, Maderwald S, Quick HH, Yazdanbakhsh P, Solbach K, Bahr A, Bolz T, Wicklow K, Schmitt F, Ladd ME. An 8-channel add-on RF shimming system for whole-body 7 tesla MRI including real-time SAR monitoring. Paper presented at: ISMRM 17th Annual Meeting Honolulu, Hawai, USA, 2009. (abstract 4767).

26. Pradhan R, Bitz AK, Maderwald S, Kraff O, Ladd ME, Orzada S. A 12 channel dorsal receive-only body array for 7T. Paper presented at: ISMRM 21th Annual Meeting Salt Lake City, (abstract 4393).

27. Ackerman MJ, Spitzer VM, Scherzinger AL, Whitlock DG. The Visible Human data set: an image resource for anatomical visualization. Medinfo 1995;8 Pt 2:1195-1198.

28. Christ A, Kainz W, Hahn EG, Honegger K, Zefferer M, Neufeld E, Rascher W, Janka R, Bautz W, Chen J, Kiefer B, Schmitt P, Hollenbach HP, Shen J, Oberle M, Szczerba D, Kam A, Guag JW, Kuster N. The Virtual Family--development of surface-based anatomical models of two adults and two children for dosimetric simulations. Phys Med Biol 2010;55:N23-38.

29. Cloos MA, Lee W, Wiggins GC, Sodickson D. Asymmetric Spokes: A Demonstration of Free-Breathing PTX in the Human Torso at 7T. In: Proceedings of the 21th Annual Meeting of ISMRM, Salt Lake City, USA, 2013. (abstract 4258).

30. Morrell G, Spielman D. Dynamic shimming for multi-slice magnetic resonance imaging. Magn Reson Med 1997;38:477-483.

31. Koch KM, McIntyre S, Nixon TW, Rothman DL, de Graaf RA. Dynamic shim updating on the human brain. J Magn Reson 2006;180:286-296.

32. Sengupta S, Welch EB, Zhao Y, Foxall D, Starewicz P, Anderson AW, Gore JC, Avison MJ. Dynamic B0 shimming at 7 T. Magn Reson Imaging 2011;29:483-496.

33. Pan JW, Lo KM, Hetherington HP. Role of very high order and degree B0 shimming for spectroscopic imaging of the human brain at 7 tesla. Magn Reson Med 2012;68:1007-1017.

Chapter 4 Sequence Comparison for Non-enhanced MRA of the Lower Extremity Arteries at 7 Tesla*

Abstract

In this study three sequences for non-contrast-enhanced MRA of the lower extremity arteries at 7 T were compared. Cardiac triggering was used with the aim to reduce signal variations in the arteries. Two fast single-shot 2D sequences, a modified Ultrafast Spoiled Gradient Echo (UGRE) sequence and a variant of the Quiescent-Interval Single-Shot (QISS) sequence were triggered via phonocardiogram and compared in volunteer examinations to a non-triggered 2D gradient echo (GRE) sequence. For image acquisition, a 16-channel transmit / receive coil and a manually positionable AngioSURF table were used. To tackle B_1 inhomogeneities at 7 T, Time-Interleaved Acquisition of Modes (TIAMO) was integrated in GRE and UGRE. To compare the three sequences quantitatively, a vessel-to-background ratio (VBR) was measured in all volunteers and stations. In conclusion, cardiac triggering was able to suppress flow artifacts satisfactorily. The modified UGRE showed only moderate image artifacts. Averaged over all volunteers and stations, GRE reached a VBR of 4.18 ± 0.05, UGRE 5.20 ± 0.06, and QISS 2.72 ± 0.03. Using cardiac triggering and TIAMO imaging technique was essential to perform non-enhanced MRA of the lower extremities vessels at 7 T. The modified UGRE performed best, as observed artifacts were only moderate and the highest average VBR was reached.

***Johst S**, Orzada S, Fischer A, Schäfer LC, Nassenstein K, Umutlu L, Lauenstein TC, Ladd ME, Maderwald S.
"Sequence Comparison for Non-enhanced MRA of the Lower Extremity Arteries at 7 Tesla"
PLOS ONE, 2014; 9(1): e86274.

4.1 Introduction

For the diagnosis of diseases of the lower extremity vasculature, digital subtraction angiography (DSA) is increasingly performed only in cases where contrast-enhanced MR angiography (CE MRA) has showed positive findings.[1] Recent publications indicate, however, that especially patients with severe renal dysfunction should not be examined with Gadolinium (Gd)-based contrast agents due to reported cases of Nephrogenic Systemic Fibrosis (NSF) after the administration of such contrast agents.[2,3] Accordingly, in recent years several publications have focused on the evaluation of non-enhanced MRA sequences as an alternative to DSA / CE MRA for the diagnosis of lower extremity vascular diseases.[1,4-8]

It has been shown that non-enhanced MRA techniques seem to profit from 7 T, especially in the head.[9,10] But in order to perform non-contrast-enhanced MRA at 7 T, one has to counter challenging issues such as B_0 and B_1 inhomogeneities,[11,12] particularly when considering body imaging.[13,14] To tackle the latter issue, a recently published technique, Time-Interleaved Acquisition of Modes (TIAMO),[15,16] was used for this study. The principle is to excite at least two different B_1 transmission modes using static radiofrequency (RF) shimming in an interleaved acquisition. Overall signal homogeneity can be improved by exploiting the complementary radiofrequency patterns of the different transmission modes. Data from e.g. two acquisitions are not just averaged, but reconstructed the same way as if twice the number of coils would have been used. By that considerably more homogeneous images can be created.

Further, for non-enhanced MRA at 7 T there is a need for heartbeat triggering due to a periodic variation in the signal intensity of the arteries that was observed in [17]. The most likely reason is interference between image acquisition frequency and heartbeat frequency. Using cardiac triggering combined with single-shot sequences acquiring the center of k-space at approximately the same time point of the cardiac cycle should be possible and thereby reduce the observed signal variations. In clinical routine at lower field strengths, ECG triggering is commonly used. Unfortunately, ECG triggering is severely limited at 7 T due to an elevated

T wave and other interferences.[18] To avoid this issue, acoustic cardiac triggering can be used.[19-21]

In [17] a 2D GRE sequence capable of TIAMO imaging was used. Here, a trigger pulse changes the excitation mode directly after every excitation pulse which means that both modes needed for a complete slice are acquired in an interleaved fashion (Fig. 4.1 top). Venous saturation pulses were applied every TR. MRA image contrast is created by saturating the background tissue via the excitation RF pulses and by inflowing unsaturated arterial blood spins which provide hyperintense signal. In this study, to avoid the reported blood signal fluctuations, two single-shot sequences were chosen to be combined with cardiac triggering:

(1) An Ultrafast Spoiled Gradient Echo (UGRE) sequence (a modified turboFLASH sequence without T_1 contrast preparing inversion RF pulse) where the cardiac trigger starts the acquisition of a complete slice. This is repeated for the second TIAMO mode after the next cardiac trigger event. Venous saturation pulses are applied only sparsely (Fig. 4.1 middle). Image contrast is created the same way as in GRE, but UGRE is designed for quite fast 2D single-shot acquisitions.

(2) A variant of the Quiescent-Interval Single-Shot (QISS)[22] sequence which is available as vendor-provided work in progress and used at 1.5T. Here, three 90° saturation RF pulses prepare the image contrast. The first one saturates the tissue signal in the imaging slice, the second one suppresses the veins and the third one suppresses fat signals. After the second preparation pulse, a time interval QI is introduced to give the unsaturated arterial blood spins time to enter the imaging slice before one complete slice is acquired (Fig. 4.1 bottom). As the QISS sequence is a vendor-provided work-in-progress at 7 T, no source code was available and TIAMO could not be implemented. Both UGRE and QISS were triggered via phonocardiogram and compared in volunteer examinations to a non-triggered 2D gradient echo (GRE) sequence similar to the one used in [17].

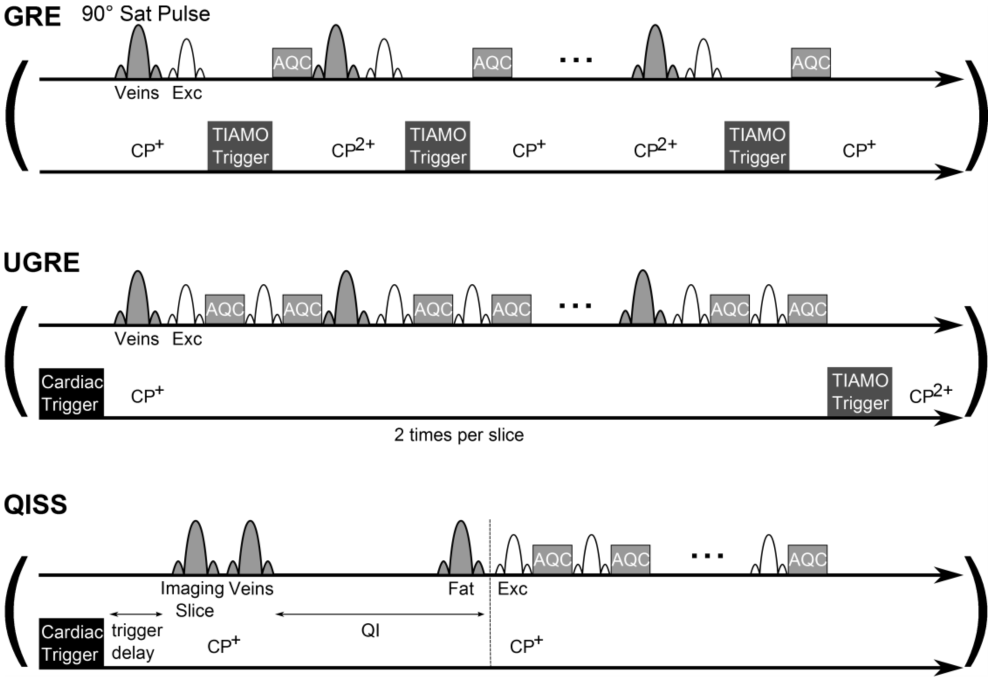

Figure 4.1. Sequence diagrams of GRE, UGRE and QISS. *In GRE, no cardiac triggering is used. Here, the TIAMO trigger changes the excitation mode directly after every excitation pulse, which means that both modes needed for a complete slice are acquired in an interleaved fashion. Saturation pulses are applied every TR. In UGRE, the cardiac trigger event starts the acquisition of a complete slice in a single shot. Due to TIAMO, this acquisition has to be repeated to acquire the same slice with the second mode. Venous saturation RF pulses are applied only sparsely. QISS uses three different saturation pulses to prepare the image contrast: In the imaging slice to suppress background tissue, a travelling venous saturation pulse below the imaging slice and a fat saturation pulse in the imaging slice. After the venous saturation, a time interval QI allows unsaturated arterial blood spins to enter the imaging slice. No saturation pulses are applied during the single-shot slice acquisition. The duration of the trigger events is shorter than pictured in these diagrams.*

The rationale of choosing UGRE and QISS is that both implementations used here are based on a GRE readout - techniques based on steady-state free precession (SSFP) like [6] are challenging at 7 T due to the inherent B_0 inhomogeneities). QISS produces promising results at lower field strength,[5] but relies on multiple preparation pulses which might be less effective at 7 T due to the inherent B_1 inhomogeneities. In contrast to QISS, the implemented version of the UGRE uses just inherent saturation effects of the GRE readout and no preparation RF pulses to generate the basic MRA contrast. This might provide sufficient contrast even in areas were desired flip angles cannot be met. Additionally, UGRE is more time-efficient because no time interval QI is necessary. By that, higher flexibility in dealing with different heart rates should be possible.

4.2 Materials and Methods

Ethics Statement

The study was conducted in conformance with the Declaration of Helsinki and approved by the Ethics Commission of the Medical Faculty of the University Duisburg-Essen (study number 11-4898-BO). Written informed consent was obtained from each volunteer before the examination.

Measurement configuration

Examinations were performed on a 7 T whole-body system (Magnetom 7T, Siemens, Erlangen, Germany) with a 16-channel transmit / receive coil based on.[23] Five stripline meander elements were placed dorsally on the patient table and eleven meander elements were placed on a rigid, semicircular former above the table. A RF shimming system with 8 channels similar to [24] was used to drive the coil with an 8-channel variable power combiner (VPC) interfaced to a 16-channel Butler matrix. Eight of the 16 inputs of the 16-channel Butler matrix corresponding to the highest transmit signal in the corresponding transmit modes were connected to the VPC.[23,25] In this way the 8-channel transmit system could be used to drive a 16-channel coil. The same configuration as in [17] was used.

Image acquisition was performed with a AngioSURF table[26,27] with 2 m length by positioning the volunteers feet-first supine and manually moving the AngioSURF table to all required body positions through the RF coil, which remained stationary at the isocenter connected to the original patient table. To reduce total acquisition time (TA), a general B_0 shim that was determined at the uppermost station was used for all stations.[17]

For compliance with the International Electrotechnical Commission (IEC) guidelines, SAR calculations (CST Microwave Studio, Darmstadt, Germany) were performed in human adult male and female body models of the Virtual Family and the Visible Human.[28,29] Full-wave simulations were applied with exact dimensions and characteristics of the 16-channel RF coil, and maximum permitted input power levels for each station were calculated from the simulations of the corresponding body models. Based on these simulations, a standardized SAR file was integrated into the SAR monitoring system.[24]

Periodic vessel signal fall-offs over short segments, particularly observable in coronal MIP images, were reported in [17]. To counter this issue, triggering with a phonocardiogram[19-21] was used for UGRE and QISS imaging. As both sequences acquire individual slices in single-shot acquisition started by the cardiac trigger event, the center of k-space can be acquired in approximately the same time point of the cardiac cycle. To compare the impact on the artifact, GRE is acquired without cardiac triggering.

Consistent signal loss in the middle third of the thigh were observed in [17], which is suspected to be caused by RF wave interferences within the FOV due to the variable anatomy of pelvis and legs along the longitudinal axis. In those volunteers where the aforementioned problem was encountered, dedicated TIAMO shims[16] were calculated based on acquired B_1^+ maps in the same imaging position. The two shims were calculated to adjust the phases of the 8 transmit channels in such a way that in one shim the B_1^+ was maximized in a circular region of interest around the right superficial femoral artery, while in the other shim the B_1^+ in a circular region of interest around the left superficial femoral artery was maximized. The remaining stations were acquired by combining the CP^+ and CP^{2+} modes, the first- and second-order circularly-polarized modes.

Sequence modifications

TIAMO imaging was implemented in the UGRE sequence code by enabling trigger pulses that cause the RF shimming system to switch between the different modulator states. As the UGRE protocol is intended to acquire one slice in a single shot between two heartbeats, the TIAMO trigger was set after each acquired imaging slice. In this way, the same slice is acquired with the two imaging modes sequentially before the next slice is excited and acquired with both modes sequentially.

Additionally, the UGRE sequence had to be further modified. RF pulses for the suppression of the venous system were implemented into the sequence. To minimize the duration of the protocol and to be able to adjust the required TR to the heartbeat rate of the volunteers, saturation pulses could be applied sparsely (i.e. only every n-th line of k-space, where n can be flexibly chosen in the protocol). The normally used saturation pulse was exchanged with another sinc pulse with lower time-bandwidth product (TBWP) (3.6 instead of 7.8). Thus, a shorter pulse was achieved without increasing its SAR contribution at the cost of the exactness of the excitation profile, which is not relevant as long as the suppression ability is not affected. A flexible RF saturation pulse duration was implemented between 800 µs and 5000 µs with a default value of 3840 µs. For further reduction of the TR, the duration of the spoiling gradients following the saturation RF was made flexible (500 µs to 2000 µs).

As the QISS sequence is a vendor-provided work-in-progress at 7 T, no source code was available and no modifications could be implemented. Hence, TIAMO imaging could not be realized, and the protocol was run with the CP^+ mode of the 16-channel coil and 1 average instead of the two or more that are necessary for TIAMO. The original QISS sequence proposed by Hodnett et al.[5] used a steady-state free precession (SSFP) readout. In this study, a GRE readout was used to avoid known artifacts and SAR limitations of SSFP at 7 T.[30]

Imaging protocols

All protocols used a nominal flip angle of 80° and a FOV of 384 mm by 288 mm to acquire 60 transversal slices with 2 mm thickness using a matrix of 384 by 288 pixels and thus an in-plane resolution of 1 mm^2. Parallel image acceleration with a GRAPPA factor of 4 utilizing 32 integrated auto-calibration lines was used. To account for inaccuracies in the manual positioning of the AngioSURF table, the different stations were scanned with an overlap that for an exact shift would lead to the lowermost 10 slices being overlapped with the uppermost 10 slices of the subsequent station. Slice overlap, which is routinely applied e.g. in time-of-flight MRA or QISS, was not used; slices within a station were acquired with no overlap (distance factor = 0) to allow for a faster coverage. Separate from the parameters that were kept the same for all three techniques, the protocols were adapted individually to the shortest TE / TR possible without affecting image quality / contrast.

Currently we are limited to 8 kW power which is not enough to perform abdominal imaging with arbitrary flip angles. Here, we used 80% of the maximum available power or 100% of the available peak power (which in this case corresponds to a nominal flip angle of 80° in the protocol). We concluded from preceding volunteer measurements that this power level gives us satisfying MRA contrast.

GRE: TR was set to 14 ms, TE to 5.26 ms, and the bandwidth to 1300 Hz/px. Image slices were acquired sequentially and in ascending order (feet to head) additionally using flow compensation. A RF pulse of nominal 90° for the suppression of the veins was applied every TR with a thickness of 116 mm and positioned at a distance of 10 mm below the imaging slice, travelling with the current slice position. TIAMO imaging[15,16] used CP^+ and CP^{2+} except for the stations of the upper thigh in volunteers where dedicated TIAMO shims had to be calculated. Hence, every slice was acquired twice. The TIAMO trigger changes excitation mode after every excitation RF pulse. The total acquisition time per station (12 cm coverage) amounted to 2 min 41 s.

UGRE: A TR of 700 ms per slice, a TE of 3.45 ms, and a bandwidth of 930 Hz/px were chosen. Image slices were acquired sequentially and in ascending order using flow compensation. Due to shorter flow compensation gradients, a shorter TE than in GRE could be reached; UGRE also used shorter spoiling gradients for remaining transversal magnetization than GRE. No inversion RF pulses for contrast preparation were used. The same RF pulse settings for venous suppression as in the GRE protocol were used except that the duration was only 2000 µs instead of 3840 µs and a pulse was applied only every 2nd excitation and using a shortened spoiler gradient of 1 ms length with a gradient moment of about 18 ms mT/m compared to 135 ms mT/m and ~ 6 ms duration in the original implementation and 15 ms mT/m in ~ 0.5 ms in GRE. TIAMO imaging[15,16] again used the CP^+ and CP^{2+} modes except for the stations of the upper thigh in volunteers where dedicated TIAMO shims had to be calculated. The sequence was gated by using the acoustic cardiac triggering device in such a way that one complete slice was acquired after the trigger signal. Due to TIAMO, each slice has to be acquired twice to combine both modes. In this protocol the two modes are acquired consecutively. After a single trigger signal, one complete slice is acquired in the first mode before the same slice excited by the second mode follows after the next trigger event. Total acquisition time for each station was on average ~ 3 minutes, depending on the heart rate of the volunteer. Without cardiac triggering, 1 min 24 s would be achievable.

QISS: A TR of 800 ms per slice, a TE of 2.74 ms, and a bandwidth of 183 Hz/px was applied. Image slices were acquired sequentially with GRE readout using a partial Fourier factor of 5/8. After the saturation RF pulses, a subsequent time interval (QI, here, 350 ms) is applied to wait for non-saturated blood spins to enter the imaging region. The sequence was gated using the acoustic cardiac triggering device. A time delay of 100 ms followed the trigger event. As in UGRE, a single slice is completely acquired beginning with the trigger event. Total acquisition time for each station was on average ~ 2 minutes depending on the heart rate of the volunteer. Without cardiac triggering, 48 s would be achievable. The protocol was run with only the CP^+ mode applied to the 16-ch coil and only 1 average (instead of the 2 that were necessary for TIAMO in the other protocols).

An overview of the relevant sequence parameters of GRE, UGRE and QISS can be found in Table 4.1.

	GRE	**UGRE**	**QISS**
TR [ms]	14	700 per slice	800 per slice
TE [ms]	5.26	3.84	2.74
Bandwidth [Hz/px]	1300	930	183
Slice orientation	Transversal	Transversal	Transversal
Slices	60	60	60
Slice acquisition	Sequential / ascending	Sequential / ascending / single shot	Sequential / ascending / single shot
FOV [mm^2]	390 x 293	390 x 293	390 x 293
Voxel volume [mm^3]	1.0 x 1.0 x 2.0	1.0 x 1.0 x 2.0	1.0 x 1.0 x 2.0
Acquisition matrix	384 x 288	384 x 288	384 x 288
Parallel imaging with GRAPPA: acceleration factor / reference lines	4/32	4/32	4/32
Partial Fourier factor	-	-	5/8
Fat suppression	-	-	Yes
Venous saturation	Prior to every excitation	Prior to every 2nd excitation	Prior to single-shot slice acquisition

Cardiac triggering	-	Phonocardiogram	Phonocardiogram
TIAMO	Yes: CP^{+}/CP^{2+} (dedicated shims in the upper thigh if necessary)	Yes: CP^{+}/CP^{2+} (dedicated shims in the upper thigh if necessary)	No: CP^{+} (dedicated shim in the upper thigh if necessary)
Averages (TIAMO)	2	2	1
TA per station [min:s]	2:41	1:24 ≤ TA ≤ ~ 4:00 2:54 on average	0:48 ≤ TA ≤ ~ 3:30 2:09 on average

Table 4.1. Sequence parameters. *Overview of relevant protocol parameters for GRE, UGRE and QISS sequence. The total acquisition time TA of GRE and QISS depended on the individual's general heart rate and amounted to max about 4 min / 3 min 30 s; without cardiac triggering 1 min 24 s / 48 s would be necessary.*

To compare the three sequences, 10 volunteers (4 female and 6 male, average age: 26.7 years, range: 20 to 38 years; average weight: 70.7 kg, range: 53 to 90 kg; average height: 1.75 m, range: 1.65 to 1.87 m) were examined by acquiring all three sequences consecutively at the same station before moving the AngioSURF table to the next station beginning at the hip and proceeding toward the feet.

For quantitative comparison of the three sequences, ROIs were placed in a single artery and in the tissue directly next to that artery for each station in both legs individually. The same artery and tissue positions were chosen for every sequence. Using the two ROIs, a vessel-to-background ratio (VBR = $\text{Signal}_{\text{Vessel}} / \text{Signal}_{\text{Tissue}}$)[31] could be calculated, where values > 1 are desirable to distinguish vessels, especially when looking at MIPs. The higher the VBR, the better the visibility of the vessel. For each station, the VBR was determined at 3 positions within the imaged region: In the central slice as well as in the slices located 5 slices toward the borders of the imaged region to avoid effects caused by gradient nonlinearity or B_1 inhomogeneities which are expected to be especially apparent in the outermost slices. As in the QISS sequence TIAMO could not be used, to minimize the influence of B_1 inhomogeneity in the evalutation of the QISS sequence, arteries were chosen that were not impaired by B_1 inhomogeneities.

To check for statistical significant differences between the three sequences, a t-test was performed.[32]

4.3 Results

In seven volunteers 10 stations were acquired, in two volunteers 11 stations, and in one volunteer 12 stations. On average 124 ROIs were placed per volunteer and sequence. In total, 1242 ROIs per sequence were evaluated. Figure 4.2 presents maximum intensity projections (MIPs) of all acquired stations for one volunteer. For the UGRE sequence, the sparse application of the venous saturation pulses combined with the shorter spoiler gradient and saturation RF pulse permitted acquisition of one complete slice across two heartbeats. Owing to TIAMO, two averages needed to be acquired to utilize both excitation modes. Due to the consecutive acquisition of both modes, excitation and saturation pulses are always run in the same mode. Nevertheless, sufficient suppression of the venous system could be realized in the final image. The inherent saturation effects of the GRE readout in the UGRE permitted suppression of the static background tissue including fat, even though no fat suppression RF pulses were applied.

The individual heart rate dictates the total acquisition time for triggered sequences, but on average, UGRE imaging took 2 min 54 s per station while QISS took only 2 min 9 s. Without triggering 36 s would be the difference between the two sequences (although UGRE acquires two acquisitions), amounting to 45 s on average when using cardiac triggering. This means, QISS was prolonged by a factor of 2.7 on average while UGRE is prolonged by a factor of 2.1 compared to imaging without any triggering.

As observed in [17], the use of a general B_0 shim for all stations as determined at the uppermost station did not lead to perceivable image distortions.

For all volunteers, VBR was averaged over all stations and both legs using the standard deviation of the signal intensities inside the measured ROIs as error. For every volunteer UGRE performed better than GRE, while QISS achieved the lowest values in all volunteers (Table 4.2). In GRE and UGRE, fluctuation of VBR between different slices within a station as well as in between different stations is much higher than in QISS imaging. This is reflected in the overall higher errors for the calculated VBR in Table 4.2. Highest vessel signal could be observed in the

Figure 4.2. Complete MIPs of GRE, UGRE and QISS of one volunteer. *MIPs of all acquired stations merged together manually in one volunteer for GRE, UGRE, and QISS. In this volunteer, the two stations covering the upper part of the thighs (marked by white double-headed arrows) used individual RF shims to prevent complete artery signal dropout. Vessel signal fluctuation in GRE could be mostly avoided in UGRE and QISS due to cardiac triggering (grey arrows). Tissue signal intensity fluctuation in QISS is most probably due to time delay induced by heartbeat triggering giving the surrounding tissue time to relax. White arrow in QISS shows vein visible in QISS sequence, as only one of the TIAMO RF shim modes could be used, preventing complete venous suppression.*

Volunteer	GRE	UGRE	QISS
V1	4.53 ± 0.17	4.90 ± 0.19	2.47 ± 0.08
V2	4.22 ± 0.17	6.08 ± 0.23	3.29 ± 0.16
V3	4.85 ± 0.26	5.56 ± 0.30	2.24 ± 0.10
V4	3.69 ± 0.12	4.90 ± 0.16	3.11 ± 0.08
V5	3.08 ± 0.16	3.46 ± 0.13	1.85 ± 0.06
V6	4.47 ± 0.17	5.44 ± 0.21	2.96 ± 0.14
V7	4.17 ± 0.17	5.88 ± 0.21	3.23 ± 0.11
V8	3.46 ± 0.14	4.82 ± 0.19	3.51 ± 0.11
V9	5.42 ± 0.17	5.58 ± 0.19	2.29 ± 0.05
V10	3.85 ± 0.13	5.37 ± 0.17	2.26 ± 0.05
Average	**4.18 ± 0.05**	**5.20 ± 0.06**	**2.72 ± 0.03**

Table 4.2. Averaged VBR of all volunteers. *Averaged VBR over all stations and both legs for the ten volunteers. In the far right column, the average over all volunteers is given. Standard deviation of the signal intensities inside the measured ROIs were used as error. Error values in this table were calculated via rules for propagation of uncertainty. The QISS sequence led to the lowest VBR in all cases, whereas UGRE performed best. Overall, UGRE reached relevantly higher values than GRE.*

QISS sequence, but also the highest tissue signal, which taken together led to the lowest VBR. Between different stations no relevant deviation and no tendency within a station (e.g. high VBR in uppermost slice and then decrease in signal) could be observed, except that vessels were harder to identify in the lowest stations at the level of the feet. In four volunteers for all sequences, delineation of arteries was not possible in the complete lowermost station, and in three volunteers delineation was not possible in the lowermost slices. In QISS images identification of the arteries in the lowermost station was not possible in four volunteers (in one of them also not possible for GRE). Averaged over all volunteers (and stations), GRE reached a VBR of 4.18 ± 0.05, UGRE 5.20 ± 0.06, and QISS 2.72 ± 0.03 (Table 4.2).

To test for statistically significant differences between the three techniques, a t-test was performed. The resulting P values provided an estimation for the significance of differences, and P values less than 0.05 can be considered as statistically significant. The results of the t-test showed that the differences between all techniques are statistically significant. Paired comparisons led to $P = 0.02 / 0.03$ for GRE compared to UGRE / QISS and $P < 0.001$ for UGRE compared to QISS.

Flow artifacts were very severe in GRE images (Fig. 4.3, 4.4), while in UGRE and QISS only a slight broadening in the phase-encode direction could be observed in some slices (Fig. 4.3). In UGRE images weak aliasing artifacts could be observed (Fig. 4.4). Since no TIAMO could be used for QISS imaging, clearly visible B_1 inhomogeneities are present which are considerably less pronounced or not visible in GRE and UGRE (Fig. 3, 4). Additionally, vessel contours appeared slightly blurred in QISS imaging (Fig. 4.4). Also, veins are often visible whereas they are nearly completely suppressed in GRE and UGRE (Fig. 4.2). Due to the blurring and the lower VBR in QISS, vessels were more poorly delineated or weren’t even visible (Fig. 4.3, 4.4).

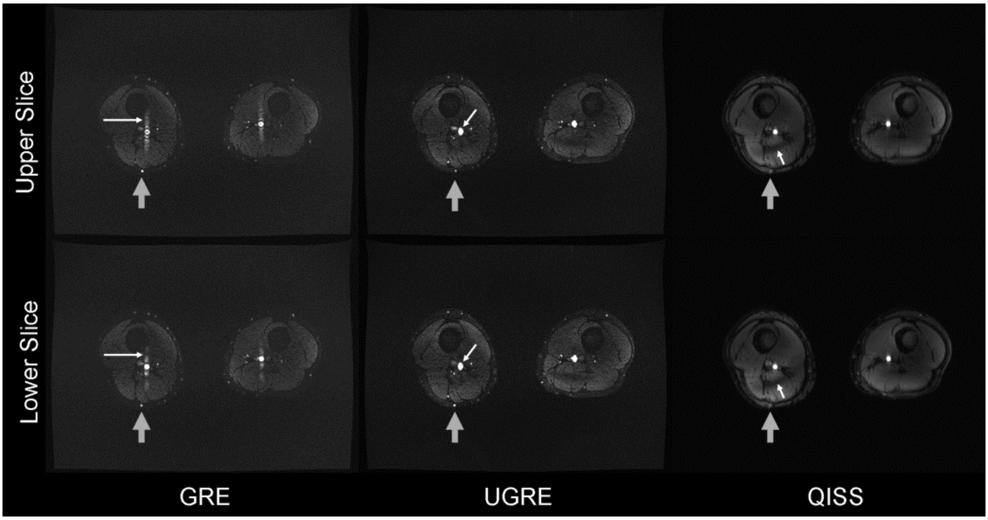

Figure 4.3. Signal variation flow artifact. *Signal variation flow artifact (white arrow in GRE) shown for consecutive axial slices at position of the grey arrow in Fig. 4.1 compared to the corresponding images in UGRE and QISS. In UGRE large arteries seem to be slightly broadened (white arrow). In the QISS images,* B_1 *inhomogeneities are considerably more pronounced as TIAMO could not be used (white arrows). For GRE and UGRE, especially the smaller vessels can be more easily delineated than for QISS (grey arrows). The upper row shows the slice position superior to the images of the lower row.*

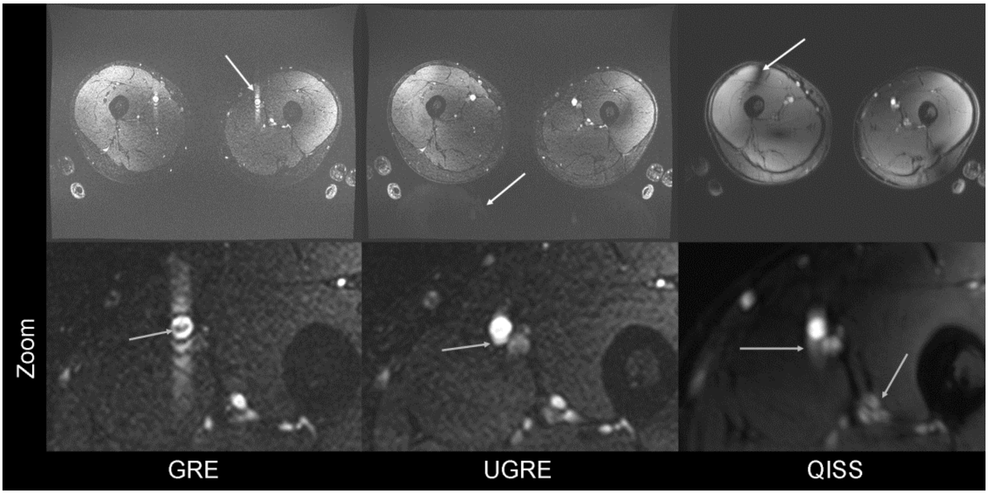

Figure 4.4. Artifacts in GRE, UGRE and QISS. *The upper row visualizes the flow artifact in GRE images, aliasing in UGRE, and* B_1 *inhomogeneity in QISS, in each case marked by a white arrow. Due to use of TIAMO, the* B_1 *inhomogeneity could be ameliorated in GRE and UGRE. Zoomed images of the left thigh in the lower row show GRE, where the flow artifact in the phase-encode direction and a small signal dropout inside the vessel lumen are clearly visible (grey arrow), UGRE and QISS. For UGRE, slight broadening of the arteries can be observed (grey arrow). In the QISS image, blurring of the vessel walls is clearly observed (grey arrows). Artery circumference can be delineated best in UGRE.*

In six volunteers (3 female, 3 male), dedicated TIAMO shims for the upper thighs were calculated based on individual B_1 maps to improve the visibility of the arteries (Fig. 4.5). After detection of the impaired vessel visibility, the scan was interrupted and restarted with the new shims after B_1 maps were acquired and the dedicated RF shims were calculated. The acquisition of the B_1 maps and the calculation took less than 2 minutes. The remaining stations were examined with the CP^+ and CP^{2+} modes. The use of TIAMO imaging in conjunction with dedicated shims in the upper thighs of certain volunteers led to nearly homogenous images over all stations.

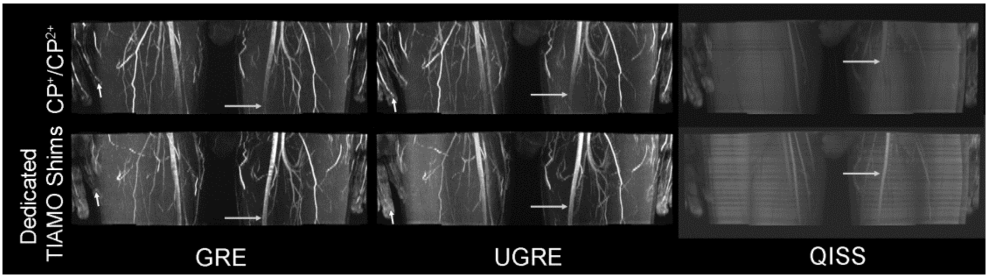

Figure 4.5. Dedicated TIAMO shims. *MIPs showing the first station of the thigh. The upper row shows images acquired using TIAMO with the* CP^+ *and* CP^{2+} *modes. In the case of QISS, only* CP^+ *was used. In the lower row, dedicated TIAMO shims were calculated after the acquisition of* B_1 *maps. In the case of QISS, only one of the two modes could be used. One can clearly see that the left superficial femoral artery can be delineated throughout the entire station with the dedicated* B_1 *shims (grey arrows), whereas the finger arteries lost signal (short white arrow in GRE and UGRE).*

4.4 Discussion

The use of cardiac triggering in conjunction with both the UGRE and QISS sequences suppressed intravascular signal variations[17] at the cost of measurement time. The triggering itself (due to time intervals between two triggers) and variations in current heart rate prolong the measurement time depending on the individual's general heart rate. If the succeeding trigger event occurs too early and k-space data sets are not acquired completely, a time delay until the next trigger event must be introduced. The acquisition time per station ranged from approximately 1 min 30 s to 3 min. In the QISS sequence, the gating and the thereby induced time delay is reflected in signal variations of the background tissue (cf. Fig. 4.2). A very fast heart rate could also potentially lead to a relevant amount of interrupted data acquisition due to the gating. This would require triggering on only every 2nd heartbeat, prolonging the measurement time even more. Especially for fast heart rates, the possibility to use the saturation pulses sparsely as well as the shorter spoiler gradient and the shorter saturation RF pulse were essential. For the given UGRE protocol, the fastest possible heart rate is 85 bpm, limited by the inverse of the TR of 700 ms. The TR also determines the acquirable image resolution and correspondingly holds for the QISS sequence which is reflected in the factor the total acquisition time per station was prolonged (2.1 for a TR of 700 ms in the UGRE and 2.7 for a TR of 800 ms in the QISS). To speed up the UGRE sequence further, a lower resolution or a more sparsely applied saturation sequence segment would be possible. However, the latter would sooner or later lead to more pronounced vein visibility. Further investigation of the relationship between heart rate and the necessary minimum number of applied saturation pulses could be pursued, but a relevant benefit is not expected. The pragmatic way to acquire data from volunteers with higher heart rates would be to trigger only every 2nd heartbeat, concomitantly enabling a resolution increase at the cost of a longer acquisition time. A general increase of the image resolution would require sparser triggering, depending on the heart rate.

The use of a general B_0 shim that was determined at the uppermost station was robust enough to be used for all following stations without perceivable image distortions, thus helping to moderate total acquisition time as the B_0 shim procedure did not need to be repeated.

The comparison of the measured VBR shows that the UGRE sequence performed best, as it showed only moderate artifacts and led overall to the highest VBR of all sequences. It provided the best artery visibility of all sequences, as the GRE was impaired by flow artifacts combined with signal dropouts due to the lack of triggering. In one of the 10 volunteers GRE performed equally to UGRE in terms of VBR (V9 in Table 4.2), but UGRE was still preferable as GRE was strongly impaired by flow artifacts. The QISS protocol showed a comparatively smaller number of vessels with blurred contour. UGRE performed statistically significant better than GRE and QISS, while VBR for UGRE and GRE were quite comparable and clearly higher than for QISS. The fact that the vessel signals acquired with QISS were the highest of all sequences shows the potential of this sequence. Unfortunately, the preparation RF pulses do not seem to work as effective as for lower field strength in suppressing the background tissue. As the QISS protocol is a vendor-provided work-in-progress at 7 T, the actual VBR can only be treated as preliminary result and could improve with further optimizations at this field strength; in particular, implementation of the TIAMO technique would be expected to significantly reduce B_1 artifacts.

In the lowermost station at the level of the feet, depiction of the arterial vessels was not possible in all slices (in seven cases for all sequences). Here, a higher imaging resolution, at the cost of prolonged total acquisition time, might help to identify more vessels. Apart from the narrow vessel diameters near the feet, a technical reason for this problem could be a relevant difference in loading of the RF coil with the feet compared to the region of the pelvis.

The absence of heartbeat triggering in the GRE sequence led to the same flow artifacts as reported in [17], which are most probably induced by an interference between individual heart rate and image acquisition frequency. GRE images are acquired covering the whole cardiac cycle and therefore a strong variation in flow velocity is present which leads to differences in flow compensation efficiency. This issue can be avoided mostly in UGRE and QISS via cardiac triggering. The weak aliasing artifacts that were visible in the UGRE sequence did not disturb the image quality, especially when looking at MIPs. The reason for the aliasing artifact is that the saturation RF pulse is applied only every second TR which leads to two different effective TRs. This leads to a periodic signal variation: Every second line in k-space is acquired with slightly lower signal which results in an artifact in axial slices which appears similar to aliasing. A possibility to prevent that would be to excite with two different flip angles and / or using a different k-space ordering. But as the artifact is only slightly visible in the axial images and not visible in the MIPs, this was not implemented yet and might be topic of future study. The slight vessel broadening visible in the phase-encode direction in UGRE was not visible in the coronal MIPs. The reason for the latter artifact is most probably that, despite cardiac triggering, the blood flow velocities are not constant during acquisition of the whole slice and thus the pronounced flow artifact observed in GRE remains in small parts visible in UGRE. In general, as two consecutively excited modes contribute to one individual slice the UGRE sequence is more prone to volunteer movements than GRE. On the other side, the consecutive acquisition ensures application of excitation and saturation pulses in the same mode, simplifying sparse application of the saturation pulses and leading to sufficient venous suppression in the final image. In the QISS images blurring of the vessels was observed which led to poorer vessel delineation, and especially smaller vessels could not be delineated at all. Regarding artifacts, UGRE would be the most preferable sequence.

Six of the examined volunteers required calculation of individual TIAMO RF shim settings for the station at the level of the thighs to improve the visibility of the superficial femoral artery in both legs; this extra step required the acquisition of B_1 maps. Another possible solution for this issue may be the use of high-permittivity pads to increase the transmit field homogeneity.[33] The remaining stations could be examined with the CP^+ and CP^{2+} modes, indicating that the combination of the CP^+ and CP^{2+} mode is relatively robust for TIAMO imaging. The most probable reason for the need of individual RF shimming is the variable anatomy at the transition from pelvis to the legs along the longitudinal axis. Also, this might depend on the leg circumference and / or the ratio between fat and muscle.

In conclusion, the UGRE sequence variant performed best for non-enhanced MRA of the lower extremity vessels, as the observed artifacts were only moderate and the highest average VBR was reached with a statistically significant difference to the compared sequences. The QISS sequence performed worst regarding VBR, while GRE showed the most severe flow artifacts despite reaching satisfactory VBR values. This study also revealed that the calculation of individual RF shim settings in a large proportion of volunteers as well as cardiac triggering, both of which prolong measurement time, are essential for the continuous depiction of the lower extremity arteries with non-enhanced MRA at 7 T.

Acknowledgments

We would like to thank the Ultra-High Field team of Siemens, especially Thomas Benner, for their technical support and Michael Schwarz of the Department of General Psychology: Cognition, University of Duisburg-Essen, Duisburg, Germany, for the support on the statistical analysis.

References

1. Gutzeit A, Sutter R, Froehlich JM, Roos JE, Sautter T, Schoch E, Giger B, Wyss M, Graf N, von Weymarn C, Jenelten R, Binkert CA, Hergan K. ECG-triggered non-contrast-enhanced MR angiography (TRANCE) versus digital subtraction angiography (DSA) in patients with peripheral arterial occlusive disease of the lower extremities. Eur Radiol 2011;21:1979-1987.

2. Thomsen HS. Nephrogenic systemic fibrosis: A serious late adverse reaction to gadodiamide. Eur Radiol 2006;16:2619-2621.

3. Prince MR, Zhang HL, Roditi GH, Leiner T, Kucharczyk W. Risk factors for NSF: a literature review. J Magn Reson Imaging 2009;30:1298-1308.

4. Lanzman RS, Blondin D, Schmitt P, Orzechowski D, Godehardt E, Scherer A, Modder U, Kropil P. Non-Enhanced 3D MR Angiography of the Lower Extremity using ECG-Gated TSE Imaging with Non-Selective Refocusing Pulses - Initial Experience. Rofo 2010;182:861-867.

5. Hodnett PA, Koktzoglou I, Davarpanah AH, Scanlon TG, Collins JD, Sheehan JJ, Dunkle EE, Gupta N, Carr JC, Edelman RR. Evaluation of Peripheral Arterial Disease with Nonenhanced Quiescent-Interval Single-Shot MR Angiography. Radiology 2011;260:282-293.

6. Fan ZY, Sheehan J, Bi XM, Liu X, Carr J, Li DB. 3D Noncontrast MR Angiography of the Distal Lower Extremities Using Flow-Sensitive Dephasing (FSD)-Prepared Balanced SSFP. Magn Reson Med 2009;62:1523-1532.

7. Nakamura K, Miyazaki M, Kuroki K, Yamamoto A, Hiramine A, Admiraal-Behloul F. Noncontrast-enhanced Peripheral MRA: Technical Optimization of Flow-Spoiled Fresh Blood Imaging for Screening Peripheral Arterial Diseases. Magn Reson Med 2011;65:595-602.

8. Cukur T, Lee JH, Bangerter NK, Hargreaves BA, Nishimura DG. Non-contrast-Enhanced Flow-Independent Peripheral MR Angiography with Balanced SSFP. Magn Reson Med 2009;61:1533-1539.

9. Maderwald S, Ladd SC, Gizewski ER, Kraff O, Theysohn JM, Wicklow K, Moenninghoff C, Wanke I, Ladd ME, Quick HH. To TOF or not to TOF: strategies for non-contrast-enhanced intracranial MRA at 7 T. Magma 2008;21:159-167.

10. Nowinski WL, Puspitasaari F, Volkau I, Marchenko Y, Knopp MV. Comparison of Magnetic Resonance Angiography Scans on 1.5, 3, and 7 Tesla Units: A Quantitative Study of 3-Dimensional Cerebrovasculature. J Neuroimaging 2013;23:86-95.

11. Hoult DI, Phil D. Sensitivity and power deposition in a high-field imaging experiment. J Magn Reson Imaging 2000;12:46-67.

12. Van De Moortele PF, Akgun C, Adriany G, Moeller S, Ritter J, Collins CM, Smith MB, Vaughan JT, Ugurbil K. B-1 destructive interferences and spatial phase patterns at 7 T with a head transceiver array coil. Magn Reson Med 2005;54:1503-1518.

13. Vaughan TT, Snyder CJ, DelaBarre LJ, Bolan PJ, Tian J, Bolinger L, Adriany G, Andersen P, Strupp J, Ugurbil K. Whole-Body Imaging at 7T: Preliminary Results. Magn Reson Med 2009;61:244-248.

14. Umutlu L, Maderwald S, Kinner S, Kraff O, Bitz AK, Orzada S, Johst S, Wrede K, Forsting M, Ladd ME, Lauenstein TC, Quick HH. First-pass contrast-enhanced renal MRA at 7 Tesla: initial results. Eur Radiol 2013;23:1059-1066.

15. Orzada S, Maderwald S, Poser BA, Bitz AK, Quick HH, Ladd ME. RF excitation using time interleaved acquisition of modes (TIAMO) to address B1 inhomogeneity in high-field MRI. Magn Reson Med 2010;64:327-333.

16. Orzada S, Maderwald S, Poser BA, Johst S, Kannengiesser S, Ladd ME, Bitz AK. Time-interleaved acquisition of modes: an analysis of SAR and image contrast implications. Magn Reson Med 2012;67:1033-1041.

17. Fischer A, Maderwald S, Orzada S, Johst S, Schafer LC, Ladd ME, Nassenstein K, Umutlu L, Lauenstein TC. Nonenhanced magnetic resonance angiography of the lower extremity vessels at 7 tesla: initial experience. Investigative radiology 2013;48:525-534.

18. Frauenrath T, Hezel F, Renz W, d'Orth TD, Dieringer M, von Knobelsdorff-Brenkenhoff F, Prothmann M, Schulz-Menger J, Niendorf T. Acoustic cardiac triggering: a practical solution for synchronization and gating of cardiovascular magnetic resonance at 7 Tesla. J Cardiovasc Magn R 2010;12:67.

19. Maderwald S, Orzada S, Lin Z, Schäfer L, Bitz A, Kraff O, Brote I, Häring L, Czylwik A, Zenge M, Ladd SC, Ladd M, Nassenstein K. 7 Tesla Cardiac Imaging with a Phonocardiogram Trigger Device. In: Proceedings of the 19th Annual Meeting of ISMRM, Montreal, Canada, 2011. (abstract 1322).

20. Nassenstein K, Orzada S, Haering L, Czylwik A, Zenge M, Eberle H, Schlosser T, Bruder O, Muller E, Ladd ME, Maderwald S. Cardiac MRI: evaluation of phonocardiogram-gated cine imaging for the assessment of global und regional left ventricular function in clinical routine. Eur Radiol 2012;22:559-568.

21. Nassenstein K, Orzada S, Haering L, Czylwik A, Jensen C, Schlosser T, Bruder O, Ladd ME, Maderwald S. Cardiac magnetic resonance: is phonocardiogram gating reliable in velocity-encoded phase contrast imaging? Eur Radiol 2012;22:2679-2687.

22. Edelman RR, Sheehan JJ, Dunkle E, Schindler N, Carr J, Koktzoglou I. Quiescent-interval single-shot unenhanced magnetic resonance angiography of peripheral vascular disease: Technical considerations and clinical feasibility. Magn Reson Med 2010;63:951-958.

23. Orzada S, Maderwald S, Kraff O, Brote I, Ladd ME, Solbach K, Yazdanbakhsh P, Bahr A, H.P. F, Bitz AK. 16-Channel Tx/Rx Body Coil for RF Shimming with Selected Cp Modes at 7T. In: Proceedings of the 18th Annual Meeting of ISMRM, Stockholm, Sweden, 2010. (abstract 50).

24. Bitz AK, Brote I, Orzada S, Kraff O, Maderwald S, Quick HH, Yazdanbakhsh P, Solbach K, Bahr A, Bolz T, Wicklow K, Schmitt F, Ladd ME. An 8-channel add-on RF shimming system for whole-body 7 tesla MRI including real-time SAR monitoring. Paper presented at: ISMRM 17th Annual Meeting Honolulu, Hawai, USA, 2009. (abstract 4767).

25. Yazdanbakhsh P, Fester M, Oppelt R, Bitz AK, Kraff O, Orzada S, Ladd ME, Solbach K. Variable Power Combiner for a 7T Butler Matrix Coil Array. mIn: Proceedings of the 17th Annual Meeting of ISMRM, Honolulu, Hawaii, 2009. (abstract 397).

26. Herborn CU, Goyen M, Quick HH, Bosk S, Massing S, Kroeger K, Stoesser D, Ruehm SG, Debatin JF. Whole-body 3D MR angiography of patients with peripheral arterial occlusive disease. AJR Am J Roentgenol 2004;182:1427-1434.

27. Quick HH, Vogt FM, Maderwald S, Herborn CU, Bosk S, Gohde S, Debatin JF, Ladd ME. High spatial resolution whole-body MR angiography featuring parallel imaging: initial experience. Rofo 2004;176:163-169.

28. Ackerman MJ, Spitzer VM, Scherzinger AL, Whitlock DG. The Visible Human data set: an image resource for anatomical visualization. Medinfo 1995;8 Pt 2:1195-1198.

29. Christ A, Kainz W, Hahn EG, Honegger K, Zefferer M, Neufeld E, Rascher W, Janka R, Bautz W, Chen J, Kiefer B, Schmitt P, Hollenbach HP, Shen J, Oberle M, Szczerba D, Kam A, Guag JW, Kuster N. The Virtual Family--development of surface-based anatomical models of two adults and two children for dosimetric simulations. Phys Med Biol 2010;55:N23-38.

30. Snyder CJ, DelaBarre L, Metzger GJ, van de Moortele PF, Akgun C, Ugurbil K, Vaughan JT. Initial Results of Cardiac Imaging at 7 Tesla. Magn Reson Med 2009;61:517-524.

31. Johst S, Wrede KH, Ladd ME, Maderwald S. Time-of-flight magnetic resonance angiography at 7 T using venous saturation pulses with reduced flip angles. Invest Radiol 2012;47:445-450.

32. Rasch D, Guiard V. The robustness of parametric statistical methods. Psychology Science 2004;46:175-208.

33. Teeuwisse WM, Brink WM, Webb AG. Quantitative assessment of the effects of high-permittivity pads in 7 Tesla MRI of the brain. Magn Reson Med 2012;67:1285-1293.

Chapter 5 Investigation of the Saturation Pulse Artifact in Non-Enhanced MR Angiography of the Lower Extremity Arteries at 7 Tesla*

Abstract

When performing non-enhanced time-of-flight MR angiography of the lower extremity arteries at 7 T with cardiac triggering, the acquisition time is a crucial consideration. Therefore, in previous studies, saturation RF pulses were applied only every second TR. In the axial source images a slight artifact with an appearance similar to aliasing could be observed. The purpose of this study was to investigate the origin of this artifact. The reason for the artifact is supposed to be related to the two effective TRs during acquisition caused by the sparsely applied saturation RF pulse. Several sequence variants were simulated and implemented within the sequence source code to examine this hypothesis. An adaptation of the excitation flip angles for each TR as well as a correction factor for the k-space data was calculated. Additionally, a different ordering of the k-space data during acquisition was implemented as well as the combination of the latter with the k-space correction factor. The observations from the simulations were verified using both a static and a flow phantom and finally, in a healthy volunteer using the same measurement setup as in previous volunteer and patient studies. Of all implemented techniques, only the reordering of the k-space was capable of suppressing the artifact almost completely at the cost of creating a ringing artifact. The phantom measurements showed the same results as the simulations and could thus confirm the hypothesis regarding the origin of the artifact. This was additionally verified in the healthy volunteer. The origin of the artifact could be confirmed to be the periodic signal variation caused by two effective TRs during acquisition.

*__Johst S__, Maderwald S, Fischer A, Quick HH, Ladd ME, Orzada S.
"Investigation of the Saturation Pulse Artifact in Non-Enhanced MR Angiography of the Lower Extremity Arteries at 7 Tesla"
PLOS ONE (in press)

5.1 Introduction

In recent studies, non-contrast-enhanced (ne) MR angiography (MRA) sequences have been evaluated as an alternative to digital subtraction angiography (DSA) and contrast-enhanced MRA for the diagnosis of lower extremity vascular diseases.[1-6] Using ne-MRA techniques has the clear advantage of being non-invasive and avoiding application of potentially harmful ionizing radiation. Furthermore, cases of Nephrogenic Systemic Fibrosis (NSF) have been reported after the administration of gadolinium(Gd)-based contrast agents.[7,8] Initial work at an increased magnetic field strength of 7 T indicates further potential for the usage of non-contrast-enhanced time-of-flight (TOF) MRA sequences, as the visibility of the vasculature increases,[9,10] and the feasibility of ne-MRA of the lower extremity arteries at 7 T was recently demonstrated in healthy volunteers and patients.[11-13]

In a recently published work, a modified turbo-FLASH (TFL) sequence was utilized for non-contrast-enhanced imaging of the lower extremity arteries[12] (Fig. 5.1a). To reduce known B_1 inhomogeneities at 7 T,[14] Time-Interleaved Acquisition of Modes (TIAMO)[15,16] was integrated into the sequence. The principle of TIAMO is to excite at least two different B_1 transmission modes using static radiofrequency (RF) shimming in an interleaved acquisition. In so doing, overall signal homogeneity can be improved by exploiting the complementary radiofrequency patterns of the different transmission modes. Data from e.g. two acquisitions are not just averaged, but reconstructed the same way as if twice the number of receive coils would have been used, additionally allowing higher acceleration factors to be used to reduce the scan time increase arising from multiple acquisitions. Finally, considerably more homogeneous images can be obtained. To avoid periodic variation in the signal intensity of the arteries that was observed in [11], acoustic cardiac triggering via a phonocardiogram was additionally used to synchronize the sequence with the heartbeat.[17-19]

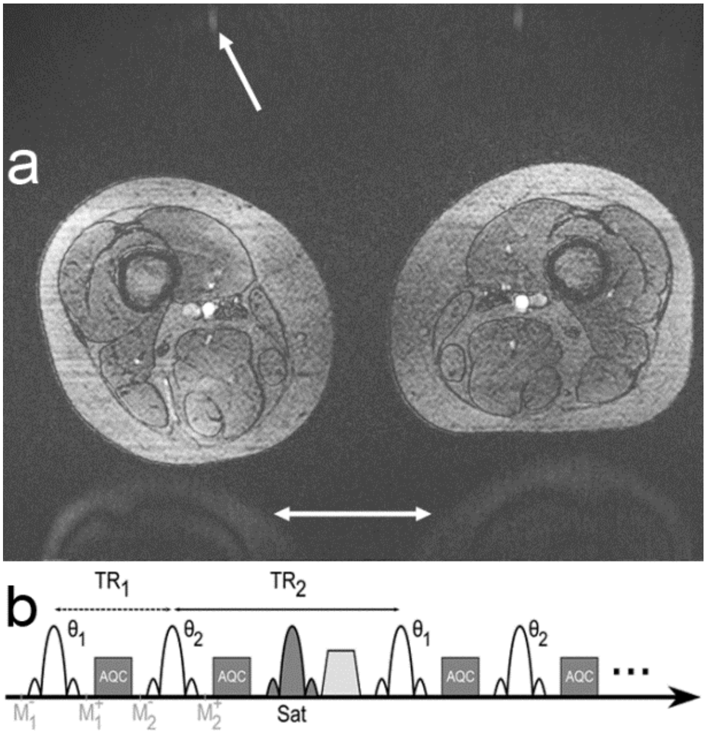

Figure 5.1. Artifact and sequence diagram. *Axial source image of MRA of the lower extremities at the level of the upper thighs (a). Imaging with two effective TRs leads to an artifact that appears similar to aliasing (arrows). A diagram of the TFL sequence implementation shows the variation in effective TR due to the saturation pulse block preceding every second excitation (b).*

As mainly the heart rate defines the total acquisition time, one complete slice (one TR) should preferably be acquired between two heartbeats to maintain a reasonable acquisition time. TRs shorter than the time interval between two heartbeats lead to significantly shorter total measurement times. Thus, the shorter the TR, the higher the heart rate that can be acquired without measurement time prolongation. One way to decrease TR is to apply RF pulses for the suppression of signal from the venous system only sparsely.[20,21] Volunteer measurements preceding the examinations in [11-13] showed that RF pulses for venous suppression need to be applied at least every second TR (Fig. 5.1b) to suppress the veins sufficiently using the chosen acquisition parameters.

Measurement times with this method for the acquisition of one station with 60 slices amounted on average to 2 min 54, depending on the heart rate of the volunteer / patient (1 min 24 s without triggering).[12] The application of the saturation RF pulse together with its spoiling gradient every other TR leads to two different effective TRs. This led to an unexpected artifact in axial slices that appears similar to aliasing (Fig. 5.1a). In the example shown, artifact intensity was approximately 50% up to 67% of the background tissue signal and approximately 20% of the arterial signal.

This publication examines the origin and nature of the observed aliasing-like artifact. The artifact is hypothesized to be caused by the periodic signal variation induced by the two alternating different effective TRs: every second line is acquired with slightly weaker signal, which leads to an attenuated aliasing artifact – similar to the aliasing which would appear if these lines would not be acquired at all. Therefore, different sequence variants were simulated to examine their impact on the artifact. In the next step the variants were implemented within the sequence source code and compared in measurements with a static setup, a flow phantom, and finally in-vivo. Understanding the nature of the artifact is important for future modifications and further developments of the used sequence variant.

5.2 Materials and Methods

Ethics Statement

The study was conducted in conformance with the Declaration of Helsinki and approved by the Ethics Commission of the Medical Faculty of the University Duisburg-Essen (study number 11-4898-BO). Written informed consent was obtained from each volunteer before the examination.

The use of different TRs during acquisition can be found e.g. in balanced steady-state free precession (SSFP) sequences[22,23] or in the actual flip angle imaging (AFI) method.[24,25] Just as in the modified TFL sequence presented here, in the original version of the AFI sequence[24] two alternating TRs generate two different signals that are used to calculate a flip angle map. Compared to the AFI sequence, the present TFL sequence acquires only half the lines, as in AFI every line is collected twice and two complete images are reconstructed from the two signals individually. This means that the signal formulas given in the publication by Yarnykh[24] can be used to simulate the observed artifact.

Simulations

To simulate the artifact, a flip-angle map inside a circular phantom including a linear gradient from 1° to 90° within and 0° outside (Fig. 5.2a) was defined in Matlab (R2010a, Mathworks, Natick, USA). This map was used to calculate two images based on the alternating signals produced by excitation with two alternating TRs:[24]

$$S_1 = M_0 \cdot \frac{1+e^{-\frac{T_{R,2}}{T_1}} \cdot \left(\left(1-e^{-\frac{T_{R,1}}{T_1}}\right) \cdot \cos\theta - 1 \right)}{1-\cos^2\theta \cdot e^{-\frac{T_{R,1}+T_{R,2}}{T_1}}} \cdot e^{-\frac{T_E}{T_2^*}} \cdot \sin\theta \qquad [5.1]$$

and

$$S_2 = M_0 \cdot \frac{1+e^{-\frac{T_{R,1}}{T_1}} \cdot \left(\left(1-e^{-\frac{T_{R,2}}{T_1}}\right) \cdot \cos\theta - 1\right)}{1-\cos^2\theta \cdot e^{-\frac{T_{R,1}+T_{R,2}}{T_1}}} \cdot e^{-\frac{T_E}{T_2^*}} \cdot \sin\theta \qquad [5.2]$$

Both images were Fourier transformed (FT) and a new k-space was formed by taking every even line from one image and every odd line from the other. The resulting retransformed image shows the characteristic artifact that was observed in the measurements (cf. Fig. 5.1a, 5.2b).

To confirm that the artifact arises from the difference in TR, four sequence variants were simulated in the following that included: 1) adaptation of the flip angle for every other excitation, 2) application of a correction factor within the k-space data before reconstruction, 3) reordering of the k-space data, and 4) a combination of reordering and correction factor. All simulations were performed with the following parameters corresponding to the values of the later performed static phantom measurements: TR_1 = 4 ms, TR_2 = 7 ms; T_1 = 1420 ms; T^*_2 = 450 ms; TE = 3 ms.

1) Flip angle adaptation

In [26], the application of two different flip angles to avoid the artifact was examined. Similar to the formula given in [24], a general formula for imaging with two TRs, $TR_{1/2}$, and flip angles, $\theta_{1/2}$, can be derived (s. Appendix):

$$S_1 = M_0 \cdot \frac{1+e^{-\frac{T_{R,2}}{T_1}} \cdot \left(\left(1-e^{-\frac{T_{R,1}}{T_1}}\right) \cdot \cos\theta_2 - 1\right)}{1-\cos\theta_1 \cdot \cos\theta_2 \cdot e^{-\frac{T_{R,1}+T_{R,2}}{T_1}}} \cdot e^{-\frac{T_E}{T_2^*}} \cdot \sin\theta_1 \qquad [5.3]$$

and accordingly:

$$S_2 = M_0 \cdot \frac{1+e^{-\frac{T_{R,1}}{T_1}} \cdot \left(\left(1-e^{-\frac{T_{R,2}}{T_1}}\right) \cdot \cos\theta_1 - 1\right)}{1-\cos\theta_1 \cdot \cos\theta_2 \cdot e^{-\frac{T_{R,1}+T_{R,2}}{T_1}}} \cdot e^{-\frac{T_E}{T_2^*}} \cdot \sin\theta_2 \qquad [5.4]$$

The condition $S_1 = S_2$ has to be met to preclude the artifact and can be solved numerically. By keeping θ_2 fixed and varying θ_1 from 1° to 90°, a flip angle $\theta_1(\theta_2)$ that minimizes the signal difference can be determined. With the hereby determined flip angle $\theta_1(\theta_2)$, the simulation was repeated by calculating two images by inserting the flip angle map in equation [5.3] and [5.4], then combining the FT representations line-by-line before retransformation. This technique was only used for the simulations, not for the phantom measurements.

2) k-space correction

Another way to influence the artifact is to apply a correction factor to the raw data in k-space. In order to avoid prolongation of total measurement time, only the center line of k-space can be acquired twice with both TRs to estimate the correction factor for all lines with lower signal. With a view to the later phantom measurements and in contrast to the flip angle adaptation, acquiring a correction factor would not depend on an a-priori estimation of the signal difference between TRs, which depends among others on T_1 and the actually achieved flip angle distribution. To calculate the k-space correction factor, the mean ratio of the k-space center lines of the image with weak / strong signal (Eq. [5.1] and [5.2]) was determined. Then, every k-space line that was generated by the weaker signal image was multiplied by the inverse of this ratio. From this data a new image was reconstructed. k-space correction was used both in the simulations and static phantom measurements.

3) Reordering

A completely different approach to reducing the impact of the artifact is to change the order in which the lines in k-space are acquired. Image contrast is determined by the data in the center of k-space. Applying a low-pass filter by shifting the lines generated by the weaker signal to the higher k-space frequencies while keeping the lines with stronger signal in the center, the image signal should increase and the artifact should be suppressed. Therefore, the magnitude-reduced lines were distributed equally to the uppermost / lowermost ends of the

FT of the target before retransformation. Reordering was used in all later simulations and measurements.

4) Reordering and k-space correction factor

For additional image correction, the same reordering described in the above case is combined with the k-space correction factor by multiplying the lines originating from the weaker signal with the factor determined in case 2. The combination of reordering and k-space correction was used in the simulations and static phantom experiments.

Sequence modifications

After simulation of the sequence variants described above, the methods were integrated into the sequence source code. In addition to the modifications described in [12], the following changes were made to the TFL sequence to examine the aliasing artifact:

1) For the estimation of the correction factor to be applied to the lines acquired with lower signal, the center line of k-space is acquired twice using both effective TRs. For reconstruction, only the acquisition with higher signal is used.

2) The k-space ordering of this sequence usually moves from the highest to the lowest k-space phase encoding step (or vice versa), which means that the center is acquired in the middle of the acquisition. For the reordering described in case 3, the lines with weaker signal are distributed to the higher areas in k-space. As an example for a resolution of 64, the RF pulse with the weaker signal is assigned to phase encoding steps -32 to -17 and +16 to +31, whereas the excitation with higher signal is assigned to -16 to +15 (including zero). The acquisition order would then be -32, **-16**, -31, **-15**,…**-1**, -17, **0**, 16, **1**…, **15**, 31 (RF with higher signal in bold font), which means that the center of k-space is still acquired in the middle of the overall acquisition. As long as the total number of acquired lines is a multiple of 4, this reordering scheme is valid for this sequence, although the number of GRAPPA reference lines must be carefully considered if parallel acquisition is used.

Measurement Configuration

Static phantom measurements

Examinations were performed on a 7 T whole-body system (Magnetom 7T, Siemens, Erlangen, Germany) with a 32-channel transmit/receive head coil (Nova Medical, Wilmington, MA). A spherical vendor-provided polydimethylsiloxane oil phantom with T_1 = 1420 ms was used. One slice was acquired in the isocenter with effective TR_1 = 4 ms and TR_2 = 7 ms using a TE = 3.07 ms, a bandwidth of 488 Hz/pixel, an acquisition matrix of 320 x 320, a field of view (FOV) = 300 mm x 300 mm, and a nominal flip angle of 80°. Saturation sequence block was applied every second k-line to evoke two different TRs, but the saturation RF pulse itself was applied with a voltage of 0 V to assure that the artifact is only generated by the difference in effective TR. The measurements were performed without using TIAMO or GRAPPA.

Dynamic phantom measurements

Additional measurements were performed using the same 32-channel head coil and a custom-built cylindrical phantom containing a tissue-simulating liquid (37.5% water, 56.5% sugar, 6% salt, $\varepsilon r = 46.3$, $\sigma = 0.8/V/m$)[15] water-sugar solution and two tubes, one empty and one filled with the same liquid with 1:1000 Gadovist contrast agent (Bayer Schering Pharma AG, Berlin, Germany). A flexible tube of approximately 0.6 mm diameter was placed directly next to the outside surface of the phantom. The water running at constant flow velocity of approximately 0.2 m/s through the tube was driven by a custom-built water pump: an immersion pump (“outside pump EXTRA”, COMET-Pumpen KG, Kriftel, Germany) combined with a power regulator (M171 PMW power control, Kemo Electronic, Langen, Germany) to change the constant flow velocity, both driven by a standard 12 V direct current power source of a desktop PC. The water pump was operated outside of the RF room passing the tubes through waveguides into the bore of the MR system. Imaging parameters corresponded to [12,13] and were identical to the in-vivo measurements given below. TIAMO and GRAPPA were applied for these measurements to be as close as possible to the in-vivo protocol.

With the 32-channel head coil, just one transmission mode can be excited; hence, applying TIAMO just leads to averaging of both acquisitions.

Volunteer measurements

Examinations were performed with a 16-channel transmit/receive coil based on [27]. The same configuration as in [12,13] was used. Five stripline meander elements were placed dorsally on the patient table and eleven meander elements were placed on a rigid, semicircular former above the table. A RF shimming system with 8 channels similar to [28] was used to drive the coil with an 8-channel variable power combiner (VPC) interfaced to a 16-channel Butler matrix.[29] Eight of the 16 inputs of the 16-channel Butler matrix corresponding to the highest transmit signal in the corresponding transmit modes were connected to the VPC.[27] In this way the 8-channel transmit system could be used to drive the 16-channel coil. Image acquisition was performed with an AngioSURF table[30,31] of 2 m length by positioning the volunteer feet-first supine. The AngioSURF table can be moved manually to the desired body position through the RF coil, which remained stationary at the isocenter connected to the original patient table. For compliance with the International Electrotechnical Commission (IEC) guidelines, SAR calculations (CST Microwave Studio, Darmstadt, Germany) were performed in human adult male and female body models of the Virtual Family and the Visible Human.[32,33] Full-wave simulations were applied with exact dimensions and characteristics of the 16-channel RF coil, and maximum permitted input power levels for each station were calculated from the simulations of the corresponding body models. Based on these simulations, a standardized SAR file was integrated into the SAR monitoring system.[28]

Almost the same volunteer imaging protocol as in [12,13] was used: a nominal flip angle of 80° and a FOV of 375 mm by 281 mm to acquire 60 transversal slices with 2 mm thickness using a matrix of 384 by 288 pixels and thus an in-plane resolution of approximately 1 mm^2. Parallel image acceleration with a GRAPPA factor of 4 utilizing 32 integrated auto-calibration lines was used. A TR of 705 ms per slice, a

TE of 3.81 ms, and a bandwidth of 1090 Hz/pixel were chosen. Image slices were acquired sequentially and in ascending order using flow compensation. No inversion RF pulses for contrast preparation were used. RF pulses for venous saturation were applied every second TR. TIAMO imaging[15,16] used the CP^+ and CP^{2+} modes. The sequence was gated by using an acoustic cardiac triggering device in such a way that one complete slice was acquired after each trigger signal. Due to TIAMO, each slice has to be acquired twice to combine both modes. The two modes are acquired consecutively. After a single trigger signal, one complete slice is acquired with the first mode and the same slice excited with the second mode follows after the next trigger event. Measurements were conducted in accordance with all guidelines set forth by the approving institutional review board. Written informed consent was obtained before the examination.

Using the spherical phantom, the results from the simulations were verified with normal ordering, with the k-space correction factor, with reordering, and with reordering combined with the k-space correction factor. To approach the contrast expected in MRA with defined and reproducible conditions, normal ordering and reordering were compared using the flow phantom with constant flow velocity. Finally, to verify that the behavior would not change when measuring in-vivo, e.g. due to pulsatile flow, normal ordering and reordering were examined in a healthy volunteer.

5.3 Results

In Figure 5.2, the simulation results are shown including the flip angle map (Fig. 5.2a) and the artifact that results when two different TRs are applied (Fig. 5.2b). A comparison of the effect of the different variants on the image can be found in Fig. 5.2c to 5.2e, while 5.2f shows the calculated flip angle for a direct adaptation of the excited signal. In Fig. 5.2g, the artifact signal intensity is given relative to the corresponding signal inside the phantom. For the different techniques, Fig. 5.2h shows the signal inside the phantom relative to the image with artifact (5.2b). The phantom signal of the artifact image is also plotted relative to the two images that were calculated by using only the stronger (Eq. [5.1]) and weaker (Eq. [5.2]) signal respectively.

Comparison with Fig. 5.2g (blue line) shows that the artifact signal increases – relative to the signal inside the phantom – with higher flip angles because the signal difference is greater at higher flip angles. The observed artifact signal corresponds to signal from within the phantom and appears at a location shifted in the phase-encoding direction. The calculations revealed that the artifact intensity depends mainly on the ratio TR_1 / TR_2 and the flip angle, but only minimally on T_1 as long as TR << T_1 (results not shown). The higher the flip angle, the greater the signal difference (Eq. [5.1] and [5.2]) and the greater the artifact signal. Looking at the signal inside the phantom, one can see in Fig. 5.2h that the increase in the artifact signal is reflected in the signal decrease within the phantom of the image with artifact relative to an image with strong signal only (Fig. 5.2h, dotted blue line). Simultaneously, the signal within the phantom of the image with artifact gets higher with higher flip angles relative to the image with weaker signal only (Fig. 5.2h, dashed blue line).

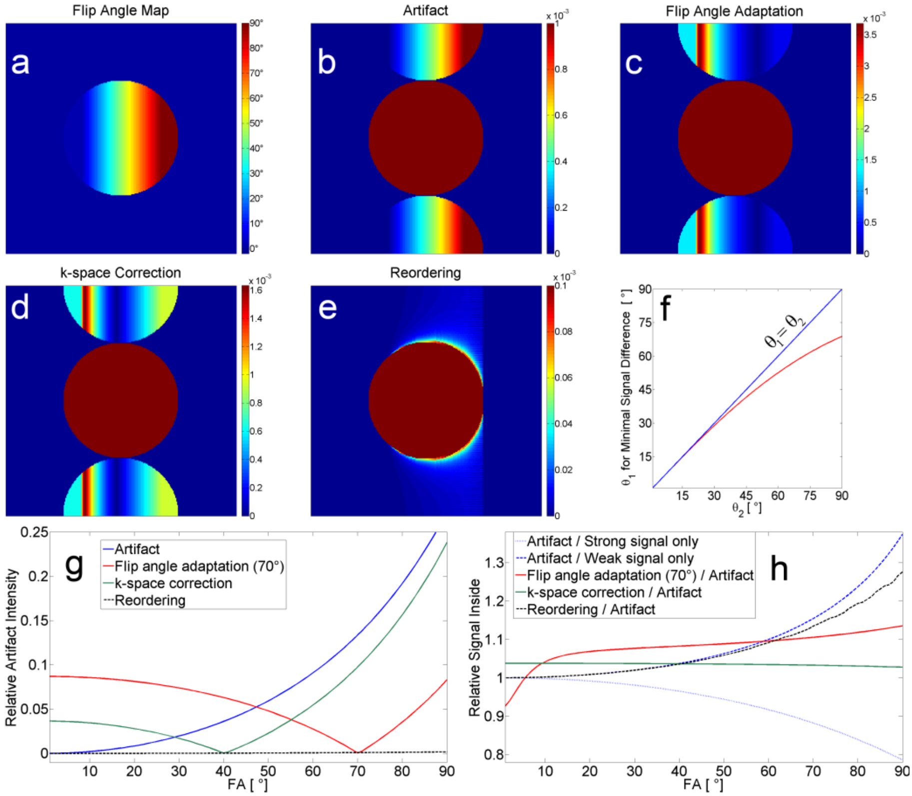

Figure 5.2. Simulation results. *Simulations were performed with flip angle map (a) to illustrate the artifact (b). (c)-(e) show different sequence variants: flip angle adaptation (c) with the flip angle calculated for minimal signal difference (red line in f), correction factor applied in k-space (d), and low-pass filter-like reordering of k-space (e). The combination of reordering and k-space correction factor was nearly identical to the reordering alone and is thus not shown here. (g) shows artifact signal intensity relative to corresponding signal inside the phantom. (h) shows signal intensity within the phantom relative to the image with artifact (red, green, and dotted black lines) as well as the intensity of the artifact image relative to an image created with strong / weak signal only (dotted and dashed blue lines). Scaling of the images (b-e) was oriented on the corresponding maximum artifact signal. Hence, the signal inside the phantom is cut off and appears homogeneous.*

Using equations [5.3] and [5.4], a flip angle θ_1 was calculated that depends on θ_2 (Fig. 5.2f). Only for small flip angles (here, approximately < 25°) is the signal difference small enough that the same flip angles can be chosen for both excitations. An excitation flip angle adaptation did not lead to an artifact-free image for the simulated non-homogenous flip angle distribution (Fig. 5.2a) as only for a single flip angle can the artifact be nulled (here exemplarily shown for 70° in Fig. 5.2c, 5.2g: red line). Although the artifact level could be reduced to less than 10% over the flip angle range below the adapted flip angle of 70°, there is an interval (< 47°) where the artifact level is even higher than in the uncorrected image. With this technique, the overall artifact level would be reduced if the flip angle range contained in the image is not as broad as in this calculation, i.e. 48° to 90° instead of 1° to 90° when optimizing for 70°. This range would be sufficient when looking at e.g. 7-T head imaging. Over a wide flip angle range, the signal within the phantom is approximately 10% higher relative to the image with artifact with a slight increase towards higher flip angles; however, below 5° there is a relative signal decrease of less than 10% (Fig. 5.2h, red line).

Similar to the flip angle adaptation, the k-space correction factor technique is able to reduce the artifact signal relative to the signal inside the phantom, but below a certain flip angle that shows maximal reduction, the artifact level again increases and even higher relative values are reached below about 29° (Fig. 5.2g, green line). The general course of the relative artifact signal is nearly the same as for the flip angle adaptation technique. The signal inside the phantom increases over the entire flip angle range: 4% for small flip angles with a slight decrease to approximately 3% for higher flip angles (Fig. 5.2h, green line).

Reordering of the k-space lines during acquisition prevents the aliasing artifact (Fig. 5.2e) almost completely (slight increase to max 0.2% at 90°), and the signal inside the phantom is increased (Fig. 5.2h, dashed black line). The signal of the reordered image approximates the signal increase that is observed comparing artifact image and image with strong signal only (Fig. 5.2h, dashed black line and dotted blue line). Direct comparison of the image formed by reordering and the image formed by the stronger signal only showed that the highest difference, observed at 90°, is still less than 5%. This means that reordering almost mimics the signal of an image with strong signal only. However, by reordering the k-space, a ringing artifact appears with increased amplitude towards higher flip angles (Fig. 5.3, black line). For 15°, the ringing amplitude is less than 0.1%, for 45° less than 0.6%, and for 90° less than 3%. For higher flip angles, ringing can also be observed outside the phantom (Fig. 5.3f).

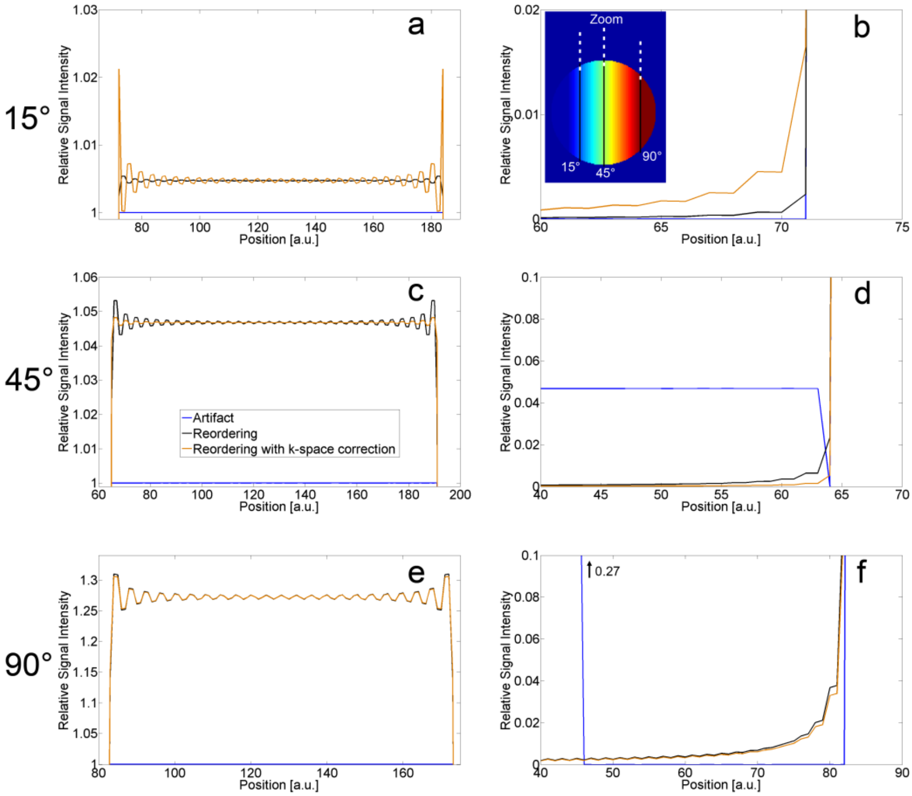

Figure 5.3. Ringing artifact. *Ringing artifact generated by the reordering of k-space (black line) compared to the uncorrected artifact image (blue line) and with additional k-space correction factor applied (orange line). On the left (a, c, e) profiles through the images of Fig. 5.2b, e show the relative signal increase compared to the original artifact image within the phantom. On the right (b, d, f) the upper border of the phantom was zoomed in to show artifact signal outside. Note that the scaling of the axes is different.*

If the k-space correction factor is applied to the weaker k-space lines after reordering, approximately identical relative artifact signal / signal within the phantom are reached as for the reordering technique alone; hence, these results not plotted in Fig. 5.2. The correction factor is able to reduce the amplitude of the ringing for medium flip angles (45°: Fig. 5.3c, d). For higher flip angles only a slight reduction is achieved (Fig. 5.3e, f), but for flip angles below 45°, the ringing amplitude is even increased by the k-space correction (15°: Fig. 5.3a, b).

For the phantom measurements, the flip angle adaptation was not further pursued, only the k-space correction factor was used to determine its impact on combining it with k-space reordering. A nominal flip angle of 80° was chosen to get high artifact signals, as the simulations showed that the artifact intensity increases with flip angle. As at 7 T the excitation profile is known to be inhomogeneous, a nominal flip angle of 80° was chosen to prevent flip angles higher than 90° that are normally not used for excitation with sequences based on gradient echo.

In Figure 5.4, the results from the phantom measurements are shown. The images were not corrected for the receive sensitivity profile of the coil. In the upper row, the images with artifact (Fig. 5.4a) and with k-space correction factor (Fig. 5.4b) are shown. As in the simulations, the correction factor can only suppress the artifact partially (Fig. 5.4b). The reordering of k-space suppresses the entire artifact (Fig. 5.4c), while after combination with the k-space correction factor no relevant improvements were observable (Fig. 5.4d). Figure 5.4e shows a flip angle estimation obtained by reconstructing both signals individually and calculating a flip angle map as described for the AFI method[24] from the two generated images. Both individual images show strong aliasing as only half the lines could be used for reconstruction. In the profiles through the middle of the phantom, the curves for reordering and reordering combined with k-space correction are almost identical (Fig. 5.4f, black and orange lines), but applying the correction factor increases the noise in the image by a factor up to approximately 2. The mean artifact signal (relative to the signal inside the phantom) was approximately 28% for the artifact image and 6% after reordering. In the profile on the right side of the phantom (Fig. 5.4g), one can clearly see that the k-space correction factor can also lead to an amplification of the artifact (Fig. 5.4g, green line). Both the correction factor and reordering were able to increase the signal within the phantom.

In the upper row of Figure 5.5, results from the measurements with the flow phantom are shown. Water was flowing with constant velocity only within the tubes outside the phantom. Using GRAPPA, the aliasing artifact was less pronounced (Fig. 5.5a). Applying reordering, the aliasing transforms into ringing within and outside the phantom, just as in the simulations (Fig. 5.3).

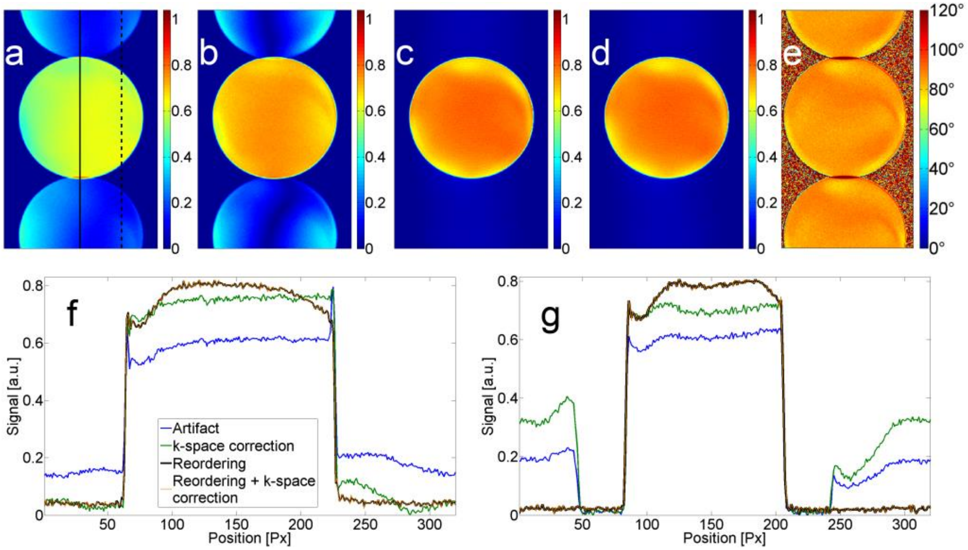

Figure 5.4. Static phantom measurements. *Results of phantom measurements showing uncorrected artifact image (a), image with k-space correction (b), image with reordered acquisition (c), and image with reordering and k-space correction factor combined (d). (e) shows an estimation of flip angle obtained by reconstructing both signals individually and calculating a flip angle map as described for the AFI method[24]. In the lower row, profiles through the middle of the phantom (f) and on the right side of the phantom (g) are shown. Positions of the profiles are exemplarily shown in (a). Reordering and reordering combined with k-space correction are almost congruent (black and orange lines in f, g).*

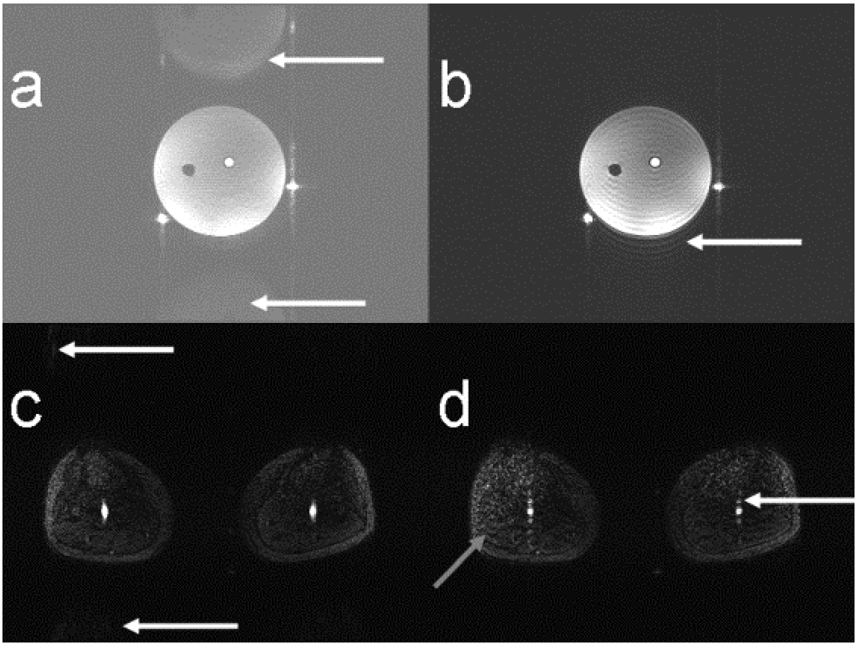

Figure 5.5. Flow phantom and volunteer measurements. *Upper row: measurement results in the flow phantom. Only the tubes outside the phantom contained flowing water at constant velocity. The white arrows in (a) point to the aliasing artifact while in (b) the ringing artifact (arrow) is visible that originates from the reordering scheme. In the lower row, in-vivo images are shown with the aliasing artifact almost not visible (c), arrows). Using a reordered acquisition led to slight ringing artifacts ((d), oblique grey arrow) and to multiple depiction of the arteries (white arrow). Image (c) and (d) are windowed identically.*

The tubes inside seem not to be affected by the reordered acquisition. In the volunteer measurement (Fig. 5.5c), aliasing was less pronounced than in the aforementioned images, but still visible if windowing was chosen accordingly. No aliasing was observable in the reordered case, while ringing was slightly visible within the legs (oblique grey arrow in Fig. 5.5d) and slightly visible outside. The arteries, however, are depicted multiple times in the phase-encode direction while being only slightly dilated using standard ordering as reported in [12].

5.4 Discussion

Of the compared simulated sequence variants, reordering of k-space during data acquisition was the only technique able to reduce the artifact intensity significantly over the entire flip angle range and to restore the signal within the phantom. Both flip angle adaptation and k-space correction nearly nulled the artifact signal only for a certain narrow range of flip angles. Although over this flip angle range the artifact signal is reduced, there are flip angles for which the artifact signal is even increased. For the flip angle adaptation, equal signals would also be achievable by increasing the flip angle θ_2 instead of decreasing θ_1 as investigated here. However, this approach would imply increasing SAR.

For the k-space correction, the flip angle which showed minimal artifact signal was approximately the mean flip angle over the entire phantom. The flip angle adaptation searches for flip angles for which both signals are equal. In contrast, the k-space correction factor tries to increase the level of the weaker signal to the level of the stronger signal (Eq. [5.2] and [5.1]). For a perfectly homogeneous excitation, both techniques would decrease the artifact signal to zero, but the signal inside the phantom would be higher with the k-space correction, since it would reach the signal of an image with strong signal only. Comparing FT representation of images with stronger and weaker signal for an inhomogeneous phantom (results not shown), one can see that the correction factor is not constant for every line as for a homogeneous phantom, but oscillates from line to line and also within every line. In fact, the artifact is distributed in both directions of k-space, and a correction factor defined only line-by-line would only correct in one direction. Only a point-wise correction could lead to reasonable results, which would require acquiring the image twice. When using a GRE sequence which reaches a steady state after a certain number of acquisitions, the correction factor would deviate additionally for the lines which are acquired before reaching the steady state.

The signal of the reordered image approximates the signal of the image with strong signal only. This behaves as expected because the inner k-space is filled by the stronger signal acquisitions due to the reordering. The oscillation that can be seen in Fig. 5.2h (dashed black line) is due to the ringing artifact that can be observed at the borders and throughout the entire phantom for higher flip angles (Fig. 5.3). Suppressing the aliasing artifact by reordering the k-space in this way leads to a ringing artifact which is caused by the abrupt change in signal intensity at a certain threshold in k-space due to the lines with weaker signal. Inverting the reordering by placing the weaker signals in the center of the phantom led to the same ringing artifact besides reducing the signal within the phantom (results not shown). The aliasing artifact observed here and in [11,12] is weaker than the known case of acquiring only every second line. Similarly, the ringing artifact caused by reordering is also weaker than it would be if caused by Gibbs ringing where only the inner k-space is acquired and zero-filling is used for the outer parts of k-space [34,35]. For the simulations performed here, if the higher frequencies are filled with zeroes instead of with the weaker signal, Gibbs ringing is visible for all flip angles and oscillations of maximally 7% of the mean signal within the phantom; with reordering of the weaker signals instead, only < 0.5% for 15° and 3% for 90° are reached.

Combining reordering with the k-space correction factor led to almost identical results regarding relative artifact signal and signal intensity within the phantom (hence not shown in Fig. 5.2). The same was observed for the ringing artifact for higher flip angles (Fig. 5.3e, f), while for lower flip angles the amplitudes of the ringing were even increased (Fig. 5.3a, b). Only for medium flip angles (e.g. 45°, Fig. 5.3c, d) was ringing clearly reduced. The reason is that 45° is quite near to the flip angle of approximately 40° in Fig. 5.2g that shows least artifact signal for the k-space correction factor. As is observed for the aliasing artifact with k-space correction factor in an inhomogeneous excitation, combining reordering with a k-space correction factor is not useful as the ringing artifact is reduced only in some parts of the flip angle range while it is increased in other parts. Another way to correct k-space for the ringing would be to apply some kind of filtering, e.g. a Tukey-window which can be used to reduce Gibbs ringing.[34]

Although ringing is observed with reordering, reordering does not depend on the choice of one particular flip angle for which the artifact disappears, which is in strong contrast to the k-space correction factor or flip angle adaptation.

The phantom measurements of k-space correction, reordering, and reordering combined with k-space correction provided the same results that were achieved in the simulations. k-space correction seems to provide a flatter profile within the phantom, but this is most probably due to signal energy that is projected outside of the phantom, generating the aliasing artifact (Fig. 5.4f, green line).

As the sequence that was applied in [12,13] uses two TRs, it actually acquires half the lines that are acquired when applying an actual flip-angle imaging (AFI) sequence.[24] The signal difference that produces the artifact can also be used to estimate the flip angle if the lines with stronger signal and the lines with weaker signal are reconstructed individually. With the formula given in [24], a flip angle map can be calculated using these two images (Fig. 5.4e). The result shows strong aliasing because the two individual images are reconstructed from two sets of data undersampled by a factor of two.

Although the aliasing artifact is weaker in-vivo than in the phantom measurements (Fig. 5.5a, c), the ringing predicted by the simulation could still be observed (Fig. 5.5d). The arteries, however, showed an artifact that cannot be explained by mere ringing as it was not visible with constant flow (Fig. 5.5b). Due to the multiple ghosting of the arteries in the images with reordering (Fig. 5.5d), this variant should not be used for suppressing the aliasing artifact. As this artifact was not observed when measuring with constant flow (Fig. 5.5b), the reason for the artifact must lie with the pulsatile flow in vivo. With the reordering technique, the inner lines of k-space are not acquired consecutively but interleaved with lines from the outside, extending the acquisition of the inner k-space over a longer period of time. This makes the acquisition with reordering more prone to changes in blood flow velocity.

Blood flows quite fast at the beginning of the cardiac cycle and then reduces its velocity to be quite constant before the next heart beats accelerates it again. This effect is visible as the slight vessel dilation in the image with aliasing artifact (Fig. 5.5c). Also, a very similar artifact was observed in some images for the FLASH sequence in [11]. In that work, image acquisition with the FLASH sequence was performed without cardiac triggering, which means that depending on the exact time the center of k-space is acquired either relatively constant blood flow or a relatively strong change in blood flow velocity is experienced, the latter leading to the slight vessel dilation.

The methods discussed in this work are not suited for sufficient suppression of the aliasing artifact. One possibility to suppress the artifact would be to apply a partial Fourier factor and use the thereby gained measurement time reduction to apply the saturation RF pulse in every line. However, due to the fact that coronal MIPs are used when looking at the images,[13] the aliasing artifact in the phase-encode direction is not disturbing. With the current system hardware, only 8 kW of RF amplifier peak power are available, of which only approximately half is available at the coil. With higher amplifier power, a more sparse application of the saturation pulses would presumably still lead to sufficient venous suppression due to the higher achieved flip angles and thus would be beneficial in reducing the artifact.

In conclusion, the simulation and phantom measurements confirmed that the origin of the observed aliasing artifact lies – as hypothesized – in the periodic signal variation due to the two effective TRs experienced by the spins during acquisition.

5.5 Appendix

Formula for flip angle correction

In the steady-state, for $0° \leq \theta_1, \theta_2 \leq 90°$ the magnetization has to satisfy the following relations (Fig. 5.1b):

(1) $M_2^+ = M_2^- \cdot \cos\theta_2$

(2) $M_2^- = M_1^+ \cdot e^{-\frac{T_{R,1}}{T_1}} + M_0\left(1 - e^{-\frac{T_{R,1}}{T_1}}\right)$

(3) $M_1^+ = M_1^- \cdot \cos\theta_1$

(4) $M_1^- = M_2^+ \cdot e^{-\frac{T_{R,2}}{T_1}} + M_0\left(1 - e^{-\frac{T_{R,2}}{T_1}}\right)$

Inserting (2) into (1) gives:

$$M_2^+ = M_1^+ \cdot e^{-\frac{T_{R,1}}{T_1}} \cdot \cos\theta_2 + M_0\left(1 - e^{-\frac{T_{R,1}}{T_1}}\right) \cdot \cos\theta_2$$

Inserting this into (4) gives:

$$M_1^- = M_1^+ \cdot e^{-\frac{T_{R,1}}{T_1}} \cdot e^{-\frac{T_{R,2}}{T_1}} \cdot \cos\theta_2 + M_0\left(1 - e^{-\frac{T_{R,1}}{T_1}}\right) \cdot e^{-\frac{T_{R,2}}{T_1}} \cdot \cos\theta_2 + M_0\left(1 - e^{-\frac{T_{R,2}}{T_1}}\right)$$

Inserting (3) into this result gives:

$$M_1^- = M_1^- \cdot e^{-\frac{T_{R,1}}{T_1}} \cdot e^{-\frac{T_{R,2}}{T_1}} \cdot \cos\theta_1 \cdot \cos\theta_2 + M_0\left(1 - e^{-\frac{T_{R,1}}{T_1}}\right) \cdot e^{-\frac{T_{R,2}}{T_1}} \cdot \cos\theta_2 + M_0\left(1 - e^{-\frac{T_{R,2}}{T_1}}\right)$$

Finally, solving the equation for M_1^- yields:

$$M_1^- = M_0 \cdot \frac{1 + e^{-\frac{T_{R,2}}{T_1}} \cdot \left(\left(1 - e^{-\frac{T_{R,1}}{T_1}} \right) \cdot \cos\theta_2 - 1 \right)}{1 - \cos\theta_1 \cdot \cos\theta_2 \cdot e^{-\frac{T_{R,1}+T_{R,2}}{T_1}}}$$

and accordingly:

$$M_2^- = M_0 \cdot \frac{1 + e^{-\frac{T_{R,1}}{T_1}} \cdot \left(\left(1 - e^{-\frac{T_{R,2}}{T_1}} \right) \cdot \cos\theta_1 - 1 \right)}{1 - \cos\theta_1 \cdot \cos\theta_2 \cdot e^{-\frac{T_{R,1}+T_{R,2}}{T_1}}}$$

To ensure correct image acquisition without artifact, the signals from both excitations with different T_R have to be the same. Since the tissue parameters are the same in both cases, the flip angles have to satisfy:

$$M_2^- \cdot \sin\theta_2 = M_1^- \cdot \sin\theta_1$$

$$\left(1 + e^{-\frac{T_{R,1}}{T_1}} \cdot \left(\left(1 - e^{-\frac{T_{R,2}}{T_1}} \right) \cdot \cos\theta_1 - 1 \right) \right) \cdot \sin\theta_2 =$$
$$\left(1 + e^{-\frac{T_{R,2}}{T_1}} \cdot \left(\left(1 - e^{-\frac{T_{R,1}}{T_1}} \right) \cdot \cos\theta_2 - 1 \right) \right) \cdot \sin\theta_1$$

This can be solved numerically. Assuming realistic values of $T_{R,1}, T_{R,2} \ll T_1$ and $T_{R,2} \leq T_{R,1} \leq 3T_{R,2}$, θ_2 can be approximated for a given θ_1 (in radians) and $m = \frac{T_{R,2}}{T_1}$ by using this equation:

$$\theta_2 = 0.7979 \cdot \theta_1 \cdot e^{0.4651m + 0.1771\theta_1} - 0.3225m \cdot {\theta_1}^2 - 0.2282m^2 \cdot \theta_1$$

References

1. Gutzeit A, Sutter R, Froehlich JM, Roos JE, Sautter T, Schoch E, Giger B, Wyss M, Graf N, von Weymarn C, Jenelten R, Binkert CA, Hergan K. ECG-triggered non-contrast-enhanced MR angiography (TRANCE) versus digital subtraction angiography (DSA) in patients with peripheral arterial occlusive disease of the lower extremities. Eur Radiol 2011;21:1979-1987.

2. Lanzman RS, Blondin D, Schmitt P, Orzechowski D, Godehardt E, Scherer A, Modder U, Kropil P. Non-Enhanced 3D MR Angiography of the Lower Extremity using ECG-Gated TSE Imaging with Non-Selective Refocusing Pulses - Initial Experience. Rofo 2010;182:861-867.

3. Hodnett PA, Koktzoglou I, Davarpanah AH, Scanlon TG, Collins JD, Sheehan JJ, Dunkle EE, Gupta N, Carr JC, Edelman RR. Evaluation of Peripheral Arterial Disease with Nonenhanced Quiescent-Interval Single-Shot MR Angiography. Radiology 2011;260:282-293.

4. Fan ZY, Sheehan J, Bi XM, Liu X, Carr J, Li DB. 3D Noncontrast MR Angiography of the Distal Lower Extremities Using Flow-Sensitive Dephasing (FSD)-Prepared Balanced SSFP. Magn Reson Med 2009;62:1523-1532.

5. Nakamura K, Miyazaki M, Kuroki K, Yamamoto A, Hiramine A, Admiraal-Behloul F. Noncontrast-enhanced Peripheral MRA: Technical Optimization of Flow-Spoiled Fresh Blood Imaging for Screening Peripheral Arterial Diseases. Magn Reson Med 2011;65:595-602.

6. Cukur T, Lee JH, Bangerter NK, Hargreaves BA, Nishimura DG. Non-contrast-Enhanced Flow-Independent Peripheral MR Angiography with Balanced SSFP. Magn Reson Med 2009;61:1533-1539.

7. Thomsen HS. Nephrogenic systemic fibrosis: A serious late adverse reaction to gadodiamide. Eur Radiol 2006;16:2619-2621.

8. Prince MR, Zhang HL, Roditi GH, Leiner T, Kucharczyk W. Risk factors for NSF: a literature review. J Magn Reson Imaging 2009;30:1298-1308.

9. Maderwald S, Ladd SC, Gizewski ER, Kraff O, Theysohn JM, Wicklow K, Moenninghoff C, Wanke I, Ladd ME, Quick HH. To TOF or not to TOF: strategies for non-contrast-enhanced intracranial MRA at 7 T. Magma 2008;21:159-167.

10. Nowinski WL, Puspitasaari F, Volkau I, Marchenko Y, Knopp MV. Comparison of Magnetic Resonance Angiography Scans on 1.5, 3, and 7 Tesla Units: A Quantitative Study of 3-Dimensional Cerebrovasculature. J Neuroimaging 2013;23:86-95.

11. Fischer A, Maderwald S, Orzada S, Johst S, Schafer LC, Ladd ME, Nassenstein K, Umutlu L, Lauenstein TC. Nonenhanced magnetic resonance angiography of the lower extremity vessels at 7 tesla: initial experience. Investigative radiology 2013;48:525-534.

12. Johst S, Orzada S, Fischer A, Schafer LC, Nassenstein K, Umutlu L, Lauenstein TC, Ladd ME, Maderwald S. Sequence comparison for non-enhanced MRA of the lower extremity arteries at 7 Tesla. PLoS One 2014;9:e86274.

13. Fischer A, Maderwald S, Johst S, Orzada S, Ladd ME, Umutlu L, Lauenstein TC, Kniemeyer HW, Nassenstein K. Initial evaluation of non-contrast-enhanced magnetic resonance angiography in patients with peripheral arterial occlusive disease at 7 T. Investigative radiology 2014;49:331-338.

14. Van De Moortele PF, Akgun C, Adriany G, Moeller S, Ritter J, Collins CM, Smith MB, Vaughan JT, Ugurbil K. B-1 destructive interferences and spatial phase patterns at 7 T with a head transceiver array coil. Magn Reson Med 2005;54:1503-1518.

15. Orzada S, Maderwald S, Poser BA, Bitz AK, Quick HH, Ladd ME. RF excitation using time interleaved acquisition of modes (TIAMO) to address B1 inhomogeneity in high-field MRI. Magn Reson Med 2010;64:327-333.

16. Orzada S, Maderwald S, Poser BA, Johst S, Kannengiesser S, Ladd ME, Bitz AK. Time-interleaved acquisition of modes: an analysis of SAR and image contrast implications. Magn Reson Med 2012;67:1033-1041.

17. Maderwald S, Orzada S, Lin Z, Schäfer L, Bitz A, Kraff O, Brote I, Häring L, Czylwik A, Zenge M, Ladd SC, Ladd M, Nassenstein K. 7 Tesla Cardiac Imaging with a Phonocardiogram Trigger Device. In: Proceedings of the 19th Annual Meeting of ISMRM, Montreal, Canada, 2011. (abstract 1322).

18. Nassenstein K, Orzada S, Haering L, Czylwik A, Zenge M, Eberle H, Schlosser T, Bruder O, Muller E, Ladd ME, Maderwald S. Cardiac MRI: evaluation of phonocardiogram-gated cine imaging for the assessment of global und regional left ventricular function in clinical routine. Eur Radiol 2012;22:559-568.

19. Nassenstein K, Orzada S, Haering L, Czylwik A, Jensen C, Schlosser T, Bruder O, Ladd ME, Maderwald S. Cardiac magnetic resonance: is phonocardiogram gating reliable in velocity-encoded phase contrast imaging? Eur Radiol 2012;22:2679-2687.

20. Schmitter S, Bock M, Johst S, Auerbach EJ, Ugurbil K, Van de Moortele PF. Contrast enhancement in TOF cerebral angiography at 7 T using saturation and MT pulses under SAR constraints: impact of VERSE and sparse pulses. Magn Reson Med 2012;68:188-197.

21. Zwanenburg JJM, Hendrikse J, Takahara T, Visser F, Luijten PR. MR Angiography of the Cerebral Perforating Arteries With Magnetization Prepared Anatomical Reference at 7T: Comparison With Time-of-Flight. Journal of Magnetic Resonance Imaging 2008;28:1519-1526.

22. Leupold J, Hennig J, Scheffler K. Alternating repetition time balanced steady state free precession. Magn Reson Med 2006;55:557-565.

23. Nayak KS, Lee HL, Hargreaves BA, Hu BS. Wideband SSFP: Alternating repetition time balanced steady state free precession with increased band spacing. Magn Reson Med 2007;58:931-938.

24. Yarnykh VL. Actual flip-angle imaging in the pulsed steady state: a method for rapid three-dimensional mapping of the transmitted radiofrequency field. Magn Reson Med 2007;57:192-200.

25. Voigt T, Nehrke K, Doessel O, Katscher U. T-1 Corrected B-1 Mapping Using Multi-TR Gradient Echo Sequences. Magn Reson Med 2010;64:725-733.

26. Johst S, Orzada S, Ladd ME, Maderwald S. Non-Enhanced MR Angiography of the Lower Extremity Arteries at 7T: Correction of Saturation Pulse Artifacts. Paper presented at: ISMRM 22nd Annual Meeting Milan, Milan, Italy, 2014. (abstract 2191).

27. Orzada S, Maderwald S, Kraff O, Brote I, Ladd ME, Solbach K, Yazdanbakhsh P, Bahr A, H.P. F, Bitz AK. 16-Channel Tx/Rx Body Coil for RF Shimming with Selected Cp Modes at 7T. In: Proceedings of the 18th Annual Meeting of ISMRM, Stockholm, Sweden, 2010. (abstract 50).

28. Bitz AK, Brote I, Orzada S, Kraff O, Maderwald S, Quick HH, Yazdanbakhsh P, Solbach K, Bahr A, Bolz T, Wicklow K, Schmitt F, Ladd ME. An 8-channel add-on RF shimming system for whole-body 7 tesla MRI including real-time SAR monitoring. Paper presented at: ISMRM 17th Annual Meeting Honolulu, Hawai, USA, 2009. (abstract 4767).

29. Yazdanbakhsh P, Fester M, Oppelt R, Bitz AK, Kraff O, Orzada S, Ladd ME, Solbach K. Variable Power Combiner for a 7T Butler Matrix Coil Array. In: Proceedings of the 17th Annual Meeting of ISMRM, Honolulu, Hawaii, 2009. (abstract 397).

30. Herborn CU, Goyen M, Quick HH, Bosk S, Massing S, Kroeger K, Stoesser D, Ruehm SG, Debatin JF. Whole-body 3D MR angiography of patients with peripheral arterial occlusive disease. AJR Am J Roentgenol 2004;182:1427-1434.

31. Quick HH, Vogt FM, Maderwald S, Herborn CU, Bosk S, Gohde S, Debatin JF, Ladd ME. High spatial resolution whole-body MR angiography featuring parallel imaging: initial experience. Rofo 2004;176:163-169.

32. Ackerman MJ, Spitzer VM, Scherzinger AL, Whitlock DG. The Visible Human data set: an image resource for anatomical visualization. Medinfo 1995;8 Pt 2:1195-1198.

33. Christ A, Kainz W, Hahn EG, Honegger K, Zefferer M, Neufeld E, Rascher W, Janka R, Bautz W, Chen J, Kiefer B, Schmitt P, Hollenbach HP, Shen J, Oberle M, Szczerba D, Kam A, Guag JW, Kuster N. The Virtual Family--development of surface-based anatomical models of two adults and two children for dosimetric simulations. Phys Med Biol 2010;55:N23-38.

34. Bernstein MA, King KF, Zhou ZJ. Handbook of MRI pulse sequences. Amsterdam ; Boston: Academic Press: 2004. 1017 p.

35. Oppenheim AV, Schafer RW. Discrete-time signal processing. Englewood Cliffs,N.J.: Prentice-Hall: 1989. 879 p.

Chapter 6 Summary

In this thesis, new sequence variants are presented that are suited for the challenging conditions at 7 T. The individual chapters are oriented towards providing feasible methods for clinical 7 T imaging.

In chapter 2, a TOF MRA sequence is presented that reduces the SAR of the sequence by applying the VERSE algorithm to excitation and saturation RF pulses. However, TR needs to be prolonged due to the SAR restrictions. Taking advantage of the inherent saturation effects of short TRs, the flip angle of the saturation RF pulse is additionally reduced to determine the lowest flip angle that still provides sufficient and robust saturation. Thereby even shorter saturation RF pulses can be applied and finally short total measurement times are accessible, mainly dependent on the chosen protocol parameters and not on SAR restrictions. Hence, high-resolution protocols with venous saturation in acceptable acquisition time are made available for clinical studies. Further measurement time reductions would only be available by examining sparsely applied RF saturation pulses.

In chapter 3, fat saturation techniques for abdominal 7 T imaging providing homogeneous suppression of fat signals are implemented and examined in a comparison study with healthy volunteers. The method that performs best applies the slice selection gradients with opposite polarity for the 90° excitation and 180° refocusing RF pulses. Due to the chemical shift, the excited fat signal is not refocused. The advantage of this method is that no additional high SAR RF pulses are necessary – reducing total SAR of this protocol.

Chapter 4 compares three different sequences for non-contrast-enhanced MRA of the lower extremities at 7 T. The modified ultra-fast GRE (MPRAGE) sequence with venous saturation RF pulses applied only every other TR performs best regarding vessel-to-background ratio with only a moderate artifact visible which appears similar to aliasing. The volunteer study also shows that cardiac triggering combined with TIAMO is a feasible strategy to successfully perform MRA of the lower extremity vessels at 7 T.

In chapter 5, the nature of the aliasing artifact observed in the ultra-fast GRE sequence of chapter 4 is investigated in simulations, phantom and in-vivo experiments. Two alternating effective TRs during image acquisition generate a periodic signal variation from line to line in k-space that leads to an aliasing artifact. This chapter shows a possible drawback of applying RF saturation pulses sparsely. Understanding the nature of this artifact is essential for further developments and modifications of this sequence variant.

In conclusion, this work presents methods that move 7 T closer to clinical applicability - not only for the head, but also for the more challenging areas of the abdomen and the lower extremities, down to the toes. The presented methods can be considered as a basis for further clinical research and as a part of future studies examining the potential of clinical 7 T imaging.

Chapter 7 Samenvatting

In dit proefschrift worden nieuwe varianten van sequenties gepresenteerd die geschikt zijn voor beeldvorming onder de complexe omstandigheden van 7 T. De individuele hoofdstukken beschrijven bruikbare methoden voor 7 T klinische beeldvorming.

In hoofdstuk 2 wordt een TOF MR angiografie sequentie gepresenteerd waarin de SAR van de sequentie wordt verlaagd door het VERSE algoritme toe te passen op de excitatie en verzadigings- RF pulsen. De repetitie tijd (TR) moet echter verlengd worden vanwege SAR beperkingen. Door gebruik te maken van de inherente verzadigingseffecten bij korte TRs is het mogelijk de pulshoek van de verzadigingspuls te verkleinen en de kleinste pulshoek waarbij de verzadiging nog toereikend en robuust is kan bepaald worden. Hierdoor kunnen zelfs kortere verzadigingspulsen gebruikt worden en is een korte totale meettijd haalbaar. De uiteindelijk totale meettijd is voornamelijk afhankelijk van de gekozen parameters in het protocol en niet van de SAR beperkingen. Hoge-resolutie protocollen met veneuze verzadiging in acceptabele acquisitie tijd zijn dus beschikbaar gemaakt voor klinische studies. Een verdere afname in meettijd zou misschien mogelijk zijn met verspreide verzadigingspulsen.

In hoofdstuk 3 zijn vet-verzadigingstechnieken voor homogene onderdrukking van vetsignaal in 7 T beeldvorming van het abdomen geïmplementeerd en onderzocht in een vergelijkingsstudie met gezonde vrijwilligers. De beste methode gebruikt plakselectieve gradiënten met tegenovergestelde polariteit voor de 90° excitatie en 180° refocusserende RF pulsen. Vanwege de chemische verschuiving wordt het geëxciteerde vetsignaal niet gerefocusseerd. Het voordeel van deze methode is dat extra RF pulsen met hoge SAR niet nodig zijn en dus de totale SAR van dit protocol laag blijft.

Hoofdstuk 4 vergelijkt drie verschillende sequenties voor 7 T MR angiografie van de onderste extremiteiten zonder contrastvloeistof. De aangepaste ultra-fast GRE (MPRAGE) sequentie met veneuze verzadigingspulsen die maar één keer per twee TRs uitgespeeld worden gaf de beste resultaten wat betreft de vaatachtergrond ratio met enkel een bescheiden zichtbaar artefact dat lijkt op aliasing. Uit de vrijwilligersstudie blijkt ook dat het triggeren van het hartritme samen met TIAMO een haalbare strategie is voor succesvolle MR angiografie van de vaten in de onderste extremiteiten.

In hoofdstuk 5 is de achtergrond van het aliasing artefact dat gezien werd met de ultra-fast GRE sequentie in hoofdstuk 4 onderzocht met behulp van simulaties, fantoom en in-vivo experimenten. Twee alternerende effectieve TRs gedurende de beeldacquisitie genereren een periodieke signaal variatie van lijn tot lijn in de k-ruimte dat leidt tot een aliasing artefact. Dit hoofstuk laat een mogelijk nadeel zien van verspreide verzadigingspulsen. Het begrijpen van het artefact is noodzakelijk voor verdere ontwikkelingen en aanpassingen van deze variant van de sequentie.

Samenvattend, in dit werk zijn methoden gepresenteerd die 7 T dichter naar de klinische toepasbaarheid brengen. Niet alleen voor het brein, maar ook voor meer uitdagende gebieden zoals het abdomen en de onderste extremiteiten, tot aan de tenen. De gepresenteerde methoden bieden een basis voor verder klinisch onderzoek en voor toekomstige studies naar de potentie van klinische 7 T beeldvorming.

Chapter 8 Perspectives

To date, an increasing number of 7 T MR systems (approx. 50) have been installed worldwide. Despite the increased proliferation, this field strength is currently still only used for research. As the detrimental effects of B_0 and B_1 inhomogeneities are tractable compared to those encountered in body imaging, most of the installed systems are used to perform only brain imaging. It is quite probable that 7 T head imaging may go clinical as a first step in the upcoming years, as a number of promising clinical and functional brain MRI studies have already been performed. The most important goal will be to show that the higher resolution and improved contrast of 7 T images can lead to earlier and improved diagnosis and thereby to improved therapies or surgery results.

7 T body imaging remains challenging and will demand more research due to the severe transmit field inhomogeneities and more restrictive SAR limitations. Especially for these applications, dedicated multichannel transmit coils are necessary to perform imaging. Simultaneously, new imaging methods and pulse sequences need to be developed to meet the challenging conditions. On the road to clinical body imaging, safe, fast and robust methods using affordable hardware need to be developed.

In the end, imaging at 7 Tesla has to be measured not only by how it can overcome the known ultra-high field issues, but by whether its advantages, e.g. the improved image resolution or acquisition speed, can lead to earlier and improved diagnosis and ultimately better patient outcome.

In this sense, all methods developed for 7-T imaging that satisfactorily address the known technical issues and simultaneously depict the contrast or resolution advantages of 7 Tesla have to be compared to the routinely used methods at the clinically established field strengths. Especially the angiographic methods discussed in chapter 2 and 4 have to prove – beyond their advantage of not needing contrast agents – that their higher resolution can potentially lead to improved diagnosis. Particularly in the head where the inherent challenges of 7

Tesla are not that severe, further comparison studies with greater numbers of patients have to be performed to show clinical relevance of the increased resolution.

In the peripheral angiography technique described in chapter 4, the acquisition time is still quite high. To establish this technique as a clinically available method for non-contrast-enhanced MRA, further effort needs to be put into reducing the total acquisition time. With the current system hardware available at the Erwin L. Hahn Institute, only 8 kW of peak RF amplifier power are available, of which only approximately half is available at the coil. In the case of this sequence and higher amplifier power, a more sparse application of the saturation pulses would presumably still lead to sufficient venous suppression due to the higher achieved flip angles. This would allow scanning patients with faster heart rate without measurement time prolongation.

In general, higher amplifier power would be beneficial for 7 Tesla body imaging by leading to better image quality in many cases. Especially sequences relying on RF pulses with high flip angle would profit, such as the single-shot fast spin echo sequence for body imaging discussed in chapter 3.

If sufficient receive coils are available – preferably not only in the in-plane direction but also in the through-plane direction – image acquisition cannot only be accelerated in the receive case but also by simultaneous multislice excitation using techniques like PINS (power independent of number of slices)[1], which can be applied to decrease imaging time or to reduce power deposition.

At the moment, RF shimming[2,3] and TIAMO[4,5] can be applied routinely in a robust way to increase image homogeneity. In the case of TIAMO, the standard CP^+ and CP^{2+} transmit modes can be used in many applications.[6,7] In the near future, parallel excitation, i.e. TRANSMIT SENSE,[8-10] combined with an increased number of excitation coils will help to homogenize the images over the entire FOV, even for body imaging, ideally including SAR optimization in the RF pulse calculation.[11] However, further development is necessary to allow these methods to be used in a fast, robust and reliable way.

As not only the B_1 field is inhomogeneous, combination with advanced B_0 shimming will be necessary, including slice-dependent B_0 shimming[12-14] and the installation of higher B_0 shim orders.[15]

The more the technical challenges can be reduced by ongoing research, the more research centers can concentrate on clinical research evaluating, e.g., the contrast advantages of 7 T such as inflow enhancement of blood or susceptibility weighted imaging.[16] This is the next big and necessary step to prove the potential of 7 Tesla and establish it as a specialized diagnostic device.

References

1. Norris DG, Koopmans PJ, Boyacioglu R, Barth M. Power Independent of Number of Slices (PINS) radiofrequency pulses for low-power simultaneous multislice excitation. Magn Reson Med 2011;66:1234-1240.

2. Collins CM, Liu W, Swift BJ, Smith MB. Combination of optimized transmit arrays and some receive array reconstruction methods can yield homogeneous images at very high frequencies. Magn Reson Med 2005;54:1327-1332.

3. Mao W, Smith MB, Collins CM. Exploring the limits of RF shimming for high-field MRI of the human head. Magn Reson Med 2006;56:918-922.

4. Orzada S, Maderwald S, Poser BA, Bitz AK, Quick HH, Ladd ME. RF excitation using time interleaved acquisition of modes (TIAMO) to address B1 inhomogeneity in high-field MRI. Magn Reson Med 2010;64:327-333.

5. Orzada S, Maderwald S, Poser BA, Johst S, Kannengiesser S, Ladd ME, Bitz AK. Time-interleaved acquisition of modes: an analysis of SAR and image contrast implications. Magn Reson Med 2012;67:1033-1041.

6. Johst S, Orzada S, Fischer A, Schafer LC, Nassenstein K, Umutlu L, Lauenstein TC, Ladd ME, Maderwald S. Sequence comparison for non-enhanced MRA of the lower extremity arteries at 7 Tesla. PLoS One 2014;9:e86274.

7. Johst S, Orzada S, Fischer A, Umutlu L, Ladd ME, Maderwald S. Comparison of fat saturation techniques for single-shot fast spin echo sequences for 7-T body imaging. Invest Radiol 2014;49:101-108.

8. Katscher U, Bornert P, Leussler C, van den Brink JS. Transmit SENSE. Magn Reson Med 2003;49:144-150.

9. Katscher U, Bornert P, van den Brink JS. Theoretical and numerical aspects of transmit SENSE. IEEE transactions on medical imaging 2004;23:520-525.

10. Katscher U, Rohrs J, Bornert P. Basic considerations on the impact of the coil array on the performance of Transmit SENSE. Magma (New York, NY 2005;18:81-88.

11. Guerin B, Gebhardt M, Cauley S, Adalsteinsson E, Wald LL. Local specific absorption rate (SAR), global SAR, transmitter power, and excitation accuracy trade-offs in low flip-angle parallel transmit pulse design. Magn Reson Med 2014;71:1446-1457.

12. Morrell G, Spielman D. Dynamic shimming for multi-slice magnetic resonance imaging. Magn Reson Med 1997;38:477-483.

13. Koch KM, McIntyre S, Nixon TW, Rothman DL, de Graaf RA. Dynamic shim updating on the human brain. J Magn Reson 2006;180:286-296.

14. Sengupta S, Welch EB, Zhao Y, Foxall D, Starewicz P, Anderson AW, Gore JC, Avison MJ. Dynamic B0 shimming at 7 T. Magn Reson Imaging 2011;29:483-496.

15. Pan JW, Lo KM, Hetherington HP. Role of very high order and degree B0 shimming for spectroscopic imaging of the human brain at 7 tesla. Magn Reson Med 2012;68:1007-1017.

16. Moser E, Stahlberg F, Ladd ME, Trattnig S. 7-T MR-from research to clinical applications? Nmr Biomed 2012;25:695-716.

Acknowledgement

This work would not have been possible without the support and contribution of many people.

The first person I would like to thank is Mark Ladd for giving me the opportunity to work in this team. It has been a great honor and pleasure to work in your group. I really enjoy the working conditions and the freedom that you give us in our personal research projects. The orientation on applicability of the developed methods and the close cooperation with the physicians from the University Hospital Essen is a valuable approach. I profited a lot from your broad knowledge of the MR field and your vast experience with the submission of paper manuscripts. I am glad that despite moving to the DKFZ in Heidelberg, we shall still be able to work together in the MRexcite project the years to come. And most importantly, I would like to thank you and David Norris very much for supervising my thesis. I am very glad that I have two such exceptional and experienced supervisors.

Very special thanks to Arend Heerschap, Radboud University Nijmegen, Andrew G. Webb, University Leiden, and Gregory J. Metzger, University Minnesota, for being in my thesis supervisory committee. I am really proud to have such experienced experts in my committee.

I would like to thank Harald H. Quick for confirming my position as sequence programmer within the team; knowing that you want me to stay after my thesis in the institute reassures me that the work I have done in the last years for this team was valued. I am really looking forward to working together with you.

I would like to thank Stefan Maderwald for his clever and pragmatic advice, his experience with all kinds of sequences and optimization of measurement protocols and his accurate appraisal for the best way to proceed with my projects and paper manuscripts. You are always the first person I talk to. Also, special thanks for all the times you’ve been such a patient volunteer! And of course thank you for all the effort you put into the maintenance and repair of the institute building.

Stephan Orzada, I thank you very much for all the support - not only during measurements, the conversations about imaging artifacts, unexpected sequence behaviors and difficult theories, your endless creative ideas, Matlab knowledge and of course your excellent imaging coils. Your knowledge of the MR field goes far beyond hardware which makes you one of the most important pillars of our institute. Thank you especially for all the conversations about politics and the social injustices of this world. Thank you for your insight. I am really glad that we get along not only professionally but are also friends.

Thank you very much, Andreas Bitz, you were the social conscience of the institute. I will always remember your speech in front of all men of the institute about sitting while urinating. There are few researchers who have your excellent and precise scientific skills in addition to your humaneness and an exceptional sense for interpersonal relations. I am still sad about you leaving for Heidelberg and thus, having only rarely the opportunity to see you. Nevertheless, I am sure that you have made the right decision. I really hope that we will manage to see each other more often in our leisure time in Heidelberg or Düsseldorf apart from professional occasions.

My thanks go to the neurosurgeons of the University Hospital Essen: Karsten Wrede, thank you for your humor and for pushing for the optimization of the TOF MRA sequence and performing the following patient study, your technical knowledge and strong interest in mechanisms behind imaging contrast, Tobias Schoemberg you were always in a good mood and we had a lot of exciting and suspenseful foosball matches, Bixia Chen, I am looking forward to working together with you while enjoying your green tea selection as well as your exotic food (thanks for all the conversations about cheese and food), and Philipp Dammann who, starting as a random roommate at the ISMRM in Stockholm, has become a true friend together with our life partners. I really hope that we will have the opportunity for a direct scientific cooperation in the future.

I would like to thank the radiologists of the Department of Diagnostic and Interventional Radiology and Neuroradiology, University Hospital Essen: Anja Fischer with whom we did great work on MRA of the lower extremities and Lale Umutlu (thank you for all the fruitful cooperation, I am looking forward to the next projects with you).

I would like to thank Oliver Kraff for managing contact with Siemens and for supporting me regarding the trouble with the ptx system. I am starting to really looking forward to our future ptx projects. And most importantly, thank you for providing the institute with coffee (special thanks for adopting my suggestion of going Fairtrade). Thank you for answering all my questions and being an advisor. It is very nice to share an office with you at the institute.

I want to thank especially Michael Bock for giving me the opportunity to work in his ultra-high field group at the DKFZ in Heidelberg and for supervising my diploma thesis. Thank you for giving me your confidence - this was my first and most important step into the MR field.

Special thanks to Sebastian Schmitter for his great and friendly support during my first steps in MR physics and IDEA. You were a great mentor. Thank you again for your accurate proof-reading of my diploma thesis. Your outstanding and accurate scientific methods are exemplary and the research you are performing now in Minnesota is really impressive.

Thanks to the whole ultra-high field team at Siemens, especially Rene Gumbrecht, for his great technical support with the ptx system.

I also want to thank, Benedikt Poser. You are a true IDEA expert and always extremely friendly in giving advices and sharing your knowledge and methods. It is really impressive to see your progress in Maastricht. It was very nice working together with you in supervising the Master's thesis of Sascha Brunheim. Thank you, Sascha, for being very motivated, interested and independent.

Special thanks to Michael Schwarz of the Department of General Psychology: Cognition, University of Duisburg-Essen, for the support on the statistical analysis

and to Lena Schäfer for performing and supporting a lot of volunteer and patient measurements and for organizing the measurement calendar.

I want to thank everyone from the Donders Center and the Radiology department of the University Hospital Nijmegen who I had the opportunity to meet or work with. Among others, Tom Scheenen, thank you for considering me for a position in your team – it really was a tough decision between your team and Mark's. I would also like to thank Markus Barth, Bart van der Bank, Lauren Bains (hopefully we will have the opportunity to work together in future), Mark van Uden and, especially Marnix Maas (thank you for all the nice conversations and for almost translating the summary of my thesis ;-)). Isabell Steinseifer, thank you for simulating the adiabatic WURST RF pulse, so I could confirm my simulation results. Mirjam Langemaat, thank you very much for doing me the favor of translating the summary of my thesis and Thiele Kobus, thank you very much for organizing the 'Benelux and friends' parties. I really like the cross-border concept of the Hahn institute. Lolita Ernst and Tildie Stijns, thank you very much for supporting the registration of my thesis. Thank you for helping me in such a friendly way throughout the whole process.

For organizing the whole institute, I would like to thank Simone Brunn and especially Sigrid Radermacher and Beate Fraß. Thank you for all the great help with the bureaucratic stuff and keeping the institute running.

I would like to thank Marcel Gratz (the whole institute profits from your technical support; thank you especially for saving me at the farewell party in Milan) and Maximilian Völker (having fun with the ptx system, thanks for being always funny and in a good mood). Mirjam Holbach, we had a great time visiting Sydney together with Andreas and Oliver - thank you for the cooperation. I really hope we will have the opportunity to work together in future and will hopefully find some time to meet again in our leisure time. Yacine Noureddine thank you especially for your help with the French letters; Anna Voss thanks for your good mood, your excellent taste in music and for sharing your nail polish with me, and Yujuan Zhao it was very nice meeting you. I am looking forward to the our next funny conversations and to seeing you at the upcoming ISMRM conferences.

All the other intelligent and nice people I am proud to work (or have worked) with in the institute: Susanne Ladd, Mark Oehmigen (it is very nice to have you back here in Essen), Jan-Willem Thielen (always funny and in a good mood), Ivonne Braun (thank you for being a volunteer for all of us, so often), Stefan Rietsch (welcome, new office-mate), Donghyun Hong, Seyedmorteza Rohani Rankouhi, Karsten Beiderwellen, Martina Flöser (I think you are doing a great job on Spokes and ptx pulse design), Ria Pradhan (thank you very much for proof-reading the English part of my acknowledgements), Andrea Lazik, Maike Lindemann, Irina Brote, Marco Schröder, Roxana Hirtopeanu, and Markus Thürling.

Ich danke meinen (Schul-)Freunden Dominik, Falko, Hannes und Ludwig. Es ist toll, dass wir uns trotz der Entfernung, dem seltenen Sehen und allem Alltagsstress uns als gute Freunde erhalten geblieben sind. Ihr seid mir wirklich ans Herz gewachsen und weiterhin sehr wichtig für mich. All unsere gemeinsamen verrückten Aktionen bleiben unvergessen! Und werden nicht die letzten bleiben...

Seit meinem Umzug von Heidelberg nach Düsseldorf habe ich glücklicherweise einige besonders wichtige und enge Freundschaften im Rhein-Ruhr-Gebiet gefunden:

Julia du bist ein echter Sonnenschein und ein äußerst aufmerksamer, freundlicher und liebenswerter Mensch mit großem Herz. Du hattest und hast immer ein offenes Ohr für mich, selbst für meine physikalischen Problemstellungen. Es ist wirklich schön, dass wir uns kennen gelernt haben. Ich freue mich jedes Mal riesig, wenn wir es schaffen uns zu sehen.

Vielen lieben Dank auch an meinen Cousin, Matthias. Es ist ein Glücksfall, dass du in der Nähe meines Instituts wohnst. Die spontanen Spaziergänge mit dir, haben mir oft geholfen den Kopf frei und etwas frische Luft und Sonne zu bekommen. Du bist ein sehr aufmerksamer Mensch und hattest immer ein offenes Ohr für meine aktuellen Forschungsgegenstände, bei denen es nicht so schnell voranging wie erhofft. Ich hoffe, dass wir weiterhin unsere unterhaltsamen Gespräche über Kapitalismus und damit verbundene Ungleichheiten in der Gesellschaft führen können.

Philipp Dammann und Johanna Hoffmann, zwischen uns Vieren hat sich eine sehr besondere und enge Freundschaft entwickelt (mittlerweile zusammen mit Leo, der ein wunderbares und fröhliches Kind ist). Zeit mit euch zu verbringen ist immer unglaublich inspirierend, erfüllend und kraftspendend. Danke für all die schönen Momente und tiefgründigen Gespräche über Literatur, Kunst und Gesellschaft. Ihr seid zwei aufmerksame, wertschätzende und kritische Menschen, die unser Leben sehr bereichert haben (und weiter werden). Wir freuen uns auf die weiteren Treffen des Literatursalons „Die umgedrehte 3“.

Ich möchte bei dieser Gelegenheit auch meinen Pateneltern Sigrid und Nik danken. Sehr gerne denke ich v.a. an die schöne Zeit zurück, die ich als Kind bei euch und mit eurer Familie verbracht habe.

Meinen Schwiegereltern, Petra und Alfons - zusammen mit Oma Fisch und natürlich Ludwig (sowie dem Familienfreund Marcel) - möchte ich vielmals für ihre Herzlichkeit, Großzügigkeit und Unterstützung danken. Ihr habt mich wirklich alle mit offen Armen in eurer Familie aufgenommen.

Ganz herzlich möchte ich noch meiner Familie danken für die immerwährende Unterstützung, die ich im Laufe meines Lebens erfahren habe. Danke, dass ihr an mich und meinen Lebensweg geglaubt habt. Meinen Geschwistern Marieke, Lukas und Henrik danke ich besonders für den starken Zusammenhalt (trotz der räumlichen Entfernung zwischen uns) – es ist schön eine große Familie zu haben. Schade, dass man nicht mehr so oft die Gelegenheit hat sich zu sehen und Dinge zu unternehmen. Ich weiß aber, dass wir jederzeit füreinander da sein werden.

Henrik, danke dass du und Klaudia mich zum Patenonkel von Klara gemacht habt. Danke für das Vertrauen in mich. Isolde und ich sind stolz Tante und Onkel von zwei so außergewöhnlichen Kindern, Leonard und Klara, zu sein. Es ist schön zu sehen, dass du so ein ausgeglichener, ruhiger und geduldiger Vater bist.

Klara, du bist ein fröhliches und cleveres Kind, das uns immer wieder erstaunt und uns viel Freude macht. Ich wünsche dir, dass du ein selbstbewusster, kritischer und emanzipierter Mensch wirst, der seinen eigenen Lebensweg gehen wird.

Lukas, auch wenn wir nicht mehr so viel Gelegenheit haben, Musik zu hören, zusammen loszuziehen oder Sparring zusammen im Muay Thai zu machen wie in Heidelberg vor ein paar Jahren, bist und bleibst du mein engster Vertrauter! Mit dir kann ich wirklich über alles reden und wenn etwas ist, weiß ich, dass ich dich immer anrufen kann. Ich danke dir für all die vertrauten Gespräche (nicht nur über die „alten“ Zeiten).

Marieke, auch dir danke ich für alle spannenden und ehrlichen Gespräche. Es war eine schöne und witzige Zeit als wir beide in Heidelberg gewohnt haben. Ich danke dir und Konsi (mein Lieblingsmitbewohner und beeindruckender Sozialwissenschaftler) besonders dafür, dass ich durch euch Isolde kennen gelernt habe. Es freut mich, dass du (zusammen mit Ede) deinen Weg in Koblenz gefunden hast.

Gissan und Wolfgang, ihr seid zwei unglaublich aufmerksame und liebenswerte Menschen. Ich habe so viele schöne Erinnerungen (nicht nur) aus meiner Kindheit an die Zeiten bei euch und ich fühle mich sehr verbunden mit euch beiden. Wir fühlen uns immer sehr wohl und erholt, wenn wir bei euch zu Besuch sind. Ich möchte euch beiden auch besonders für die Unterstützung während meines Studiums danken. Bei euch als Untermieter zu wohnen hat mir während der stressigen ersten Semester des Physikstudiums sehr den Rücken frei gehalten. Besonders habe ich auch euer Interesse an Themen geschätzt, die inhaltlich mein Physikstudium betrafen.

Meinen Eltern, Inge und Reinhard, danke ich, dass ihr mir nicht nur trotz dreier Geschwister das Studium finanziert habt, sondern auch dass ihr so tolle und besondere Eltern wart. Bessere Eltern hätte ich mir wirklich nicht wünschen können. Ihr habt uns Kinder zu kritischen, offenen und selbstbewussten Menschen erzogen und ich bin stolz, dass ich schon als kleines Kind mit auf

(Friedens-)Demonstrationen war. Ich bewundere außerdem eure Offenheit und eurer politisches und soziales Bewusstsein und den Lebensweg, den ihr gegangen seid. Danke für eure immerwährende Anerkennung und Unterstützung. Bis heute bin ich zusammen mit Isolde sehr gern bei euch, um spannende Gespräche zu führen und bei euch eine schöne Zeit zu verbringen.

Schließlich möchte ich der wichtigsten Person in meinem Leben danken. Isolde, du hast mich wirklich fast bedingungslos unterstützt und mir in den vielen langen, stressigen Situationen immer den Rücken frei gehalten. Danke für dein unglaublich geduldiges Verständnis und deine Kraft, wenn ich abends mal nicht abschalten konnte, launisch war oder mit mir nicht mehr viel anzufangen war, weil ich geistig völlig ausgelaugt und überreizt war. Du hattest wirklich immer ein offenes Ohr für meine Sorgen und Bedenken - trotz des Arbeitens an deiner eigenen Dissertation - und bist in allen Lebens- und Berufssituationen die perfekte Ratgeberin. Du bist ein wirklich aufmerksamer Mensch, der ein Auge für die kleinen Details und Zwischentöne im menschlichen Zusammenleben hat. Ich bin stolz auf deine Menschlichkeit, deinen wissenschaftlichen Werdegang sowie dein soziales Bewusstsein und Engagement. Ich möchte dir auch vielmals für unsere gemeinsamen spannenden und inspirierenden Gespräche über Politik, Gesellschaft und Ungerechtigkeiten in dieser Welt danken sowie für die wertvollen Impulse, die du mir gibst. Es ist wunderschön, dass wir so viele Gemeinsamkeiten haben. Danke, dass du mich auch und gerade in den Dingen bestärkst, in denen ich anders bin und von den ausgetretenen Pfaden abweiche. Ohne dich und deine Liebe wäre ich heute nicht der Mensch, der ich bin.

Curriculum Vitae

Sören Johst, born April 17th, 1984 in Heidelberg, Germany

Education

Since 04/2010	Erwin L. Hahn Institute for MRI, University Hospital Essen and University Duisburg-Essen, Essen, Germany. PhD candidate.
10/2004 – 02/2010	Study of physics at Ruprecht-Karls University Heidelberg. Diploma thesis “Time-of-Flight MR-Angiography at High Magnetic Fields” in the Highfield MRI research group (Prof. Dr. Michael Bock), German Cancer Research Center (DKFZ), Heidelberg, Germany. Grade: very good.
1994 – 2003	Hohenlohe Gymnasium Öhringen, Germany. Abitur 2003 with grade 1.0 (secondary school, diploma from German secondary school qualifying for university admission or matriculation)

Experience

2010 – 2014	Attending and presenting at the ISMRM
2011	“Basic RF Pulse Physics”, Lectures on MR: RF Pulses: Design and Applications, ESMRMB educational course, Essen
Since 04/2010	Erwin L. Hahn Institute for MRI / University Hospital Essen and University Duisburg-Essen, Essen, Germany. PhD candidate and researcher (pulse sequence programming and RF pulse calculation for 7 Tesla MRI)

2008	Student assistant at Ruprecht-Karls University Heidelberg: Mentoring medical students for preliminary medical examination
2003 – 2004	Civilian Service in a sheltered workgroup for disabled persons, Lichtenstern, Germany

Stipends

2011 – 2013	Educational stipends, International Society for Magnetic Resonance in Medicine (ISMRM), Berkley CA, USA
2012, 2014	Travel stipends, German Academic Exchange Service

Scientific Publications

Original Papers:	4 as first author; 12 as co-author
Conference Abstracts:	9 as first author; >20 as co-author

About the author

Sören Johst was born in Heidelberg, Germany the 17th of April, 1984. He grew up with his parents Inge und Reinhard Johst and his siblings Marieke, Lukas and Henrik in Willsbach and Eschenau (near Heilbronn), Germany. After completing secondary education in 2003 at the Hohenlohe-Gymnasium Öhringen, Germany, he did civilian service in a sheltered workgroup for disabled persons, Lichtenstern, Germany.

Afterwards he moved to Heidelberg to study Physics at the Ruprecht-Karls University and graduated with a diploma in Physics in 2010 with the diploma thesis “Time-of-Flight MR-Angiography at High Magnetic Fields” in the Highfield MRI research group (Prof. Dr. Michael Bock), German Cancer Research Center (DKFZ), Heidelberg, Germany.

Directly after his graduation, Sören moved to Düsseldorf and started his Ph.D. research at the Erwin L. Hahn Institute for MRI in Essen, Germany in the group of Prof. Dr. sc. techn. Mark E. Ladd. Here, he could profit from his former experience with 7 T MRI and sequence programming he gained during his time in Heidelberg. As a sequence programmer, he gained insight into various sequence types. He promoted not only his own projects, but was thereby part of most studies needing sequence modifications, e.g. by implementing TIAMO in various sequences. He could deepen and widen his knowledge in many topics of the MR field, e.g. the calculation of various types of RF pulses.

In 2011, he took part in organizing an ESMRMB educational course “Lectures on MR: RF Pulses: Design and Applications” at the Hahn Institute in Essen and prepared and lectured in the “Basic RF Pulse Physics” part of the course. Additionally he supervised two students with their bachelor and master thesis and was jointly responsible for the final implementation and troubleshooting of the ptx system at the Hahn institute.

Sören applied successfully for several stipends from the International Society for Magnetic Resonance in Medicine (ISMRM) and the German Academic

Exchange Service (DAAD). He attended and presented at every ISMRM meeting since 2010.

Sören Johst lives happily with his life partner Isolde Aigner in Düsseldorf, Germany. He finds balance in training kickboxing and kapap / krav maga, writing poems and is interested in politics (including feminism, social injustice, economics, ecology).

Peer-reviewed publications

Johst S, Maderwald S, Fischer A, Quick HH, Ladd ME, Orzada S. Investigation of the saturation pulse artifact in non-enhanced MR angiography of the lower extremity arteries at 7 Tesla. PLOS ONE (in press). (2014)

Wrede HK, Dammann P, **Johst S**, Mönninghoff C, Schlamann M, Maderwald S, Sandalcioglu E, Ladd ME, Forsting M, Sure U, Umutlu L. Non-enhanced MR imaging of cerebral arteriovenous malformations: 7 Tesla versus 1.5 Tesla. (under review). (2014)

Holbach M, Lambert J, **Johst S**, Ladd ME, Suter D. Optimized selective lactate excitation with a refocused multiple-quantum filter. (under review). (2014)

Wrede HK, **Johst S**, Dammann P, Özkan N, Mönninghoff C, Kraemer M, Maderwald S, Ladd ME, Sure U, Umutlu L, Schlamann M. Improved cerebral time-of-flight magnetic resonance angiography at 7 Tesla – feasibility study and preliminary results using optimized venous saturation pulses. PLOS ONE, 9(9): e106697. (2014)

Fischer A, Maderwald S, **Johst S**, Orzada S, Ladd ME, Umutlu L, Lauenstein TC, Kniemeyer HW, Nassenstein K. Initial evaluation of non-contrast-enhanced magnetic resonance angiography in patients with peripheral arterial occlusive disease at 7 T. Invest Radiol, 49(5): 331-8. (2014)

Johst S, Orzada S, Fischer A, Schäfer LC, Nassenstein K, Umutlu L, Lauenstein TC, Ladd ME, Maderwald S. Sequence comparison for non-enhanced MRA of the lower extremity arteries at 7 Tesla. PLOS ONE, 9(1): e86274. (2014)

Wrede KH, Dammann P, Mönninghoff C, **Johst S**, Maderwald S, Sandalcioglu IE, Müller O, Özkan N, Ladd ME, Forsting M, Schlamann MU, Sure U, Umutlu L. Non-enhanced MR imaging of cerebral aneurysms: 7 Tesla versus 1.5 Tesla. PLOS ONE, 9(1): e84562. (2014)

Johst S, Orzada S, Fischer A, Umutlu L, Ladd ME, Maderwald S. Comparison of fat saturation techniques for single-shot fast spin echo sequences for 7-T body imaging. Invest Radiol, 49(2): 101-8. (2014)

Fischer A, Maderwald S, Orzada S, **Johst S**, Schäfer LC, Ladd ME, Nassenstein K, Umutlu L, Lauenstein TC. Nonenhanced magnetic resonance angiography of the lower extremity vessels at 7 Tesla: Initial experience. Invest Radiol, 48(7): 525-34. (2013)

Umutlu L, Theysohn N, Maderwald S **Johst S**, Lauenstein TC, Moenninghoff C, Goericke S, Dammann P, Wrede KH, Ladd ME, Forsting M, Schlamann M. 7 Tesla MPRAGE imaging of the intracranial arterial vasculature: Nonenhanced versus contrast-enhanced. Acad Radiol, 20(5): 628-34. (2013)

Umutlu L, Maderwald S, Kinner S, Kraff O, Bitz AK, Orzada S, **Johst S**, Wrede KH, Forsting M, Ladd ME, Lauenstein T, Quick H. First-pass contrast-enhanced renal MRA at 7 Tesla: Initial results. Eur Radiol, 23(4): 1059-66. (2013)

Orzada S, **Johst S**, Maderwald S, Bitz AK, Solbach K, Ladd ME. Mitigation of B(1) (+) inhomogeneity on single-channel transmit systems with TIAMO. Magn Reson Med, 70(1): 290-4. (2012)

Johst S, Wrede KH, Ladd ME, Maderwald S. Time-of-flight magnetic resonance angiography at 7 T using venous saturation pulses with reduced flip angles. Invest Radiol, 47(8): 445-50. (2012)

Schmitter S, Bock M, **Johst S**, Auerbach E, Uğurbil K, van de Moortele PF. Contrast enhancement in TOF cerebral angiography at 7 T using saturation and MT pulses under SAR constraints: Impact of VERSE and sparse pulses. Magn Reson Med, 68(1): 188-97. (2012)

Wrede KH, **Johst S**, Dammann P, Umutlu L, Schlamann M, Sandalcioglu I, Sure U, Ladd ME, Maderwald S. Caudal image contrast inversion in MPRAGE at 7 Tesla: Problem and solution. Acad Radiol, 19(2): 172-8. (2012)

Orzada S, Maderwald S, Poser B, **Johst S**, Kannengiesser S, Ladd ME, Bitz AK. Time-interleaved acquisition of modes: An analysis of SAR and image contrast implications. Magn Reson Med, 67(4): 1033-41. (2012)